MULTIPHYSICS PHASE FIELD MODELING OF HYDROGEN DIFFUSION AND δ-HYDRIDE PRECIPITATION IN α-ZIRCONIUM

by

Andrea M. Jokisaari

A dissertation submitted in partial fulfillment
of the requirements for the degree of
Doctor of Philosophy
(Materials Science and Engineering)
in the University of Michigan
2016

Doctoral Committee:

Professor Katsuyo S. Thornton, Chairperson
Professor John E. Allison
Professor Michael Thouless
Professor Gary S. Was

DEDICATION

To my family, friends, and scientists of the past and the future.

ACKNOWLEDGMENTS

I would like to express my sincere appreciation to my advisor, Dr. Katsuyo Thornton, for her continuous support of my doctoral research. She gave me an opportunity to work in computational and theoretical materials science, an area in which I had little prior expertise. I would also like to thank the rest of my thesis committee: Dr. John Allison, Dr. Gary Was, and especially Dr. Michael Thouless, for their encouragement, insightful comments, and hard questions. I would also like to thank my fellow group members for their support and fellowship throughout my graduate career, particularly Dr. Larry Aagesen, Dr. Susan Gentry, Dr. Candace Gilet, and Dr. David Montiel. I also express my deepest gratitude to my mentors and collaborators, especially Dr. Olle Heinonen, Dr. Michael Tonks, and Cody Permann, for their support.

I would like to acknowledge the computation resources used in pursuit of this research, namely the High Performance Computing Center at Idaho National Laboratory. I also wish to express my gratitude to the MOOSE team at Idaho National Laboratory for their generous help and support. This research was supported by the Consortium for Advanced Simulation of Light Water Reactors (www.casl.gov), an Energy Innovation Hub (http://www.energy.gov/hubs) for Modeling and Simulation of Nuclear Reactors under U.S. Department of Energy Contract No. DE-AC05-00OR22725.

Words cannot express my love and appreciation for my husband, Jake, who encouraged

me to come to University of Michigan so many years ago and has been by my side throughout it all. I would like to thank my friends for enriching my life, and Ed Huebner and Christine Kelley for their invaluable personal support and guidance.

TABLE OF CONTENTS

LIST OF FIGURES

LIST OF TABLES

ABSTRACT

MULTIPHYSICS PHASE FIELD MODELING OF HYDROGEN DIFFUSION AND δ-HYDRIDE PRECIPITATION IN α-ZIRCONIUM

by

Andrea M. Jokisaari

Chairperson: Katsuyo Thornton

Hydride precipitation in zirconium is a significant factor limiting the lifetime of nuclear fuel cladding, because hydride microstructures play a key role in the degradation of fuel cladding. However, the behavior of hydrogen in zirconium has typically been modeled using mean field approaches, which do not consider microstructural evolution. This thesis describes a quantitative microstructural evolution model for the α-zirconium/δ-hydride system and the associated numerical methods and algorithms that were developed. The multiphysics, phase field-based model incorporates CALPHAD free energy descriptions, linear elastic solid mechanics, and classical nucleation theory. A flexible simulation software implementing the model, Hyrax, is built on the Multiphysics Object Oriented Simulation Environment (MOOSE) finite element framework. Hyrax is open-source and freely

available; moreover, the numerical methods and algorithms that have been developed are generalizable to other systems. The algorithms are described in detail, and verification studies for each are discussed. In addition, analyses of the sensitivity of the simulation results to the choice of numerical parameters are presented. For example, threshold values for the CALPHAD free energy algorithm and the use of mesh and time adaptivity when employing the nucleation algorithm are studied. Furthermore, preliminary insights into the nucleation behavior of δ-hydrides are described. These include a) the sensitivities of the nucleation rate to temperature, interfacial energy, composition and elastic energy, b) the spatial variation of the nucleation rate around a single precipitate, and c) the effect of interfacial energy and nucleation rate on the precipitate microstructure. Finally, several avenues for future work are discussed. Topics encompass the terminal solid solubility hysteresis of hydrogen in zirconium and the effects of the α/δ interfacial energy, as well as thermodiffusion, plasticity, and irradiation, which are not yet accounted for in the model.

CHAPTER I

Introduction

1.1 General introduction to nuclear electricity generation

Nuclear power reactors generate a significant share of the global production of electricity. There are currently 434 nuclear power reactors in operation worldwide [1] with a total generating capacity of 371.7 gigawatts-electric, and this capacity is projected to increase between 17 and 94% by 2030 [1]. In the United States, 100 reactors are currently in operation and five are under construction [2]. All nuclear power reactors in the United States are light water reactors (LWRs), in which $\left[^1\mathrm{H}\right]_2\mathrm{O}$ is the primary neutron moderator and fuel coolant [2]; both boiling water reactors (BWRs) and pressurized water reactors (PWRs) are in operation. Figure 1.1.1 illustrates the average capacity factor of the United States power reactor fleet from 1970 to 2011. The capacity factor is defined as the ratio of the actual amount of electrical power produced to the amount of electrical power that could theoretically have been produced if the power plant had been operating continuously at full power [3]. The average capacity factor has improved significantly since the 1970s, resulting in an increase in the total power generation of the fleet without the addition of new power plants, which are costly and time-consuming to build. The increase in capacity

factor is due both to a reduction in plant outages and to improvements in nuclear fuel [4].

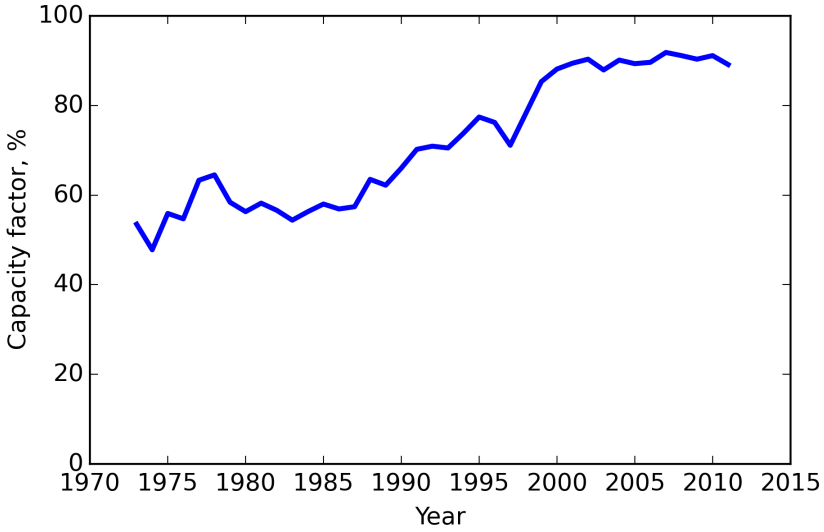

Figure 1.1.1: Average capacity factor of nuclear power plants in the United States, 1973-2011 [5].

Safe operation of the nuclear power reactor fleet is the highest priority in the United States nuclear industry [6, 7]. Two additional industry goals include reducing costs by achieving power uprates [7] and reducing nuclear waste by improving fuel burnup [7]. A power uprate is an increase in the maximum power level at which a plant may operate [8], and fuel burnup is a measure of the energy generated per mass of nuclear fuel [3]. The Consortium for the Advanced Simulation of Light Water Reactors (CASL), a United States Department of Energy Innovation Hub, has been created to help meet these goals by improving modeling and simulation of nuclear power plants [7]. Research within CASL is focused on the development of physics-based models of processes occurring within a reactor, including neutron transport, thermal hydraulics, nuclear fuel performance, and corrosion and surface chemistry [7]. The research presented in this thesis was funded by CASL as part of their Materials and Performance Optimization thrust.

1.2 Fuel cladding and its degradation

In an LWR, the nuclear fuel is contained in fuel assemblies, which are inserted into the reactor core. In the core, heat generated due to nuclear fission is removed by coolant water. A schematic of a fuel assembly is presented in Fig. 1.2.1. Although fuel assemblies differ by type and manufacturer, a typical fuel assembly is approximately four meters tall and contains on the order of 200 fuel rods [9]. A fuel rod is composed of a sealed zirconium alloy tube, called cladding, which is filled with fuel pellets of uranium oxide or mixed uranium/plutonium oxide [3]. A typical fuel rod has an outer diameter of 0.8-1.2 cm [3,9] with a cladding thickness of approximately 0.6 mm [3,9]. Fuel assemblies generally remain in the reactor core for three reactor refueling cycles, each of which is 18-24 months long, totaling approximately six years [3].

The fuel cladding serves several important purposes [3,9]. Primarily, cladding provides the first line of defense against the release of highly radioactive fission products from the fuel into the coolant. Cladding also protects the oxide fuel from the coolant and maintains dimensional stability of the fuel. In addition, cladding must have a high thermal conductivity and a low neutron absorption cross section for maximum reactor efficiency and fuel performance. Fuel cladding must fulfill these functions while in the demanding service environment of the reactor core, which entails neutron irradiation, high pressure, high temperature and vibration due to coolant flow [9]. Zirconium alloys meet all of these design criteria and are currently used for LWR fuel assembly components and fuel cladding [3,9].

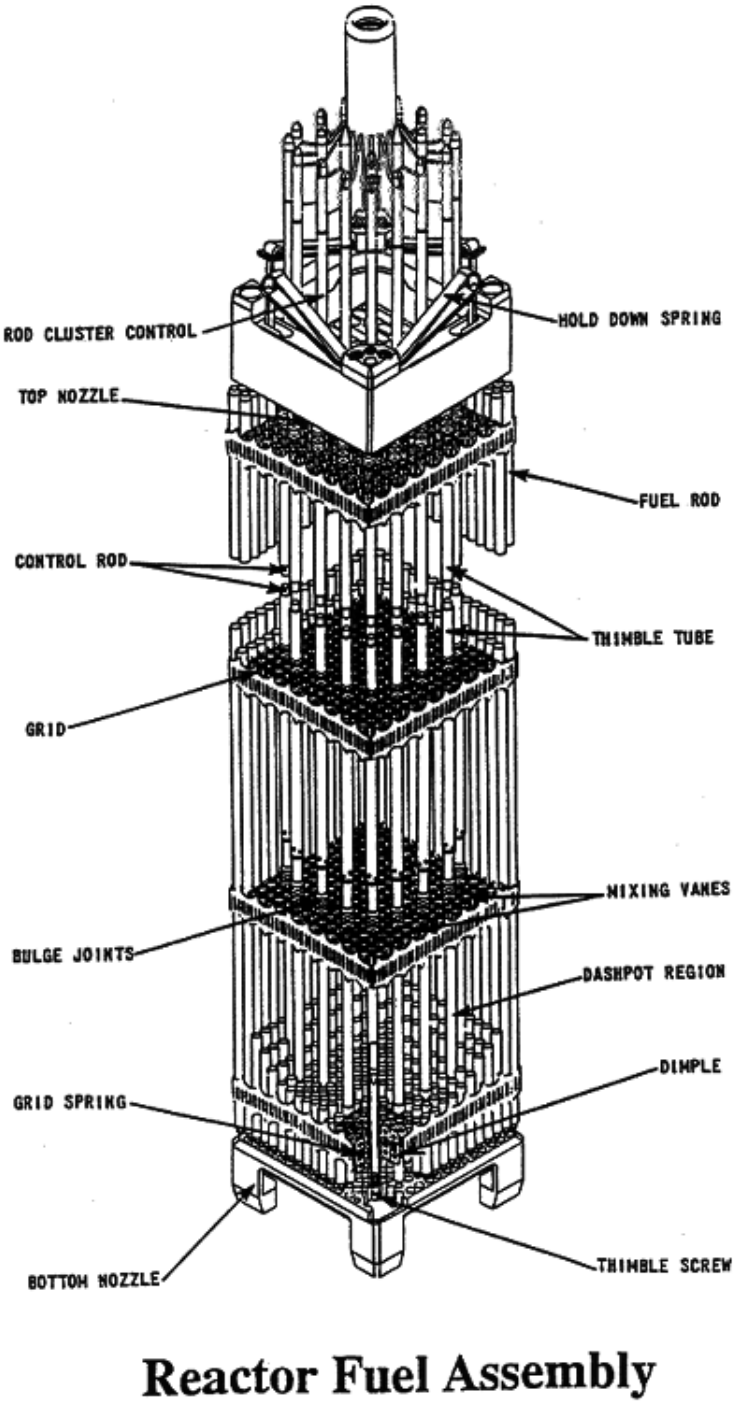

Figure 1.2.1: A PWR fuel assembly schematic, reproduced from Ref. [10].

Corrosion is one of the primary mechanisms for fuel cladding degradation. Zirconium alloy fuel cladding experiences significant corrosion during service due to its exposure to the coolant water [11], which has a temperature of approximately 600 K. The overall corrosion reaction is of the form

$$Zr + 2H_2O \rightarrow ZrO_2 + 4H, \tag{1.2.1}$$

where zirconium reacts with water to form zirconium oxide and hydrogen. The oxide adheres to the metal, reducing the load-bearing cross section of the cladding and acting as an insulating layer that prevents efficient heat transfer from the fuel to the coolant [3]. In addition, some fraction of the hydrogen formed during the corrosion reaction diffuses through the oxide layer into the zirconium [12, 13], termed ''hydrogen pickup.'' During service, fuel cladding may attain a total hydrogen concentration in the hundreds of parts per million by weight [14]. Upon reaching the solubility limit of hydrogen in zirconium, which is approximately 80 wt ppm at 600 K, zirconium hydrides precipitate. Spent fuel rod cladding typically exhibits a massive hydride layer on the water side and a network of hydrides of decreasing density toward the fuel side [15].

The presence of zirconium hydride precipitates in zirconium reduces the ductility of zirconium and its alloys [14]. During reactor operation, the presence of hydrides can cause fuel failures [15], commonly as a result of hydride blistering [16], hydride rim formation [15] or hydride reorientation [17]. Therefore, the amount of hydrogen in the fuel cladding is one factor limiting the fuel burnup that can be achieved. Once the fuel assembly has been removed from service, delayed hydride cracking may occur during spent fuel storage [18]. The presence of hydrogen induces brittle behavior below

a critical transition temperature, which is proportional to the hydrogen content [14]. For example, zirconium remains ductile at room temperature when it contains less than 10 wt ppm hydrogen, while the ductile-to-brittle transition temperature is greater than 600 K for a hydrogen concentration of 260 wt ppm. The transition behavior is not due to the presence or absence of hydride precipitates [14] but rather is due to a change in the failure mechanism [19]. Fractographic study indicates that void nucleation and coalescence between hydrides occurs during brittle failure, while shear instability in zirconium occurs between hydrides during ductile failure [19]. In addition, the orientation of macroscopic hydride precipitates affects how significantly the ductility of a zirconium specimen is reduced. Hydrides with long axes oriented 50-90° from the tensile stress axis reduce ductility while hydrides oriented parallel to the tensile stress axis do not [14]. Because fuel cladding experiences hoop stresses (circumferential stresses), the effect of hydrides on cladding ductility is minimized by fabricating the cladding tubes such that hydrides precipitate circumferentially rather than radially [20--22].

1.3 Characteristics of zirconium hydride in fuel cladding

Hydrogen is virtually insoluble in zirconium at 298 K, but its solubility increases with temperature, as shown in the zirconium-hydrogen phase diagram in Fig. 1.3.1 [23]. The two phases of interest in fuel cladding are hcp α-zirconium and fcc δ-hydride [24], though fct ϵ-hydride may precipitate at hydrogen contents >1250 wt ppm [24] and metastable fctγ-hydride may form at high cooling rates [23--25]. The α-zirconium/δ-hydride phase diagram is of the eutectoid type [23], and in both phases the tetrahedral interstitial sites

of the zirconium crystal structure are populated randomly with hydrogen [23]. The α-zirconium phase exhibits its maximum hydrogen solubility of 693 wt ppm (5.9 at.%) at 823 K [23], but hydrogen is essentially insoluble at 298 K. In addition, the δ-hydride phase is composed of 56.7 at.% hydrogen at 823 K and 66.7 at.% at 298 K [23].

Precipitates of δ-hydride exhibit certain crystallographic characteristics with respect to the α-zirconium matrix. The most common orientation relationship for δ-hydride and α-zirconium is $[11\bar{2}0]_\alpha$ nearly parallel to $[1\bar{1}0]_\delta$, and $(0001)_\alpha$ nearly parallel to $(111)_\delta$ (the actual planar orientation differs by approximately 8°) [22]. In addition, the δ-hydride phase exhibits a 17.3% volumetric expansion with respect to α-zirconium at 298 K [26,27]. The misfit strains between the two phases, ϵ_{ij}^{misfit}, also known as the stress-free transformation strains, are temperature dependent. Their temperature dependence is given in Table 1.1; at 298 K, $\epsilon_{11}^{misfit} = \epsilon_{22}^{misfit} = 4.58\%$ and $\epsilon_{33}^{misfit} = 7.22\%$ [26]. Because the δ-hydride phase is cubic, the anisotropy of the misfit strain arises from the anisotropy of the hcp α-zirconium lattice parameters.

Given the volume expansion of δ-hydride with respect to α-zirconium, a hydride precipitate will be elastically stressed unless the misfit strain is relaxed by the formation of dislocations and/or creep. A recent TEM investigation of δ-hydride precipitates in α-zirconium indicated that the elastic stress within the hydrides was approximately uniform and on the order of 1 GPa [28]. Elastic strains up to 5.5% were observed at the matrix/hydride interface, but decreased in the matrix to less than 0.5% within 50 nm of the interface [28]. However, plastic strain was also observed, as evidenced by dislocations in the basal plane of the matrix surrounding the precipitate [28].

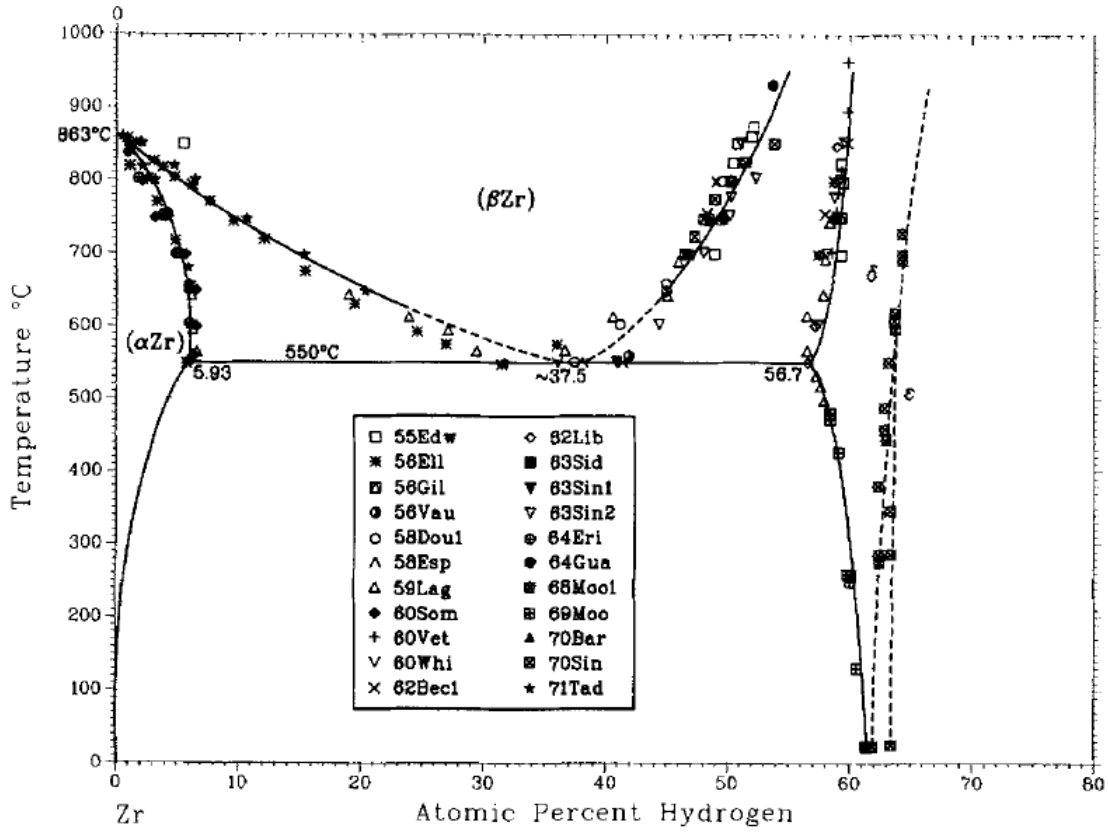

Figure 1.3.1: Phase diagram of the zirconium-hydrogen system. From Ref. [23].

Table 1.1: Stress-free transformation strain of δ-hydride with respect to α-zirconium.

Direction (α-Zr)	$\epsilon_{ij}^{misfit}(T)$ [26]
$[11\bar{2}0]$	$\epsilon_{11}^{misfit}(T) = 0.03888 + 2.315 \times 10^{-5} T$
$[1\bar{1}00]$	$\epsilon_{22}^{misfit}(T) = 0.03888 + 2.315 \times 10^{-5} T$
$[0001]$	$\epsilon_{33}^{misfit}(T) = 0.06646 + 1.9348 \times 10^{-5} T$

The precipitation of δ-hydride in α-zirconium occurs when the material becomes supersaturated with respect to the solubility limit (i.e., the terminal solid solubility, or TSS). Supersaturation may occur either by cooling the material at a fixed hydrogen concentration

or by increasing the hydrogen concentration at a fixed temperature. According to the thermodynamic theory of bulk phases, the solvus will be the same upon cooling and heating, i.e., hydride precipitation and dissolution, respectively. However, the experimentally measured TSS for precipitation (TSSp) is greater than the experimentally measured TSS for dissolution (TSSd) at any given temperature [20,29--33], a phenomenon known as TSS hysteresis. While investigations into the TSSd of various α-zirconium alloys indicate little variation, the TSSp results display a significant degree of scatter. In general, the TSSp and TSSd are not affected by the microstructure [30], amount of cold work [30], alloying content (with the exception of oxygen) [30,31], and heating and cooling rates up to 10°C/minute, though both the TSSp and TSSd are affected by higher rates [20,30,32,34]. Neutron irradiation increases the values of both the TSSp and TSSd, possibly due to hydrogen trapping at irradiation-induced defects, but the TSSp and TSSd are restored upon annealing [30,35]. The currently accepted theory of the origin of TSS hysteresis is that the TSSd represents the stress-free solubility limit, while the TSSp represents the effect of elastic energy on the solubility limit [36--39]. According to this analysis, only approximately 50% of the elastic strain energy induced by the crystallographic misfit strain is required to increase the solubility limit of hydrogen to the TSSp [40]. However, this analysis was performed using isotropic elastic constants and misfit strains and did not take into account temperature dependence. In addition, it imposed the shape of the hydride.

The microstructure of an α-zirconium/δ-hydride system contains two length scales: microscopic hydride precipitates on the order of tens to hundreds of nanometers, and agglomerates of microscopic precipitates on the order of tens of microns, which are referred to as macroscopic hydrides. The structure of macroscopic hydrides is controlled by the behavior of microscopic precipitates. Macroscopic precipitates tend to form long

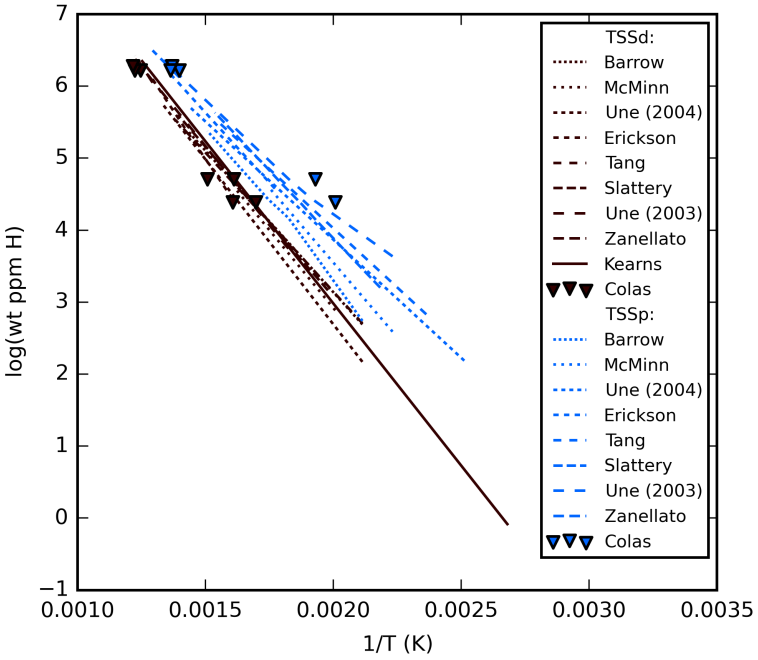

Figure 1.3.2: A compilation of TSSd and TSSp data of a-zirconium alloys (zirconium, Zircaloy-2, and Zircaloy-4), labeled by the first author. Experimental techniques include synchrotron X-ray diffraction (Barrow, Zircaloy-2 [33], Zanellato, Zircaloy-4 [32], Colas, Zircaloy-2 [20]); differential scanning calorimetry (McMinn, Zircaloy-2 and 4 [30], Une, Zircaloy-2 (2003) [31], Une, zirconium (2004) [41], Tang, Zircaloy-4 [42]); dilatometry (Erickson, zirconium [29], Slattery, Zircaloy-4 [43]); and diffusion coupling (Kearns, zirconium [44]).

''stringers'' that can be observed optically [25], as shown in Fig. 1.3.3. At low magnifications, a macroscopic hydride may appear to be one particle, but is found to be composed of stacks of hydride platelets [22, 45--47]. Microscopic δ-hydride platelets precipitate with the orientation relationship to zirconium described previously, and their habit plane tends to be close to the basal plane [22, 47]. The platelet shape is likely influenced by the elastic strain induced by the misfit between the hydride and the matrix, which is greatest in the [0001] direction. The apparent habit plane of a macroscopic hydride is a result of the angle

of alignment between the microscopic hydrides in the hydride stack [22, 45--47], as shown in Fig. 1.3.4.

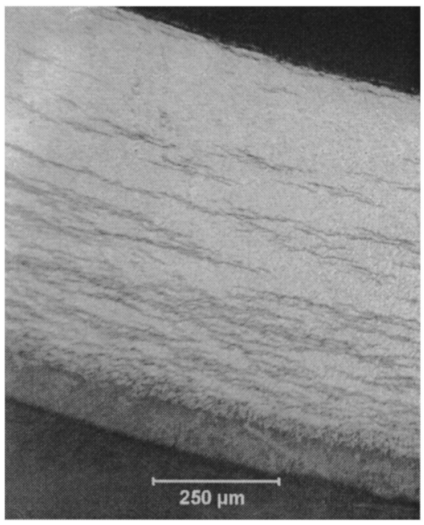

Figure 1.3.3: The macroscale hydride structure of irradiated Zircaloy-4 fuel cladding. The hydrides are present as dark gray circumferential lines. Reproduced from Ref. [48].

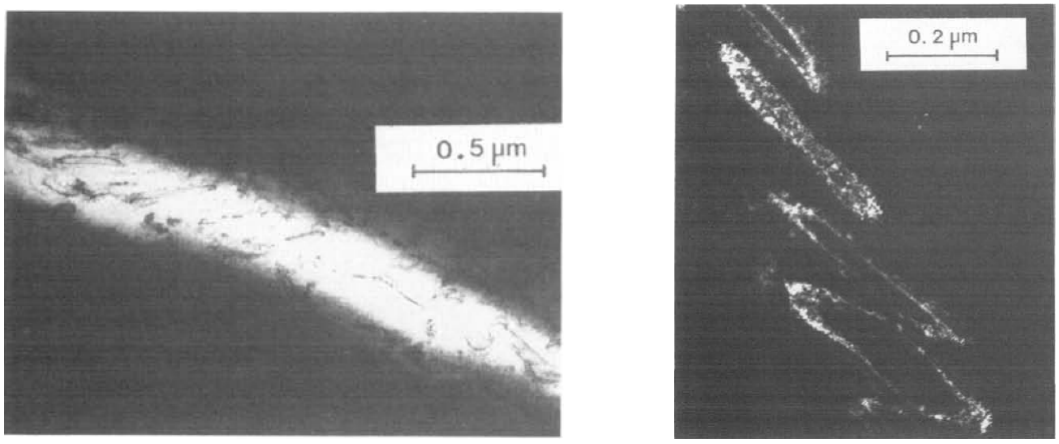

(a) (b)

Figure 1.3.4: The microstructure of a single hydride precipitate. (a) Bright field TEM; the hydride appears as one massive particle. (b) Dark field TEM; the individual plates in the hydride are apparent. Reproduced from Ref. [22].

The orientation of macroscopic hydrides experience depends on the stress field, which is termed stress orientation. In this process, the long axis of the hydride tends to form normal to a tensile stress (or parallel to a compressive stress) [49,50]. Stress orientation likely occurs to minimize the elastic energy incurred by the volume expansion of the hydride [49]. In addition, macroscopic hydrides may experience stress reorientation [49,50]. Reorientation may occur in fuel cladding when it experiences a change in temperature (e.g., due to refueling or oxide spalling). This may cause a change in the orientation of macroscopic hydrides from the circumferential direction to the radial direction, decreasing cladding ductility. In hydride reorientation, the temperature of the hydrided material fluctuates. Upon a temperature increase, some or all of the hydrides dissolve [50]. The specimen then undergoes a change in stress state and a decrease in temperature such that macroscopic hydrides re-precipitate with a new orientation [50]. The fraction of reoriented hydrides increases as the magnitude of the applied stress increases [49,51,52], and a minimum stress between approximately 80-150 MPa is required [49,51,52]. The reorientation of macroscopic hydrides is currently hypothesized to be caused by a change in the stacking angle of microscopic hydride arrays in response to the stress state of the material [22,47].

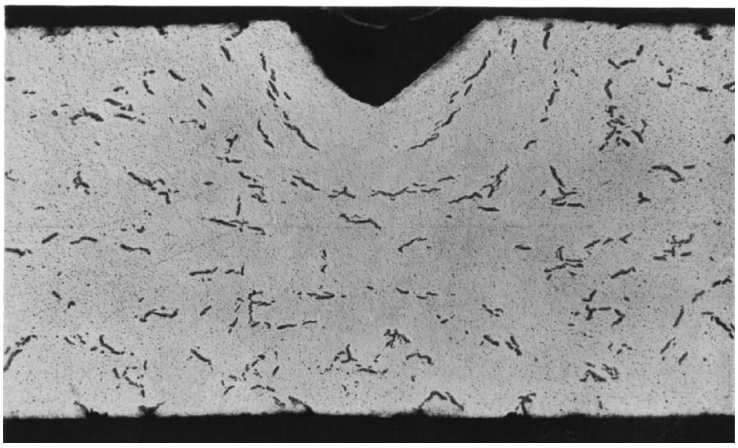

Figure 1.3.5: The stress orientation of macroscopic hydrides surrounding a gauge mark punched into Zircaloy-2. Reproduced from Ref. [49].

The arrangement of microscopic δ-hydride platelets into aligned stacks is currently hypothesized to be a result of autocatalytic nucleation and elastic stabilization [22,53]. In general, the free energy of the material and the activation energy for hydride nucleation are dependent upon both solute supersaturation and elastic energy. In the autocatalytic nucleation process, the presence of a coherent precipitate induces localized stresses within the matrix. The spatial distribution of the stresses around the precipitate may cause certain arrangements of precipitates to be energetically favorable [22,53]. Perovic et al. analytically examined the elastic interaction energy between two rectangular-platelet-shaped hydride precipitates in various geometrical arrangements [53]. Certain configurations of hydrides were found to have negative (favorable) interaction energies, such as platelets stacked at an angle of 30° or 60° [53].

1.4 Existing models of hydriding in zirconium

Several models have been proposed to describe hydrogen diffusion and hydride precipitation in zirconium, including reaction-diffusion models and phase field models. All of the reaction-diffusion models coarse-grain the α-zirconium/δ-hydride microstructure [54--58]. A reaction-diffusion model was proposed to describe hydrogen supercharging in zirconium and the formation of a surface hydride layer [56]. The model was later extended following Onsager theory to describe hydrogen diffusion in the presence of a temperature gradient [57]. Another reaction-diffusion model was developed that incorporates experimental TSSp and TSSd data as well as diffusion in a temperature gradient [58]. Finally, a reaction-diffusion model for hydride layer formation and cracking [54, 55] has been proposed. In addition, a mean-field model of the kinetics of hydride precipitation and hydride orientation under an applied stress [59] has been developed more recently. This mean-field model incorporates classical nucleation theory and assumes hydride orientation is determined upon nucleation, not growth [59].

Several phase field models have been developed recently to model the microstructure evolution of hydrides in zirconium. Unlike the reaction-diffusion models described previously, phase field models can simulate the evolution of individual precipitates in a matrix. A series of work has been published detailing the development of a phase field model of γ-hydride precipitation and growth in α-zirconium [60--64]. In the earlier works, the material was modeled as linear elastic [60--62], while in the later works, the material was modeled as elasto-plastic [63, 64]. Hydride nucleation was achieved with the use of noise terms in the evolution equations at the beginning of the simulation. It was found that the hydrogen distribution in the matrix increases in regions under tensile stress, particularly at the tips of the γ-hydride needles. In addition, plasticity in the zirconium

matrix decreases the growth rate, as measured by the length of the γ-hydride needle, due to a smaller increase of hydrogen in the matrix in the vicinity of the hydride tips [63,64]. Very recently, a quantitative phase field model has been proposed for γ-hydride precipitation and growth [65,66]. However, the effort fits phenomenological parameters to a Landau polynomial for the chemical free energy density without presenting a verification of the equilibrium compositions and phase fractions, and approximates nucleation behavior with random noise terms in the evolution equations.

1.5 Research objectives

As described in the previous section, the α-zirconium/δ-hydride system is of technological importance, particularly for the fuel assemblies of nuclear power reactors. However, the microstructural evolution of the system is complex and the underlying physics governing it are not thoroughly understood. A predictive model of the microstructural behavior of hydrogen in zirconium, specifically of hydride precipitation and growth, will improve the fuel performance models and could accelerate the development of new zirconium alloys. For example, the microstructural model could be used to understand the evolution of hydrides in the presence of a crack tip, which occurs during delayed hydride cracking [67]. In addition, data obtained from the microstructural model, such as the volume fraction of hydrides and the hydride nucleation rate, could be used in engineering-scale models. Thus, the objective of this thesis is the development of a quantitative microstructure evolution model of the α-zirconium/δ-hydride system that captures the diverse behaviors described in Section 1.3.

Because a phase field model is based on the thermodynamics and kinetics of the system, coupled effects are naturally captured. Therefore, a wide range of experimentally observed phenomena (e.g., hydrogen diffusion and hydride nucleation, both of which are influenced by stress) can be studied with the same model. Thus, the phase field approach has been chosen as the basis for the quantitative microstructure evolution model of the α-zirconium/δ-hydride system. The capabilities of the phase field model have been extended by coupling it with solid mechanics and classical nucleation theory. To obtain quantitative results, the combined model must be accurately parameterized. In addition, a flexible simulation software has been created based on the Multiphysics Object Oriented Simulation Environment (MOOSE) finite element framework [68, 69]. Numerical algorithms have been designed, implemented, and verified to address challenges presented by the model implementation. Finally, this development effort has been applied to study hydride nucleation in zirconium.

1.6 Dissertation outline

This dissertation contains six chapters: (I) Introduction, (II) Background, (III) General Method for Incorporating CALPHAD Free Energies of Mixing into Phase Field Models, (IV) A Nucleation Algorithm for the Coupled Conserved-Nonconserved Phase Field Model, (V) Preliminary Work and Future Work, and (VI) Conclusion.

In the present chapter, the motivation for this research is presented. The importance of zirconium in the nuclear power industry is examined and characteristic microstructural evolution behaviors of hydrides in zirconium are described. Existing models of hydrogen

in zirconium are summarized. Finally, the research objectives of this thesis are discussed.

In Chapter II, the background information is presented. A general description of the phase field modeling approach, a core component of the model, is given, as well as a discussion of the different approaches for incorporating nucleation into phase field models. In addition, the multiphysics microstructural model of the α-zirconium/δ-hydride system is described. The model combines a phase field model incorporating CALPHAD-based free energies, a linear elastic solid mechanics model, and a nucleation model based on classical nucleation theory. The governing equations and the nondimensionalization of the system are presented. Finally, an introduction to the finite element method and a description the code that has been developed for the multiphysics model is given. This chapter is based on the articles ''A Nucleation Algorithm for the Coupled Conserved-Nonconserved Phase Field Model'' [70] and ''General Method of Incorporating CALPHAD Free Energies of Mixing into Phase Field Models: Application to the α-Zirconium/δ-Hydride System'' [71].

In Chapter III, the algorithm developed to successfully incorporate the CALPHAD-based free energies is presented. The method is verified by planar interface simulations of the α-zirconium/δ-hydride system. The phase fractions and compositions obtained from the phase field simulations are compared to the values obtained via the common tangent construction on the original free energies and the sensitivity of the results to the choice of algorithm parameters is quantified. This chapter is based on the article ''General Method of Incorporating CALPHAD Free Energies of Mixing into Phase Field Models: Application to the α-Zirconium/δ-Hydride System'' [71].

In Chapter IV, the algorithms developed for incorporating nucleation into the model are presented. Both the introduction of a single nucleus and concurrent nucleation and growth are examined. The kinetics of a phase transformation exhibiting concurrent nucleation and

growth with a constant nucleation rate is analyzed in the form of the Avrami equation, and a statistical analysis is performed to determine if mesh and/or time adaptivity affects the simulation results. This chapter is based on the article ''A Nucleation Algorithm for the Coupled Conserved-Nonconserved Phase Field Model'' [70].

In Chapter V, preliminary results on the nucleation behavior of δ-hydride in α-zirconium are presented, along with suggestions for future work. The sensitivities of the nucleation rate to temperature, interfacial energy, hydrogen concentration and elastic energy are explored within a small parametric space, and the spatial variation of the nucleation rate around a single precipitate at a single hydrogen composition is described and analyzed. Preliminary concurrent nucleation and growth simulations illustrate how the precipitate microstructure is affected by the nucleation rate. Multiple avenues of future work are suggested; topics include the terminal solid solubility hysteresis of hydrogen in zirconium and the effects of the α/δ interfacial energy, as well as thermodiffusion, plasticity, and irradiation, which are not yet accounted for in the model.

In Chapter VI, the summary and impact of this research are presented.

CHAPTER II

Background: Physics and Numerical Methods

In this chapter, a multiphysics phase field model is proposed to describe the α-zirconium/δ-hydride system. The model incorporates solid mechanics and classical nucleation theory. This model is used throughout this thesis, with certain variations that are identified at the beginning of each chapter. Prior to this work, a quantitative phase field model for the microstructural evolution of the α-zirconium/δ-hydride system has not been presented in the literature. Below, an introduction to the phase field model is first given. Next, the multiphysics phase field model for the α-zirconium/δ-hydride system is described. Finally, an introduction to finite element modeling and the computational framework that was developed is discussed.

2.1 Introduction to the Phase Field Model

In this section, a general introduction to the phase field modeling approach is given. Comprehensive descriptions and reviews of phase field modeling are found in Refs. [72--77]. Phase field modeling is a method of simulating microstructural evolution based on

thermodynamics and kinetics, and has been successfully applied to phase transformations such as spinodal decomposition [78--81], coarsening [82--86], solidification [87--89], and thin film growth [80, 90--93].

In a phase field model, a microstructure is described by one or more continuous conserved or nonconserved field variables, termed order parameters. An order parameter is generally denoted as $\phi(\mathbf{r}, t)$ and indicates the phase at $\mathbf{r}$, where $\mathbf{r}$ is position and t is time. Each phase is designated by a bulk value (e.g., $\phi = 0$ for the α phase and $\phi = 1$ for the β phase), and the value of ϕ changes smoothly between the phases. The position of the interface between the phases is described by an intermediate value (e.g., $\phi = 0.5$), schematically illustrated in Fig. 2.1.1. Thus, the phase field methodology eliminates the need to track the positions of the interfaces explicitly. The free energy of the system can be described as a functional of the order parameters, and the evolution of the system is driven by the reduction of the free energy [81, 94]. The Gibbs-Thomson effect, which causes a shift in the compositions of phases due to the presence of a curved interface, is automatically incorporated.

2.1.1 Free energy

The system, whose microstructure is described by order parameters $\phi_1(\mathbf{r}, t), ...\phi_n(\mathbf{r}, t)$, has a free energy G [95],

$$G = G_{bulk} + G_{grad} + ... \tag{2.1.1}$$

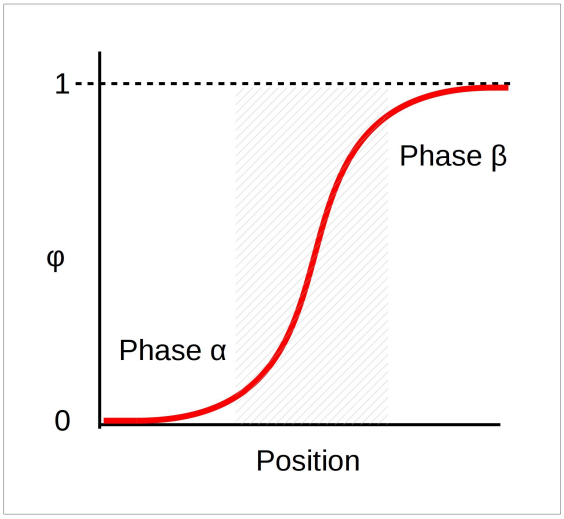

Figure 2.1.1: A schematic illustration of the diffuse interface profile between phases in a phase field model, where ϕ is the phase field variable. The interface region is marked with gray hatching.

where G_{bulk} is the ''bulk'' or ''chemical'' energy related to compositional inhomogeneity and G_{grad} is the gradient energy, which is incorporated to generate a diffuse interface. Additional terms may be added to Eq. 2.1.1, such as elastic energy, to further describe the system being modeled. The free energy is a functional of the order parameters [95], i.e.,

$$G = G\left[\phi_1\left(\mathbf{r},t\right),...\phi_n\left(\mathbf{r},t\right),\nabla\phi_1\left(\mathbf{r},t\right),...\nabla\phi_n\left(\mathbf{r},t\right)\right], \tag{2.1.2}$$

and is typically written in integral form,

$$G = \int_V \left(g_{bulk}\left(\phi_1,...\phi_n\right) + g_{grad}\left(\phi_1,...\phi_n\right) + ...\right) dV \tag{2.1.3}$$

where V is the volume, g_{bulk} is the chemical free energy density and g_{grad} is the gradient energy density. The typical form of g_{grad} is proportional to the square of the gradient of the order parameter, and thus Eq. 2.1.3 becomes [95]

$$G = \int_V \left(g_{bulk}\left(\phi_1, ...\phi_n\right) + \kappa_1 |\nabla \phi_1|^2 ... + \kappa_n |\nabla \phi_n|^2 \right) dV \tag{2.1.4}$$

where κ is a gradient energy coefficient. The g_{bulk} term is generally in the form of a double well with an energy barrier W of some height between the wells; a schematic of a simple $g_{bulk}\left(\phi\right)$ is given in Fig. 2.1.2. The g_{bulk} term favors infinitely sharp interfaces between phases, while the g_{grad} term favors a uniform mixture by imposing a gradient energy penalty (i.e., the free energy of the system increases as the gradient of ϕ becomes greater). A diffuse interface with a finite width results from the competition between the g_{bulk} and g_{grad} terms [95]. The interfacial width is typically larger than the physical interface and is treated as a computational parameter. The interfacial energy of the physical system can be incorporated by controlling W, κ, and the diffuse interface width in the model.

2.1.2 Governing equations

The evolution of the system is driven by the reduction of the free energy. For a conserved field variable, the time evolution is governed by the Cahn-Hilliard equation [81], while for a nonconserved field variable, the Allen-Cahn equation describes the dynamics [94]. The Cahn-Hilliard equation is based on the theory of irreversible thermodynamics [81, 96] and can be considered as a generalized diffusion equation. For a conserved quantity c, the flux $\mathbf{J}_c$ of c is given as

$$\mathbf{J}_c = -M_c \nabla \Phi_c \tag{2.1.5}$$

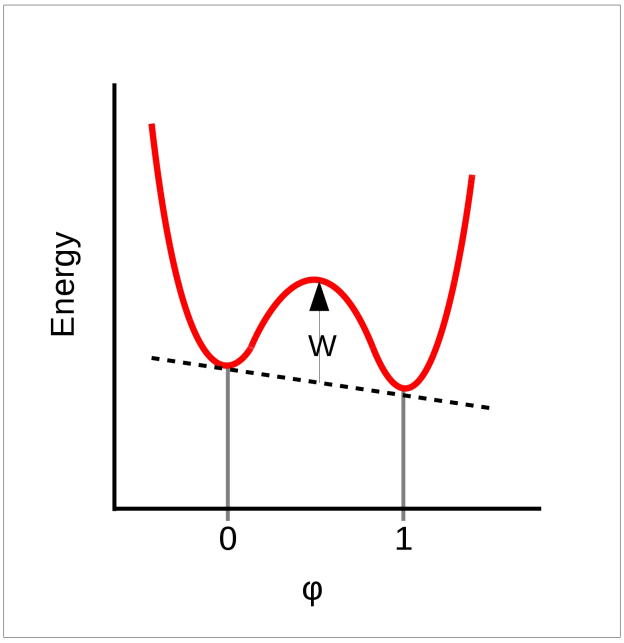

Figure 2.1.2: A schematic of the bulk free energy as a function of the phase field variable, ϕ. The energy has a a double-well shape with a well height W. The equilibrium compositions of the phases are marked.

where M_c is the mobility of c and Φ_c is the diffusion potential [96]; Eq. 2.1.5 is the so-called ''force-flux relationship'' [96]. The law of mass conservation dictates that the rate of change in c with respect to time is [81, 96]

$$\frac{\partial c}{\partial t} = -\nabla \cdot \mathbf{J}_c = \nabla \cdot (M_c \nabla \Phi_c) \,. \tag{2.1.6}$$

The Cahn-Hilliard equation is given by Eq. 2.1.6, where $\Phi_c = \delta F / \delta c$ [81]. For example,

$$\frac{\delta F}{\delta c} = \frac{\partial f_{chem}}{\partial c} - 2\kappa_c \nabla^2 c \tag{2.1.7}$$

for Eq. 2.1.4.

Unlike the conserved order parameter system, a system with a non-conserved parame-

ter evolves such that the change is driven by the fastest decrease in free energy without the constraint of mass conservation. In this case, the dynamics are described by the Allen-Cahn equation [94]. For a nonconserved quantity n in a non-equilibrium system, the change of n with respect to time is directly proportional to its potential Φ_n [94],

$$\frac{\partial n}{\partial t} = -L_n \Phi_n = -L_n \frac{\delta F}{\delta n}, \tag{2.1.8}$$

where L_n is the kinetic coefficient for the nonconserved quantity. In a phase field model governed by the Allen-Cahn equation, the velocity of interfaces is proportional to the mean curvature [94].

2.2 Multiphysics phase field model

2.2.1 Free energy formulation

A phase field model simulates the evolution of the system based on the reduction of the total free energy. The α-zirconium/δ-hydride system may be described using a coupled conserved-nonconserved system. The conserved field variable, X, is the atomic fraction of hydrogen, and the nonconserved structural field variable, η, tracks the structural transformation between the two phases ($\eta = 0$ for the α phase and $\eta = 1$ for the δ phase). For the α-zirconium/δ-hydride system, the free energy is expressed as

$$G = \int_V \left(g_{chem}\left(X, \eta, T\right) + \frac{\kappa_X}{2} |\nabla X|^2 + \frac{\kappa_\eta}{2} |\nabla \eta|^2 \right) dV + G_{elastic}, \tag{2.2.1}$$

where κ_X and κ_η are the gradient energy coefficients for the atomic fraction of hydrogen and the structural order parameter, respectively, g_{chem} is the bulk chemical free energy density, $G_{elastic}$ is the elastic strain energy, T is the absolute temperature, and V is the volume of the system. Although elastic strain energy affects the total free energy of the system, chemical and elastic energy contributions are typically incorporated separately in a phase field model [72]. The incorporation of elastic strain energy will be described in Section 2.2.3.

The expression for g_{chem} follows the Wheeler-Boettinger-McFadden (WBM) [97] model. In the α-zirconium/δ-hydride model, g_{chem} is given as

$$g_{chem} = \frac{1}{\Omega_o}\left[\left(1-h\left(\eta\right)\right)G_{mix}^{0,\alpha}\left(X,T\right)+h\left(\eta\right)G_{mix}^{0,\delta}\left(X,T\right)+wk\left(\eta\right)\right] \tag{2.2.2}$$

where $G_{mix}^{0,\alpha}\left(X,T\right)$ is the molar free energy of mixing of α-zirconium with hydrogen, $G_{mix}^{0,\delta}\left(X,T\right)$ is the molar free energy for δ-hydride, and $\Omega_0 = 1.4\times10^{-5}$ m^3/mol is the molar volume of α-zirconium. In addition, $h\left(\eta\right)=\eta^2\left(3-2\eta\right)$ is the interpolation function that increases monotonically from $h\left(0\right)=0$ to $h\left(1\right)=1$, $k\left(\eta\right)=\eta^2\left(\eta-1\right)^2$ is the double well function, and w controls the height of the barrier, though other terms may contribute to the total energy barrier. The $G_{mix}^{0,\alpha}\left(X,T\right)$ and $G_{mix}^{0,\delta}\left(X,T\right)$ energies were calculated by Dupin et al. using the CALPHAD method [98] and are described in Section 2.2.1. The mixing energies were approximated as the piecewise functions $\tilde{G}_{mix}^{0,\alpha}\left(X,T\right)$ and $\tilde{G}_{mix}^{0,\delta}\left(X,T\right)$ to overcome numerical challenges; this approximation is detailed in Chapter III.

CALPHAD free energies of mixing

Quantitative modeling of the α-zirconium/δ-hydride system requires a realistic description of the chemical free energy, and the CALPHAD method was chosen for the model. The CALPHAD method is a semi-empirical approach for formulating free energies of mixing using known thermodynamic data and equilibrium phase diagrams [99,100]. The incorporation of realistic CALPHAD-based free energies into phase field models has significantly increased prediction capabilities of phase field modeling [73,75,76]. To date, this approach has been applied to steels [101--104], superalloys [84,105--111], and aluminum alloys [112--114], among others, with studies examining both solidification [101,105,110,112,114--120] and solid-state transformations [84,102--109,111,113,121--123].

In the CALPHAD method, a molar free energy of mixing for a single phase is expressed in the form

$$G_{mix}^{0,i}(X,T) = G_{ref}^{0,i}(X,T) + G_{ideal}^{0,i}(X,T) + G_{excess}^{0,i}(X,T), \tag{2.2.3}$$

where $G_{ref}^{0,i}$ is the reference free energy of mixing of the ''end members'' [100], $G_{ideal}^{0,i}$ is the free energy of mixing for an ideal solution, and $G_{excess}^{0,i}$ is the free energy of mixing that deviates from the ideal solution model [99]. The end members may be elements or stoichiometric compounds, as in the case of free energies formulated according to a sublattice model [100]. The sublattice model is a common technique for developing free energies of mixing for substitutional and interstitial solutions as well as compounds [100]. In the sublattice model, the end member compound is formed when all of the vacancies in the sublattice are filled.

Both the α-zirconium phase (solid solution with interstitial hydrogen) and the δ-hydride

phase can be modeled as two-sublattice systems, in which zirconium fills the first sublattice and hydrogen and vacancies fill the second sublattice [124, 125]. The α-zirconium phase is notated as $(Zr)_1 (H, vac)_1$, while δ-zirconium hydride is notated as $(Zr)_1 (H, vac)_2$ [98]. The subscripts indicate the number of sites of each sublattice per unit cell. The free energies of mixing for the α-zirconium/δ-hydride system were parameterized by Dupin et al. [98] using the CALPHAD method. The molar free energy of mixing for hydrogen in α-zirconium is given as

$$\begin{aligned} G_{mix}^{0,\alpha}(X,T) &= \left[(1-2X)\, G_{Zr}^{0,hcp}(T) + X G_{ZrH}^{0,hcp}(T)\right] \\ &\quad + RT\left[X \ln\left(\frac{X}{1-X}\right) + (1-2X)\ln\left(\frac{1-2X}{1-X}\right)\right] \end{aligned} \tag{2.2.4}$$

and that for δ-hydride is given as

$$\begin{aligned} G_{mix}^{0,\delta}(X,T) &= \frac{1}{2}\left[(2-3X)\, G_{Zr}^{0,fcc}(T) + X G_{ZrH_2}^{0,fcc}(T)\right] \\ &\quad + RT\left[X \ln\left(\frac{X}{2(1-X)}\right) + (2-3X)\ln\left(\frac{2-3X}{2(1-X)}\right)\right] \\ &\quad + \left(\frac{3X^2-2X}{4(X-1)^2}\right)\left[(X-1)\, L_{fcc}^{0}(T) + (1-2X)\, L_{fcc}^{1}(T)\right] \end{aligned} \tag{2.2.5}$$

where R is the gas constant [98]. The parameterizations for $G_{ZrH}^{0,hcp}(T)$, $G_{ZrH_2}^{0,fcc}(T)$, $L_{fcc}^{0}(T)$, and $L_{fcc}^{1}(T)$ are supplied by Ref. [98], and the parameterizations for $G_{Zr}^{0,hcp}(T)$ and $G_{Zr}^{0,fcc}(T)$ are from Ref. [126]. We parameterized $G_{H_2}^{0,gas}(T)$, which is needed to calculate $G_{ZrH}^{0,hcp}(T)$ and $G_{ZrH_2}^{0,fcc}(T)$, using the data in Ref. [127]. All of the parameterizations are reproduced below.

$$G_{Zr}^{0,hcp}(T) = -7827.595 + 125.64905T - 24.1618T\ln(T) - 4.37791\text{x}10^{-3}T^2 + 34971T^{-1}\ \text{J/mol} \quad (2.2.6)$$

$$G_{Zr}^{0,fcc}(T) = -227.595 + 124.74905T - 24.1618T\ln(T) - 4.37791\text{x}10^{-3}T^2 + 34971T^{-1}\ \text{J/mol} \quad (2.2.7)$$

$$G_{H_2}^{0,gas}(T) = 8055.34 - 243.79T + 18.313T\ln(T) - 0.034513T^2 - 734182T^{-1}\text{J/mol} \quad (2.2.8)$$

$$G_{ZrH}^{0,hcp}(T) = -45965 + 41.6T + G_{Zr}^{0,hcp}(T) + \frac{1}{2}G_{H_2}^{0,gas}(T)\ \text{J/mol} \quad (2.2.9)$$

$$G_{ZrH_2}^{0,fcc}(T) = -170490 + 208.2T - 9.47T\ln(T) + G_{Zr}^{0,hcp}(T) + G_{H_2}^{0,gas}(T)\ \text{J/mol} \quad (2.2.10)$$

$$L_{fcc}^{0} = 14385 - 6.0T \quad (2.2.11)$$

$$L^1_{fcc} = -106445 + 87.3T \tag{2.2.12}$$

2.2.2 Governing equations

The microstructural evolution of the system is governed by coupled conserved-nonconserved dynamics [97]. Note that this model is presented for isothermal temperature fields; it has not been verified to model the effect of temperature gradients. The Cahn-Hilliard equation [81] governs the evolution of the atomic fraction of hydrogen. To reduce computational resource requirements, the Cahn-Hilliard equation is split into two second-order equations [128, 129]. Although the full fourth-order Cahn-Hilliard equation may be implemented, the split formulation provides significantly higher computational efficiency for the finite element method by using lower order elements [130]. The time evolution of X is given by

$$\frac{1}{\Omega_0}\frac{\partial X(\mathbf{r},t)}{\partial t} = \nabla \cdot M\nabla\left(\frac{\delta G}{\delta X}\right), \tag{2.2.13}$$

where M is the mobility, and

$$\frac{\delta G}{\delta X} = \frac{\partial g_{chem}}{\partial X} - \kappa_X \nabla^2 X + \frac{\partial g_{el}}{\partial X}. \tag{2.2.14}$$

The mobility of hydrogen in the system must be formulated such that the diffusivity of hydrogen in the α and δ phases is reproduced in the phase field model. In addition, the mobility must be positive [96]. For a single phase, the flux $\mathbf{J}_H$ of hydrogen calculated

according to Fick's first law must match the flux in the phase field model,

$$\mathbf{J}_H = -D\nabla\left(\frac{X}{\Omega_0}\right) = -M\nabla\left(\frac{1}{\Omega_0}\frac{\partial G_{mix}^{0,i}}{\partial X}\right), \tag{2.2.15}$$

where D is the diffusivity, $\mathbf{J}_H$ has units of $\text{mol}\cdot\text{m}^{-2}\text{s}^{-1}$, and M has units of $\text{mol}\cdot\text{m}^{2}\text{J}^{-1}\text{s}^{-1}$. For the α-zirconium/δ-hydride phase field model, the mobility in the α phase is given as

$$M^{\alpha}\left(X,T\right) = \frac{D^{\alpha}\left(T\right)}{\partial^2 \tilde{G}_{mix}^{0,\alpha}/\partial X^2} \tag{2.2.16}$$

and the mobility in the δ phase is given as

$$M^{\delta}\left(X,T\right) = \frac{D^{\delta}\left(T\right)}{\partial^2 \tilde{G}_{mix}^{0,\delta}/\partial X^2} \tag{2.2.17}$$

such that the total mobility in Eq. 2.2.13 is

$$M\left(X,\eta,T\right) = \left(1-h\left(\eta\right)\right)M^{\alpha}\left(X,T\right) + h\left(\eta\right)M^{\delta}\left(X,T\right), \tag{2.2.18}$$

where $D^{\alpha}\left(T\right)$ is the diffusivity of hydrogen in α-zirconium [131] and $D^{\delta}\left(T\right)$ is the diffusivity of hydrogen in δ-hydride [132]. Thus, the conservation equation is given as

$$\frac{1}{\Omega_0}\frac{\partial X}{\partial t} = -\nabla\cdot\mathbf{J}_H. \tag{2.2.19}$$

In addition, the Allen-Cahn equation [94] governs the evolution of the structural order parameter as

$$\frac{\partial \eta\left(\mathbf{r},t\right)}{\partial t} = -L\frac{\delta G}{\delta \eta} = -L\left(\frac{\partial g_{chem}}{\partial \eta} - \kappa_{\eta}\nabla^2\eta + \frac{\partial g_{el}}{\partial \eta}\right), \tag{2.2.20}$$

where L is the kinetic coefficient, which has units of $m^3J^{-1}s^{-1}$. Both the mobility and the kinetic coefficient are assumed isotropic.

2.2.3 Solid mechanics model

General model

The elastic strains in the hydride and in the surrounding matrix are important factors influencing the microstructural evolution of hydride precipitates. As described in the Introduction, TEM investigation indicates that elastic strains up to 5.5% are present at the α-zirconium/δ-hydride interface of nanoscale hydrides [28]. The maximum observed elastic strain value is much larger than the macroscopic yield point (typically assumed as 0.2%) and is only somewhat smaller than the maximum crystallographic misfit strain (7.2% [27]). These observations indicate that coherency between the matrix and hydride introduces elastic strain. Because the size of the precipitates we simulate are nanoscale, for which elastic deformation is relatively small compared to larger coherent particles, we make a simplifying assumption of linear elasticity to model the mechanical behavior of the system. Linear elasticity has previously been incorporated into phase field models of γ-hydrides in α-zirconium [60--62]. In Section 2.2.3, we discuss how we model relaxation of the misfit strain, as we do not assume that all the misfit is retained between the hydride and matrix.

The solid mechanics model determines the elastic strains in the system. Mechanical equilibrium is assumed at each time step such that

$$\frac{\partial \sigma_{ij}(\mathbf{r})}{\partial x_i} = 0 \tag{2.2.21}$$

where$\sigma_{ij}(\mathbf{r})$ is the elastic stress tensor components at point $\mathbf{r}$ (for which the indices vary from 1 to 3), and the equation is expressed in Einstein summation notation. The constitutive relationship for linear elasticity that relates the elastic stress and the elastic strain is

$$\sigma_{ij}(\mathbf{r}) = C_{ijkl}(\mathbf{r})\,\epsilon^{el}_{kl}(\mathbf{r}), \tag{2.2.22}$$

where C_{ijkl} is the stiffness tensor, which may be dependent upon temperature, and ϵ^{el}_{kl} is the elastic strain. Because the lattice parameters are different between the two phases, the elastic strain differs from the total strain as [133]

$$\epsilon^{el}_{kl}(\mathbf{r}) = \epsilon^{total}_{kl}(\mathbf{r}) - \epsilon^{0}_{kl}(\mathbf{r}) \tag{2.2.23}$$

where $\epsilon^{0}_{kl}(\mathbf{r})$ is the local stress-free strain tensor (i.e., strain measured with respect to the reference lattice). Therefore, stress-free lattice expansions do not contribute to elastic energy. The total strain is related to the displacement, u_i, as [133]

$$\epsilon^{total}_{kl}(\mathbf{r}) = \frac{1}{2}\left[\frac{\partial u_k(\mathbf{r})}{\partial x_l} + \frac{\partial u_l(\mathbf{r})}{\partial x_k}\right]. \tag{2.2.24}$$

Thus, the total elastic energy of the system is given as

$$G_{elastic} = \int_V g_{elastic}(X, \eta, T)\, dV = \frac{1}{2}\int_V C_{ijkl}(\mathbf{r})\,\epsilon^{el}_{ij}(\mathbf{r})\,\epsilon^{el}_{kl}(\mathbf{r})\, dV. \tag{2.2.25}$$

Due to numerical considerations, we assume that C_{ijkl} is homogeneous between phases. The stiffness tensor values are set to take that of α-zirconium [134], as done previously

in phase field modeling of γ-hydrides in α-zirconium [60--63] This approximation was incorporated to avoid spurious checkerboard patterns that develop in the stresses and strains of the precipitate when performing finite element calculations with heterogeneous stiffnesses between phases [135]. The issue likely arises from the near-incompressibility of the precipitate, causing spurious pressure modes and/or element locking [135]. Although formulations do exist to avoid this numerical problem [135--137], they are non-trivial to apply. In addition, while the elastic properties of α-zirconium have been extensively measured, [134], those of δ-hydride have not been well characterized. The C_{ijkl} values for δ-hydride have been calculated at 0 K [138] and are similar to the measured values for α-zirconium at 4 K [134]. The Young's modulus of δ-hydride has been measured at ambient temperature, and was found to be only slightly stiffer than α-zirconium [139--143]. However, the elastic properties of both α-zirconium and δ-hydride display strong temperature dependencies [134,140], and thus there is significant uncertainty in the elastic constants of δ-hydride at the elevated temperatures simulated in this work. Therefore, we assume that the δ-hydride stiffness tensor can be approximated by that of α-zirconium.

Misfit strain relaxation

In the model presented here, $\epsilon^0_{kl}(\mathbf{r})$ accounts for both matrix/hydride misfit strains and for the dilational effect of interstitial hydrogen in solution with α-zirconium, similar to the formulation in Ref. [63]. The misfit strain tensor is given as a linear combination of the stress-free transformation strains of the two phases,

$$\epsilon^0_{kl}(\mathbf{r}) = \left[\left(1-\eta^2(\mathbf{r})\right) X(\mathbf{r})\,\lambda_{kl} + \left(\eta^2(\mathbf{r})\right)(1-\psi)\,\epsilon^{misfit}_{kl}\right], \tag{2.2.26}$$

where ϵ_{kl}^{misfit} is the temperature-dependent misfit strain of δ-hydride with respect to pure α-zirconium [26], X is the atomic fraction of hydrogen, λ_{kl} is the local distortion tensor created by an interstitial hydrogen atom in solution with α-zirconium [144,145], which is assumed to be temperature-independent, and ψ is the fraction of misfit strain relieved by misfit dislocations, which will be described further below. The interpolation functions, $\left(1-\eta^2\left(\mathbf{r}\right)\right)$ and $\eta^2\left(\mathbf{r}\right)$, are chosen following Refs. [63,146].

As discussed previously, the elastic strains reported in Ref. [28] are significantly larger than the macroscopic yield strain, but some plastic deformation was also observed around the precipitates. Therefore, the relaxation factor, ψ, was incorporated into Eq. 2.2.26 to approximate the effect of coherency loss between the hydride and matrix by reducing the values of ϵ_{kl}^{misfit}. This factor represents the fraction of the misfit strain that is not relieved by interfacial dislocations and takes a value between zero and one, where zero indicates no misfit strain relaxation and unity indicates total relaxation of the misfit strain. Semi-coherent precipitates are indicated by intermediate values of ψ. This formulation assumes that no dislocations reside in the bulk of the matrix or the hydride. Decreasing the value of ϵ_{kl}^{misfit} by ψ is similar to the methods proposed in Refs. [147,148] to account for the effect of interfacial dislocations in a phase field model. In these works, a plastic strain tensor is subtracted from the misfit strain tensor, reducing the misfit strain tensor values and the calculated elastic strain.

The relaxation of ϵ_{kl}^{misfit} will have a concomitant effect on the interfacial energy between the α and δ phases. While quantitative values of the α/δ interfacial energies are not available in the literature, the interfacial energy is estimated as [149]

$$\gamma = \gamma_{ch} + \gamma_{st}, \tag{2.2.27}$$

where γ_{ch} is the chemical energy of the interface (calculated in Ref. [150] for other coherent hydride phases) and γ_{st} is the energy due to the presence of dislocations reducing the misfit strain between the α and δ phases. The dislocation contribution to the interfacial energy is obtained in Refs. [149, 151] as $\gamma_{st} \approx \frac{1}{2} S b \epsilon^0$, where S is the shear modulus of zirconium, b is the Burgers vector of a dislocation, roughly equal to the lattice constant of δ-hydride, and ϵ^0 is the average α/δ misfit strain. However, as mentioned in Section 2.2.3, the misfit strain is not fully relieved by interfacial dislocations for nanoscale hydrides [28]. To model this case, ψ is incorporated into γ_{st}. The dislocation contribution to the interfacial energy is modeled as

$$\gamma_{st} \approx \frac{1}{2} S b \psi \epsilon^0 \tag{2.2.28}$$

where S is the shear modulus of zirconium, b is the Burgers vector of a dislocation, roughly equal to the lattice constant of α-hydride, and ϵ^0 is the average α/δ misfit strain [27]. A fully coherent interface and a fully relaxed interface are represented by $\psi = 0$ and $\psi = 1$, respectively. A larger ψ indicates a higher density of dislocations and thus a smaller dislocation spacing.

2.2.4 Nucleation model

Nucleation and growth are key phenomena in phase transformations such as solidification and solid-solid precipitation. Nucleation behavior can have a major impact on the resulting microstructure and material properties. For example, precipitation hardening of alloys involves the formation of second-phase particles. The mechanical properties of such materials are dependent on precipitate size and spatial distribution; these characteristics

are controlled in part by the nucleation behavior [152]. Thus, modeling of nucleation and growth is of major technological and scientific importance for materials development and design [153, 154].

An introductory discussion of the various methods to incorporate nucleation into phase field models is given in Section 2.2.3. In the multiphysics phase field model of the α-zirconium/δ-hydride system, the method introduced by Simmons et al. [155] is chosen. Hereafter, this method will be referred to as the explicit nucleation algorithm. In addition, a discussion of classical nucleation theory is presented along with parameterization for the α-zirconium/δ-hydride system.

Methods to incorporate nucleation into phase field models

The formulation of the evolution equations in the phase field model precludes the occurrence of activated processes such as nucleation. Nucleation is commonly handled in one of two approaches within a phase field model [74], though other approaches exist as well. In the first method, a random noise term satisfying the fluctuation-dissipation theorem, ζ_n, is added to the time evolution equation to model atomic-scale thermal fluctuations, e.g.,

$$\frac{\partial n}{\partial t} = -L_n \frac{\delta G}{\delta n} + \zeta_n \tag{2.2.29}$$

for the Allen-Cahn equation. These fluctuations give rise to homogeneous nucleation [156]. However, the spatial and temporal resolutions required to accurately describe these fluctuations are computationally prohibitive with existing resources except for when modeling extremely small volumes. In practice, unphysically large random noise is often used in the early stage of a simulation to induce the formation of second phase

particles. After their formation, the noise is deactivated and growth of the particles ensues [156--158]. Similarly, heterogeneous nucleation on microstructural defects and walls has been modeled by the use of white- and colored-noise terms in the evolution equation [159].

An alternative to the aforementioned noise-based methods is explicit introduction of nuclei into the phase field simulation. In this method, classical nucleation theory is applied to a phase field model described by coupled conserved-nonconserved order parameters [155]. The local nucleation probability for each discretized volume in the simulation is calculated as a function of the local nucleation rate, and nucleation occurs stochastically as a function of the local nucleation probability. If nucleation occurs, a supercritical nucleus is introduced into the simulation by changing the value of the local composition field. To satisfy mass conservation, a depletion region around the nucleus must be created in the composition field. The algorithm was initially implemented with a depletion region described by a discontinuous concentration profile [155]. In subsequent work, a depletion region profile derived from the Zener gradient approximation [160] was demonstrated. This method was further modified by introducing a diffusion smoothing step after nucleus introduction [161] to create a smooth composition gradient at the nucleus/matrix interface.

Several other phase field treatments of nucleation exist in addition to the two aforementioned approaches. Microscopic phase field formulations of heterogeneous nucleation on defects were developed, in which the energy of a defect, such as a dislocation, is added into the local free energy to induce nucleation on the defect [162, 163]. In addition, several researchers have developed methods to numerically determine the critical nucleus shape. In one approach, the critical nucleus profile under solidification conditions

was determined by finding the time-independent solutions of the phase field evolution equations for a given concentration [164]. To obtain the shapes of critical nuclei in solid-solid phase transformations, which could deviate from a spherical shape due to elastic effects, both the nudged elastic band method [165] and the minimax technique have been utilized [166--168].

Classical nucleation theory

According to classical nucleation theory, the formation of a coherent precipitate nucleus involves an increase in the free energy due to the creation of an interface between the matrix and the second phase, a decrease in the chemical free energy due to the phase transformation, and an increase in the free energy due to elastic strain arising from misfit, if any. The change in free energy due to the formation of a nucleus, $\Delta G^{nucleus}$, is given as [152]

$$\Delta G^{nucleus} = -V_p \Delta g_{chem} + A\gamma_{nuc} + \Delta E_{elastic} \tag{2.2.30}$$

where Δg_{chem} is the chemical energy change per unit volume of the phase transformation, V_p and A are the volume and surface area of the nucleus, respectively, and γ_{nuc} is the interfacial energy between the nucleus and the matrix. In addition, $\Delta E_{elastic}$ is the change in the total elastic strain energy of the system from the pre-nucleation to the post-nucleation state. In this thesis, a spherical nucleus and isotropic interfacial energy are assumed. Equation 2.2.30 may be re-written as [152]

$$\Delta G^{nucleus} = -V_p \left(\Delta g_{chem} - \Delta \bar{g}_{el}\right) + A\gamma_{nuc} \tag{2.2.31}$$

where $\Delta\bar{g}_{el} = \Delta E_{elastic}/V_p$; i.e., the total elastic strain energy change of the system is converted to an average energy density for the nucleus. This conversion may be used if $\Delta E_{elastic}$ is proportionate to V_p. For a given hydrogen concentration in the matrix, the $\Delta\bar{g}_{el}$ term will reduce the driving force for nucleation because it is positive. The Δg_{chem} term for a two-component system such as α-zirconium/δ-hydride is calculated as [169]

$$\Delta g_{chem} = \frac{1}{\Omega_0}\left[G^{0,\alpha}_{mix}\left(X_0, T\right) - G^{0,\delta}_{mix}\left(X_p, T\right) + \left(X_p - X_0\right)\frac{dG^{0,\alpha}_{mix}}{dX}|_{X_0}\right] \tag{2.2.32}$$

where X_0 is the atomic fraction of solute in the matrix phase and X_p is the composition of the precipitate phase. Figure 2.2.1 schematically illustrates Δg_{chem} for a two-component system. For a supersaturated solution, Δg_{chem} will take a positive value.

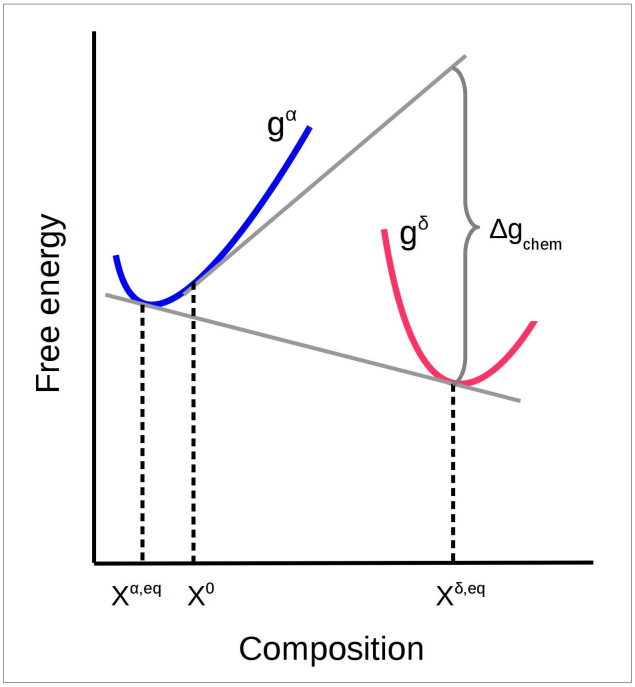

Figure 2.2.1: Illustration of Δg_{chem}, the volumetric chemical driving force of nucleation from the matrix. $X^{\alpha,eq}$ and $X^{\delta,eq}$ are the equilibrium compositions of the α and δ phases, respectively, while X^0 is the initial composition of the supersaturated matrix.

To calculate $\Delta\bar{g}_{el}$, the change in the total elastic energy of the system due to the presence of a new nucleus must be found. The change in the total elastic energy of the system may be considered as the sum of two components [170, 171],

$$\Delta E_{elastic} = \Delta E_{elastic}^{self} + \Delta E_{elastic}^{interaction}, \tag{2.2.33}$$

where $\Delta E_{elastic}^{self}$ is the change in elastic energy from the constrained nucleus and $\Delta E_{elastic}^{interaction}$ is the change in elastic energy due to the interaction of the nucleus with the existing stress state arising from the microstructure and boundary stresses. The $\Delta E_{elastic}^{self}$ term is equal to the elastic energy of a coherent spherical precipitate in an infinite matrix, which may be found numerically. Division of $\Delta E_{elastic}^{self}$ and $\Delta E_{elastic}^{interaction}$ by the volume of the precipitate for which it was computed gives $\Delta\bar{g}_{elastic}^{self}$ and $\Delta\bar{g}_{elastic}^{interaction}$, respectively. For the introduction of a nucleus at a given position $\mathbf{r}$, the change in the interaction energy may be approximated as [170, 171]

$$\Delta E_{elastic}^{interaction} \approx -V_p \sigma_{ij}\left(\mathbf{r}\right) \epsilon_{ij}^{misfit} \tag{2.2.34}$$

assuming that the stress within the precipitate is uniform. Equation 2.2.34 may be re-written as an energy density as $\Delta\bar{g}_{elastic}^{interaction} = -\sigma_{ij}\left(\mathbf{r}\right) \epsilon_{ij}^{misfit}$, such that size dependence of the nucleus is eliminated. Therefore, the average volumetric elastic energy change may also be given as

$$\Delta\bar{g}_{el} = \left(\Delta\bar{g}_{elastic}^{self} - \sigma_{ij}\left(\mathbf{r}\right) \epsilon_{ij}^{misfit}\right). \tag{2.2.35}$$

At the critical size, the nucleus is in unstable equilibrium. The critical nucleus activation energy, ΔG^{*}, describes the minimum energy barrier that must be overcome to form a

critical nucleus. The shape of the nucleus and the interfacial energy must be known or assumed to calculate the critical activation energy. At the critical nucleus radius r_C, ${}^{d\Delta G^{nucleus}}/_{dr} = 0$ such that

$$r_C = \frac{2\gamma_{nuc}}{\Delta g_{chem} - \Delta \bar{g}_{el}}. \tag{2.2.36}$$

By substituting Eq. 2.2.36 into Eq. 2.2.31, the critical nucleus activation energy is found as

$$\Delta G_C = \frac{16\pi}{3} \frac{\gamma_{nuc}^3}{\left(\Delta g_{chem} - \Delta \bar{g}_{el}\right)^2}. \tag{2.2.37}$$

The nucleation rate may be calculated as a function of the critical nucleus activation energy. The local nucleation rate for critical nuclei in a given volume, $J_C\left(t\right)$, is calculated following classical nucleation theory [96] as

$$J_C\left(\mathbf{r}, t\right) = ZN\beta_C \exp\left(\frac{-\Delta G_C}{k_B T}\right) \exp\left(\frac{-\tau}{t}\right), \tag{2.2.38}$$

where Z is the Zeldovich correction factor, N is the number of solute atoms in the volume [172], β_C is the frequency at which a critical nucleus becomes supercritical, related to the attachment rate of hydrogen to the hydride, T is the temperature, k_B is the Boltzmann constant, τ is the incubation time, and t is the time. This may be rewritten as

$$J_C\left(t\right) = Zn\Delta v\beta_C \exp\left(\frac{-\Delta G_C}{k_B T}\right) \exp\left(\frac{-\tau}{t}\right), \tag{2.2.39}$$

where $N = n\Delta v$, Δv is the volume, and n is the number density of solute atoms. To obtain a volumetric nucleation rate, $J_{C,V}$, the volume is eliminated from the previous equation such that

$$J_{C,V}\left(\mathbf{r},t\right)=Zn\beta_C\exp\left(\frac{-\Delta G_C}{k_BT}\right)\exp\left(\frac{-\tau}{t}\right). \tag{2.2.40}$$

Simmons et al. pioneered the development of an algorithm that explicitly introduces nuclei in a phase field simulation based on classical nucleation theory [155]. In this method, a nucleation probability is introduced, which follows a first-order decay relationship with respect to the nucleation rate. The local nucleation probability in a volume Δv, $P\left(t\right)$, is calculated as [155]

$$P\left(t\right)=1-\exp\left(-J_{C,V}\Delta v\Delta t\right), \tag{2.2.41}$$

where Δt is the time interval over which the nucleation probability is calculated.

In the α-zirconium/δ-hydride model, the incubation time, τ, is neglected because it is assumed that nucleation is in the steady-state regime [96, 155]. The Zeldovich correction factor accounts for the fact that every critical nucleus does not become a supercritical nucleus and that the number of nuclei present in reality is less than that in equilibrium conditions [96, 169]. The Zeldovich factor is calculated as [172]

$$Z=\frac{V_\alpha\left(\Delta g_{chem}-\Delta\bar{g}_{el}\right)^2}{8\pi\sqrt{\gamma^3k_BT}}, \tag{2.2.42}$$

where V_α is the volume per atom in the matrix. In addition, the frequency factor β_C is calculated as [96]

$$\beta_C=z_cX_B^\alpha v_c\exp\left(\frac{-G^m}{k_BT}\right) \tag{2.2.43}$$

where $z_cX_B^\alpha$ is the number of solute atoms in the matrix surrounding the critical nucleus that may jump onto the critical nucleus, z_c is the total number of sites in which the

solute may sit, X_B^α is the atomic fraction of solute in the matrix, v_c is the frequency of the aforementioned jump, and G^m is the activation energy for the jump. Because several of the quantities in Eq. 2.2.43 are difficult to measure, Eq. 2.2.43 is approximated as [172]

$$\beta_C \approx \frac{16\pi\gamma^2 XD}{\left(\Delta g_{chem} - \Delta \bar{g}_{el}\right)^2 a^4} \tag{2.2.44}$$

where D is the solute diffusivity in the matrix [131] and a is the lattice parameter of δ-hydride [23].

2.2.5 Nondimensionalization of the equations

The governing equations are nondimensionalized in this work, which improves numerical behavior by ensuring all quantities are within approximately an order of unity. The nondimensionalization method adopted here follows that presented in Ref. [173]; the solid mechanics equations are also nondimensionalized. Characteristic scale values for the system's length, energy, and time are defined, and the equations are nondimensionalized using these values. The characteristic length scale was set to $l = 1 \times 10^{-9}$ m so that nucleation and early growth may be simulated. The characteristic volumetric energy scale was the peak driving force for transformation between the α and δ phases at 600 K, $|\Delta g| = 4.0 \times 10^8\ \mathrm{J/m^3}$. In addition, while no experimental information exists for the Allen-Cahn kinetic coefficient, $L = 1 \times 10^{-5}\mathrm{m^3\,J^{-1}s^{-1}}$ was chosen to maintain a diffusion-controlled transformation [113]. The relationships between the dimensional and dimensionless quantities are presented in Table 2.2, in which the dimensionless quantities are denoted with an asterisk.

Table 2.2: Nondimensionalization expressions for quantities within the α-zirconium/δ-hydride phase field model.

Quantity	Nondimensionalization expression
Time	$t^* = L\lvert\Delta g\rvert t$
Length	$r^* = r/l$
Hydrogen mobility	$M^* = M\Omega_0/\left(Ll^2\right)$
Allen-Cahn kinetic coefficient	$L^* = L/L \equiv 1$
Hydrogen atomic fraction gradient coefficient	$\kappa_X^* = \kappa_X/\left(\lvert\Delta g\rvert l^2\right)$
Structural order parameter gradient coefficient	$\kappa_\eta^* = \kappa_\eta/\left(\lvert\Delta g\rvert l^2\right)$
Chemical energy density	$g_{chem}^* = g_{chem}/\lvert\Delta g\rvert$
Elastic energy density	$g_{el}^* = g_{el}/\lvert\Delta g\rvert$
Stress	$\sigma_{ij}^* = \sigma_{ij}/\lvert\Delta g\rvert$
Elastic stiffness	$C_{ijkl}^* = C_{ijkl}/\lvert\Delta g\rvert$
Nucleation rate	$\left(J_{C,V}\right)^* = J_C l^3/\left(L\lvert\Delta g\rvert\right)$

2.3 Numerical methods

In this thesis, the finite element method was used to numerically solve the governing equations of the multiphysics phase field model (Eqs. 2.2.13, 2.2.14, 2.2.20 and 2.2.21). The finite element method is among the numerical techniques used to solve differential equations, which include the finite difference method and the finite volume method [174, 175]. While many variants exist, all finite element methods share two key principles [176]: 1) the domain over which the differential equation is solved is divided into a finite number of subdomains, termed elements, and 2) the differential equation is solved in its

variational form. This approach provides approximated solutions for differential equations without closed-form solutions.

2.3.1 Mathematical formulation of the finite element method

An excellent reference on the finite element method is *Finite Elements: An Introduction*, by E. C. Becker, G. F. Carey, and J. T. Oden [176], and its introduction to the finite element method is briefly summarized here. The symmetric Galerkin formulation is described, although other formulations exist. We start with a differential equation written in its strong form and its boundary conditions. For illustration, a simple one-dimensional differential equation is used as an example [176],

$$\begin{aligned} -u'' + u &= x, \qquad 0 \leq x \leq 1 \\ u(0) &= 0, \qquad u(1) = 0 \end{aligned} \tag{2.3.1}$$

along with its domain and boundary conditions, in which $u(x)$ is the solution and the number of prime marks indicate the order of the derivative (i.e., $u'' = d^2u/dx^2$). In the strong form, u must satisfy Eq. 2.3.1 at every point within the domain over which the equation is defined. However, this requirement is often too mathematically restrictive for many differential equations that model physical systems [176]. Therefore, the differential equation is recast into its weak or variational form, which reduces the requirements on the solution [176]. In addition, the variational form allows the differential equation to be approximated in such a way that linear algebra techniques may be applied to solve the

equation, for which computational methods exist.

When a differential equation is recast in its variational form, the differential equation is multiplied by a test function and then integrated such that the differential equation and its boundary conditions are satisfied in an average sense [176]. Equation 2.3.1 is written in variational form as

$$\int_0^1 \left(-u'' + u\right) v \, dx = \int_0^1 xv \, dx, \tag{2.3.2}$$

where v, the test function, is a function of x that is sufficiently differentiable and whose value vanishes at the edges of the domain [176]. Upon collection of terms to the left hand side, one obtains

$$\int_0^1 \left(-u'' + u - x\right) v \, dx = 0. \tag{2.3.3}$$

All of the terms are collected on the left hand side so that the roots of the equation may be found. At this point, the concept of the residual function of the differential equation is introduced. The residual, $R\left(x\right)$, is given as

$$R\left(x\right) = -u'' + u - x \tag{2.3.4}$$

and is the error of the partial differential equation. If the residual is non-zero (within some tolerance), then Eq. 2.3.3 is not satisfied and the proposed u is not the solution [176].

While Eq. 2.3.3 is a valid variational formulation, it is preferable that the same order of u and v appear within the variational equation [176]. To achieve this, integration by parts is performed (i.e., the Divergence Theorem is applied) to the second-order term in Eq. 2.3.3 to obtain [176]

$$\int_0^1 -u''v\,dx = \int_0^1 u'v'\,dx - u'v\Big|_0^1 \tag{2.3.5}$$

where $u'v|_0^1 = 0$ for v vanishing on the edges of the domain as a result of the Dirichlet boundary condition of zero that was chosen. Therefore, Eq. 2.3.3 is re-written as

$$\int_0^1 \left(-u'v' + uv - xv\right)\,dx = 0. \tag{2.3.6}$$

The variational formulation, Eq. 2.3.6, must be discretized to be solved numerically. A function, f, may be represented as an infinite series [176] as

$$f(x) = \sum_{n=1}^{\infty} \beta_n \theta_n(x) \tag{2.3.7}$$

where θ_n is some differentiable function, termed a basis function, and β_n is the n^{th} coefficient, which is known. The function may be discretized for a finite number of terms as [176]

$$f_N(x) = \sum_{i=1}^{N} \beta_i \theta_i(x). \tag{2.3.8}$$

Therefore, the test function is discretized for a finite number of terms as [176]

$$v_N(x) = \sum_{i=1}^{N} \beta_i \theta_i(x), \tag{2.3.9}$$

and the discretized trial function is represented as [176]

$$u_N(x) = \sum_{i=1}^{N} \alpha_i \theta_i(x) \tag{2.3.10}$$

where α_i is the unknown i^{th} order coefficient and θ_i is the same shape function used in Eq. 2.3.9 [176]. The Galerkin approximation method seeks an approximate solution to Eq. 2.3.6 by using the same basis functions for the test and trial functions and by summing a finite number of terms.

Therefore, the approximated differential equation is given as

$$\int_0^1 \left(-u'_N v'_N + u_N v_N - x v_N\right)\, dx = 0 \tag{2.3.11}$$

and u_N is determined upon determination of the α_i coefficients, which are referred to as the degrees of freedom of the approximation [176].

To determine the values of α_i, Eqs. 2.3.9 and 2.3.10 are inserted into Eq. 2.3.11 to obtain

$$\begin{aligned} \int_0^1 \Bigg\{ \frac{d}{dx}\left[\sum_{i=1}^{N} \beta_i \theta_i(x)\right] \frac{d}{dx}\left[\sum_{j=1}^{N} \alpha_j \theta_j(x)\right] \\ + \left[\sum_{i=1}^{N} \beta_i \theta_i(x)\right]\left[\sum_{j=1}^{N} \alpha_j \theta_j(x)\right] - x\left[\sum_{i=1}^{N} \beta_i \theta_i(x)\right] \Bigg\} dx &= 0 \end{aligned} \tag{2.3.12}$$

for all β_i, $i = 1...N$. By factoring β_i from Eq. 2.3.12 and re-writing $d\theta_i(x)/dx = \theta'_i(x)$,

$$\sum_{i=1}^{N} \beta_i \left(\sum_{j=1}^{N} \alpha_j \left\{ \int_0^1 \left[\theta'_i(x)\, \theta'_j(x) + \theta_i(x)\, \theta_j(x) \right] dx \right\} - \int_0^1 x \theta_i(x)\, dx \right) = 0 \tag{2.3.13}$$

is obtained. Finally, Eq. 2.3.13 is compactly expressed as

$$\sum_{i=1}^{N} \beta_i \left(\sum_{j=1}^{N} K_{ij} \alpha_j - F_i \right) = 0 \tag{2.3.14}$$

where

$$K_{ij} = \int_0^1 \left[\theta'_i(x)\, \theta'_j(x) + \theta_i(x)\, \theta_j(x) \right] dx, \tag{2.3.15}$$

which is commonly called the stiffness matrix, and

$$F_i = \int_0^1 x\theta_i(x)\ dx \tag{2.3.16}$$

is commonly called the force vector, where $i, j = 1...N$. Upon examination of Eq. 2.3.14, the matrix nature of the discretization of the variational formulation becomes evident.

Several additional key concepts exist within finite element modeling. First is the concept of the mesh (Fig. 2.3.1a), which is the collection of elements and nodes that represents the domain over which the differential equation is solved. The coefficients α_j in Eq. 2.3.13 are solved for at the nodes, such that the value of u_N at that point is found by multiplying the value of α_j with the value of its basis function θ_j. The value of u_N between the nodes may be found by interpolation. An element has a certain geometry and contains nodes, that may be at the vertices of the element or within the element. An element is characterized by its geometry, such as a triangular, shell, or hexahedral shape, and the ''shape function'', which interpolates the solution between the elements. Many different element geometries exist, which are useful for generating different mesh geometries and for modeling different types of problems.

Basis functions are used to represent the solution over the entire computational domain. Each basis function is piecewise-defined such that it is non-zero over a small number of elements and is zero over all other elements (Fig. 2.3.1b). The non-zero portion of the basis function is composed of a simple shape function whose form is used for all the basis functions. There are many types of shape functions available, and the choice of shape

function is determined by the type of problem being modeled [176]. The order of the shape function and its specific functional form must be selected according the requirements of the differential equations (i.e., a fourth-order equation may not be modeled using first-order shape functions). In addition, the computational resources required per element increase with the order of the shape function, but the mesh resolution requirements for a given level of accuracy may decrease with increasing shape function order. An example of a mesh with linear shape functions and the resulting solution is illustrated in Fig. 2.3.1c. Finally, the integration in Eq. 2.3.13 must be performed. This may be done exactly for simple shape functions and elements, or according to some quadrature rule (a rule describing the approximation of a definite integral) [176].

To model ever more complex problems with limited computational resources, mesh adaptivity is commonly used to place additional degrees of freedom at regions of the mesh in which the solution changes rapidly (i.e., that requires higher resolution) but remove degrees of freedom where less are needed to maintain a given level of accuracy. This type of adaptivity is termed h-adaptivity [177], in which the size of the elements is varied dynamically. In addition, p-adaptivity may also be used, in which the order of the shape functions is changed during the simulation [177]. As mentioned previously, higher-order shape functions provide greater accuracy for a given element size, but are more computationally expensive.

Typically, the differential equations solved via the finite element method are nonlinear. To solve the system of equations, some nonlinear solution-finding method is required that minimizes the residual to within a given tolerance. Two algorithms commonly used are the Newton-Raphson method and the Jacobian-Free Newton-Krylov (JFNK) method [178]. These algorithms are implemented in many libraries, including PETSc [179], the most

widely used parallel numerical software library for matrix computations in the world [180]. Both the Newton-Raphson method and the JFNK method are iterative in nature. Broadly speaking, a value for the variable close to the true solution of the function is guessed, and the value is updated with each iteration until the solution is found for which the residual is within some convergence tolerance (i.e., within some predefined level of error). Within each iteration, the problem is a approximated as a linear system of equations based on the Jacobian matrix (i.e., the matrix of the partial derivatives of the function), for which efficient computational solvers exist [178]. The JFNK method is attractive because the Jacobian matrix, whose expression is often not available analytically and can be computationally intensive to calculate, is not required [178].

2.3.2 MOOSE

While many finite element software packages exist, the Multiphysics Object Oriented Simulation Environment (MOOSE) framework [68, 181, 182] was used for the research presented in this thesis. MOOSE is a software framework to solve coupled, nonlinear partial differential equations [181,182] and is based on the parallel finite element framework libMesh [183]. MOOSE provides a core set of functionalities for solving physics-based partial differential equations. Physics-based problems share common features, and each feature is implemented as a core functionality. To simulate specific problems, a user may develop their own application based on MOOSE. Each functionality may be inherited from (i.e., built on top of) and modified by the user to code a specific equation or perform a specific code action. The modular nature of MOOSE is shown in Fig. 2.3.2. The core functionalities include ‘‘kernels’’, materials, auxiliary kernels, postprocessors, and time

integration, among others. Kernels implement the operators or terms within the partial differential equations to be solved. Materials provide materials-specific information to the rest of the software, such as atomic mobility, thermal conductivity, elastic stiffnesses, etc. Auxiliary kernels solve additional mathematics over the computational domain that are not part of the partial differential equations, while postprocessors analyze the simulation results after every time step and return a scalar value. To perform a simulation, an input file is supplied that specifies which kernels, materials, etc., are to be used, such that different physical behaviors and code outputs can be activated by including them in the input file.

MOOSE offers several advantages; in particular it is open-source and is free to download, compile, and use. MOOSE supports serial or parallel computation with adaptive time stepping and adaptive meshing, which can significantly reduce the computational resources required for large simulations. The physics implementation within MOOSE is dimensionally independent such that the same application code may be run in one, two, or three dimensions. In addition, multiphysics coupling in MOOSE is automatically built in to each functionality such that the values of any defined variables on an element are retrievable. Moreover, the object-oriented nature of MOOSE minimizes the need to re-implement common mathematical expressions when solving a new form of an equation. For example, implementing a new chemical potential within the Cahn-Hilliard equation requires only a few new lines of code. Furthermore, a set of built-in physics libraries (called ''modules'') provide general formulations for phase field equations and tensor-based solid mechanics that may be used directly or adapted for specific applications, amongst other types of physics. To minimize the chance that code updates introduce errors, MOOSE provides a means of testing user code for regressions or failures when parts of the framework are

updated. Finally, MOOSE has a large user base and a developer team who continue to implement new features, improve MOOSE, and provide support. More information about MOOSE may be found at `http://mooseframework.org` and the source code may be found at `http://github.com/idaholab/moose`.

2.3.3 Hyrax

Hyrax, the software built to perform the simulations of the α-zirconium/δ-hydride multiphysics phase field model, is based on MOOSE. Hyrax may be found online at `http://github.com/UMThorntonGroup/hyrax`. In this section, the core components of Hyrax are described, and the overall structure of Hyrax is schematically illustrated in Fig. 2.3.2. Several software terms that are part of the C++ language will be used throughout the discussion. ''Object-oriented'' software design means that the program design is based around the manipulation of ''objects'' instead of the traditional data flow that occurs within procedural programming. A ''class'' is a data type that is defined by the programmer; in addition to providing a data structure, a class may contain definitions of operations that may be performed. Objects are instances of a class. Objects consume computer memory and operations are performed using their data. Many objects of the same class may be created within a program.

Tensor Mechanics system

During the course of Hyrax development, it became evident that the existing solid mechanics module within MOOSE was insufficient to implement the solid mechanics for-

mulation in Section 2.2.3. The existing system was developed for isotropic materials and was later adapted for anisotropic materials, which proved to be error-prone and too inflexible. In collaboration with several scientists at Idaho National Laboratory and Argonne National Laboratory, I developed the Tensor Mechanics module within MOOSE. Tensor Mechanics is suite of classes based on the full tensor formulations of stress, strain, and elastic stiffness, and includes the kernels for the governing equation (Eq. 2.2.21). It is designed for ease of use with anisotropic crystals and for performing tensor rotations. After the incorporation of the Tensor Mechanics module into MOOSE, it has been expanded significantly by other developers, primarily by the addition of various plasticity models, and it is now widely used by the MOOSE community [184--186]. Further information about the Tensor Mechanics module may be found at `http://mooseframework.org/wiki/PhysicsModules/TensorMechanics`.

Kernels

As described in Section 2.3.2, kernels implement the partial differential equations to be solved. The discretizations of the weak forms of the Cahn-Hilliard and Allen-Cahn equations are implemented using the ''phase field'' module within MOOSE [68]. Specific expressions for $\partial g_{chem}/\partial X$, $\partial g_{chem}/\partial \eta$, $\partial g_{el}/\partial X$ and $\partial g_{el}/\partial \eta$ are implemented within Hyrax. The reduced-order split Cahn-Hilliard formulation is used in which Eq. 2.2.13 and Eq. 2.2.14 are solved without combining them into a single, higher-order partial differential equation [128, 130]. This approach offers significantly higher computational efficiency by allowing the use of lower-order elements as compared to the full fourth-order Cahn-Hilliard formulation [128, 130]. Further information about the development

of phase field models using MOOSE may be found at `http://mooseframework.org/wiki/PhysicsModules/PhaseField`.

Materials

Three types of material properties necessary to model the α-zirconium/δ-hydride system were implemented into materials classes in Hyrax. The first class type contains information for the parameters in the phase field model, such as M, L, κ_X, κ_η, w and Ω_0. The second class type contains information for the solid mechanics in the model. Parameters such as C_{ijkl}, ϵ_{ij}^{misfit}, λ_{ij}, and ψ as well calculated values such as $\sigma_{ij}(\mathbf{r})$, $\epsilon_{ij}^{el}(\mathbf{r})$, and $\epsilon_{ij}^{0}(\mathbf{r})$ are part of this class. The third class type is actually a set of classes that contain information for the CALPHAD free energies of mixing for the α-zirconium/δ-hydride system, which is schematically illustrated in Fig. 2.3.3. The common formulation of CALPHAD free energy equations (Eq. 2.2.3) allows code development to be streamlined by the creation of two base classes. The first base class, which is unique to Hyrax, evaluates the CALPHAD free energy and its derivatives for a given X and T (i.e., G_{mix}^0, $\partial G_{mix}^0/\partial X$, $\partial^2 G_{mix}^0/\partial X^2$). The second base class, which queries the first base class, holds the spatial field values of those energies and derivatives (i.e., $G_{mix}(\mathbf{r})$). These spatial field values are needed within the kernel classes and the classes involved with the nucleation algorithm. To include $G_{mix}^{0,\alpha}$ and $G_{mix}^{0,\delta}$ within Hyrax, classes specific to those energies were derived from the base classes.

Auxiliary kernels

The mathematical expressions for the nucleation model are computed within the auxiliary kernel system. Hyrax contains three types of auxiliary kernels to model nucleation. The first type computes the chemical driving force for nucleation, including Δg_{chem} and $\Delta \bar{g}_{el}$ (Eqs. 2.2.32 and 2.2.35). The second type computes the nucleation rate using the values calculated by the first auxiliary kernel. The third class computes the nucleation probability using the nucleation rate calculated by the second auxiliary kernel. The nucleation algorithm is described in detail in Chapter IV.

Additional code components for nucleation algorithm implementation

The incorporation of the explicit nucleation algorithm into Hyrax required the creation of several algorithms and code structures that were not previously present in MOOSE. The nucleation algorithm involves customized executioner, user object, and marker classes as well as a nucleus class that is unique to Hyrax. The nucleus class contains information for an individual nucleus introduced into the simulation, including its position and the time at which nucleation occurred. The entire explicit nucleation algorithm is controlled by a special executioner derived from the existing MOOSE executioner. The executioner defines the order that commands are performed within the simulation. The nucleation algorithm is shown schematically in Figure 2.3.4. Steps two and four are performed by user object classes unique to Hyrax. A user object class in MOOSE provides custom algorithms and data structures to any other system in MOOSE; the user object system, consisting of user object classes and how they link together with MOOSE, enables flexibility beyond that provided by the other MOOSE components. One user object class performs step two,

the determination of nucleation events, while the other user object class performs step four, the introduction of nuclei into the simulation. If mesh adaptivity is enabled, the list of nucleus positions stored within the first user object class is passed to a custom marker class. The marker tells the mesh refinement algorithm to refine elements at the positions of new nuclei so that the mesh has the appropriate local resolution.

2.4 Chapter summary

In this chapter, a multiphysics model was presented to describe the microstructural evolution of the α-zirconium/δ-hydride system and the numerical methods used to perform the simulations were detailed. The model incorporates the phase field method, solid mechanics and classical nucleation theory. In the first section, the phase field formalism was presented. A conserved field variable tracks the atomic fraction of hydrogen, and a nonconserved structural order parameter specifies the phase. The energetics of the system are described with CALPHAD-based free energies of mixing and linear-elastic solid mechanics, and an estimate for the interfacial energy was provided. The governing equations include the Cahn-Hilliard equation for hydrogen and the Allen-Cahn equation for the structural order parameter. A formulation for the mobility of hydrogen was given. In the next section, the solid mechanics formalism was presented. The model incorporates linear elasticity and accounts for the stress-free transformation strains of both δ-hydride and interstitial hydrogen in α-zirconium. In addition, the parameter ψ was introduced, which is a scaling factor applied to the stress-free transformation strain of δ-hydride as a simple method of approximating misfit strain relaxation via interfacial misfit disloca-

tions. In the last section, the nucleation model was presented, which is an extension of the explicit nucleation method developed by Simmons et al. [155]. Classical nucleation theory is applied to each discretized volume element in the simulation. If nucleation occurs, a nucleus is introduced into the simulation. The details of the formulation for the α-zirconium/δ-hydride system were presented. Finally, the nondimensionalization of the governing equations was given.

A review of the numerical methods utilized were presented in the last section. The finite element method was chosen to perform the multiphysics phase field simulations. In the finite element method, the domain over which the differential equation is solved is divided into a finite number of subdomains, termed elements, and the differential equation is solved in its variational form. An overview of the mathematical formulation was presented. In addition, a description of the application developed, Hyrax, was given. Hyrax is based on the Multiphysics Object Oriented Simulation Environment (MOOSE). The core components of MOOSE and Hyrax were described and information regarding further documentation was provided.

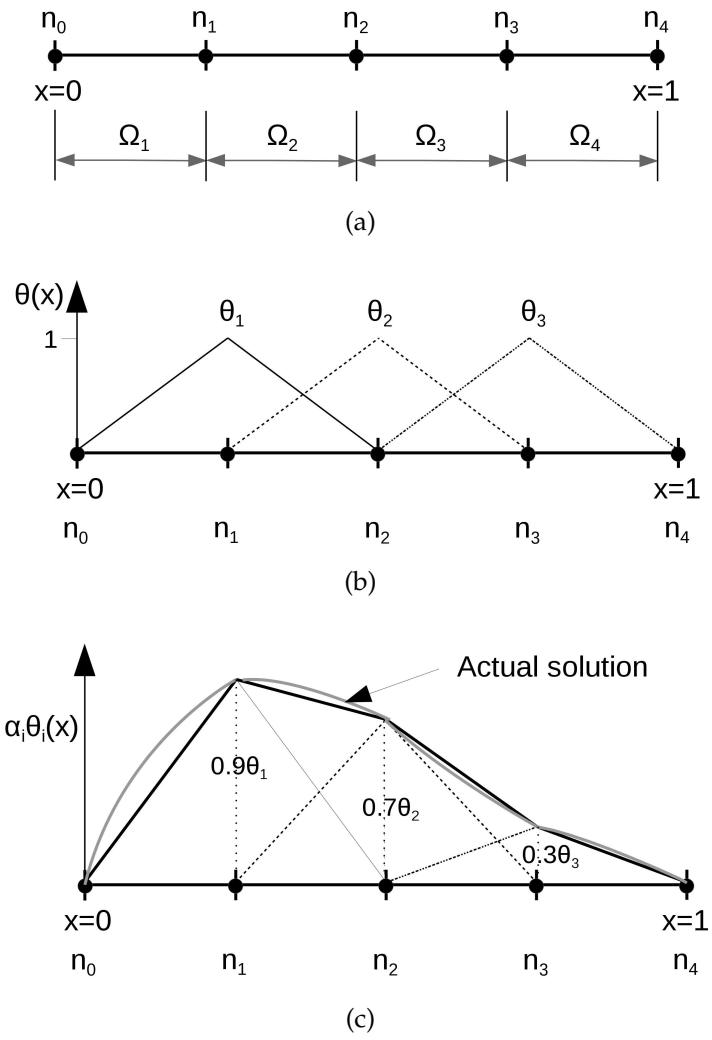

Figure 2.3.1: Illustrations of key finite element concepts. (a) A one-dimensional mesh with four elements (denoted by Ω_i) and five nodes (denoted by n_i). The total domain spans $0 \leq x \leq 1$. (b) An example of basis functions $\theta_i(x)$ for the elements. Each basis function is piecewise defined and composed of linear shape functions. (c) An example of an approximated solution. The value of the function at each node is the product of the nodal coefficient and the value of the shape function. Discretization error between the actual solution and the approximated solution will decrease with either increased resolution or higher order shape functions. Conceptualization from Ref. [176].

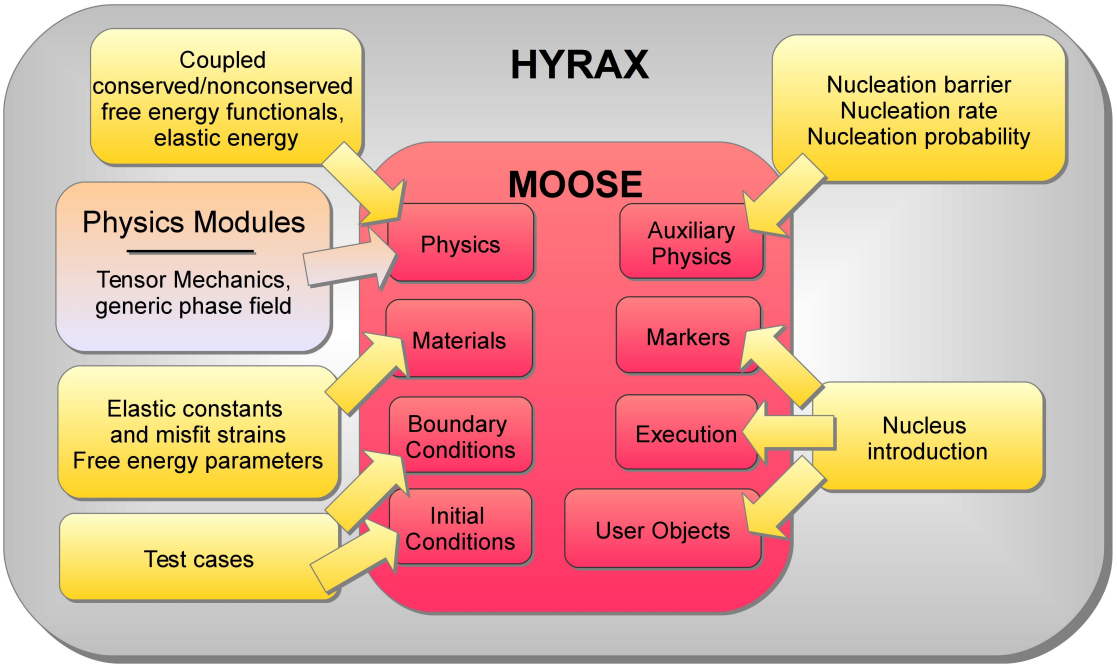

Figure 2.3.2: Schematic illustration of the overall code structure of Hyrax. The core MOOSE components are shown in red, and the code developed for Hyrax that falls under each category is shown in yellow.

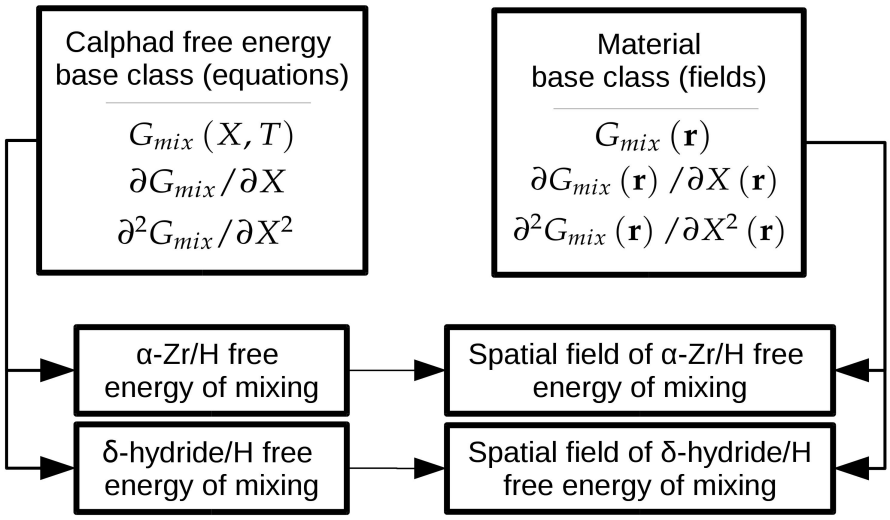

Figure 2.3.3: Schematic illustration of the set of materials classes within Hyrax that perform the calculation of the CALPHAD free energies of mixing for the α-zirconium/δ-hydride system. The classes in the left column compute the value of the free energy of mixing for a given composition and temperature, while the classes in the right column construct a field of those values over the computational domain.

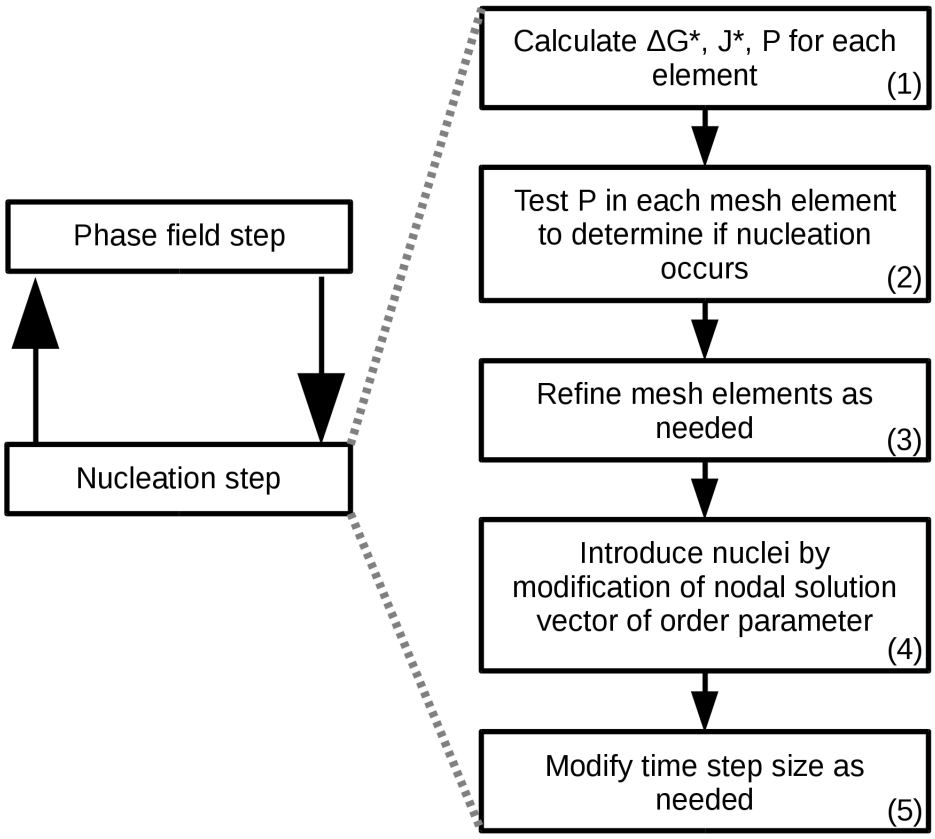

Figure 2.3.4: A flow chart of the order-parameter-only nucleation algorithm implemented within Hyrax. After a phase field time step, the nucleation algorithm is executed. (1) The nucleation activation energy, nucleation rate, and nucleation probability are calculated for each element. (2) The nucleation probability in each element is tested to determine if nucleation occurs. If mesh adaptivity is enabled, (3) mesh elements are refined as needed to obtain sufficient resolution for new nuclei. (4) The nodal solution vector for the order parameter is explicitly modified to reflect the formation of the new nuclei. (5) The time step size is modified as needed. Upon the completion of the nucleation step, the next phase field time step is executed.

CHAPTER III

General Method for Incorporating CALPHAD Free Energies of Mixing into Phase Field Models: Application to the α-Zirconium/δ-Hydride System

In this chapter, the algorithm and numerical challenges associated with the incorporation of CALPHAD-based free energies into the phase field model are discussed. While CALPHAD-based free energy descriptions provide realistic energetics of alloys, their formulations may pose numerical difficulties for phase field simulations. Specifically, the free energies of mixing for different phases may not necessarily be defined over the same concentration ranges, and their derivatives may exhibit highly nonlinear behavior. The method presented approximates the free energies of mixing using piecewise functions to eliminate the aforementioned characteristics while largely retaining the free energy values and the first and second derivative information, which also affect the thermodynamic and kinetic behavior of the system. The method is verified by planar interface simulations of the α-zirconium/δ-hydride system. The phase fractions and compositions obtained from the phase field simulations are compared to the values calculated from the common

tangent construction on the original free energies. The results indicate a high degree of accuracy.

3.1 Introduction

While CALPHAD-based free energy descriptions may provide realistic thermodynamic information, the presence of natural logarithm terms in their formulation poses numerical challenges for simulation. For example, Ref. [187] indicated the difficulty in performing phase field simulations at low vacancy concentrations for a TiAlN-vacancy system described by CALPHAD-based free energies. In addition, the free energies of mixing may only be defined over a finite concentration range of solute and their derivatives may exhibit undesirable asymptotic behavior. Furthermore, free energies of mixing for different phases may not be defined over the same concentration ranges (e.g., G^{α} may be defined over an atomic fraction range of $(0, 0.5)$, while G^{β} may be defined over $(0, 1)$). These attributes may be problematic for numerical simulations because solvers may attempt to compute a free energy for a concentration value outside the range for which it is defined. In many phase field models (e.g., the Wheeler-Boettinger-McFadden (WBM) [97], Kim-Kim-Suzuki (KKS) [188], or Welland-Wolf-Guyer (WWG) [189] models), free energy curves must be defined over a large composition range, even at compositions far from equilibrium. However, the computed mobility may be negative when it is calculated from the experimentally obtained diffusivities and the second derivative of the free energy (e.g., in the spinodal region). To avoid such a situation, the CALPHAD free energy must be modified.

Previously proposed methods of incorporating CALPHAD-based free energies into

phase field models include direct coupling to a thermodynamic database [105,190,191] or polynomial approximations of the free energies [113,192--195]. However, direct coupling may incur substantial computational expense by querying external software at each mesh point for every simulation step, and it may necessitate the use of commercial software, which may require costly licensing fees. Approximating the free energy as a polynomial expression alleviates the aforementioned computational cost, but a simple approximation may cause a loss of thermodynamic information. For example, Ref. [113] found that precipitate growth kinetics and the driving force for nucleation are sensitive to the parameterization of the free energy of the matrix and precipitate phases, respectively, in an Al-Cu system.

The α-zirconium/δ-hydride system is of technological importance, particularly for the fuel assemblies of nuclear power reactors. A CALPHAD-based description of the molar free energies of mixing for this system exists in the literature [98]. However, the free energies exhibit several characteristics that are problematic for phase field modeling, including the presence of natural logarithms arising from the entropic contribution to the free energy. In addition, the solubility limit of hydrogen in α-zirconium is low. Therefore, at low concentrations a numerical solver may attempt to compute a free energy for a hydrogen atomic fraction less than zero, resulting in undefined behavior due to the natural logarithm terms. Furthermore, the α-phase free energy of mixing is defined over a smaller composition range than that of the δ-phase, so that energy evaluations may occur outside the composition range of the α-phase but still within the composition range of the δ-phase.

In this chapter, a simple and efficient method of approximating CALPHAD-based free energies for phase field models is proposed. The approximation method was formulated to retain the original free energy in the composition ranges that are present in the evolving

system while alleviating numerical challenges. The approach is incorporated into a phase field model for the α-zirconium/δ-hydride system, which was chosen as a test system because it exhibits the characteristics described previously. Planar interface simulations were performed to verify the model. The equilibrium phase fractions and compositions from the simulations were compared to values obtained from the original CALPHAD free energies via a common tangent construction. In addition, an example of δ-hydride precipitate growth is discussed to demonstrate the flexibility of the method.

3.2 Methods

To incorporate a CALPHAD-based free energy functional in a phase field model, an implementation must effectively handle any instances where the free energies of mixing for the phases become undefined or discontinuous. These instances may be treated either by numerical exceptions or by modifying the functional such that it yields numerically acceptable behavior while retaining essential thermochemical information. In this work, we take the latter approach. Below, we first describe a general phase field model to provide the form of the free energy required. We then provide the generic framework for approximating the free energies of mixing.

3.2.1 General coupled conserved-nonconserved phase field model

In the phase field approach, the state of a two-phase system may be described using two field variables, as detailed in Chapter II. A conserved field variable, X, describes the atomic

fraction of solute, and a nonconserved structural field variable, η, tracks the structural transformation between the two phases. The free energy is expressed as

$$G = \int_V \left(g_{chem}\left(X, \eta, T\right) + \frac{\kappa_X}{2}|\nabla X|^2 + \frac{\kappa_\eta}{2}|\nabla \eta|^2 \right) dV, \tag{3.2.1}$$

where κ_η and κ_X are the gradient energy coefficients for the structural order parameter and atomic fraction, respectively, g_{chem} is the bulk chemical free energy density, T is the absolute temperature, V is the system volume. Additional energy contributions may be incorporated into the free energy as well. In phase field model formulations suited for incorporating CALPHAD-based free energies (including the Wheeler-Boettinger-McFadden [97], Kim-Kim-Suzuki [188] and Welland-Wolf-Guyer [189] models), the expression for g_{chem} is a combination of two single phase energies,

$$g_{chem} = \frac{1}{\Omega_0}\left[\left(1 - h\left(\eta\right)\right) G_{mix}^{0,\alpha} + h\left(\eta\right) G_{mix}^{0,\beta} + wk\left(\eta\right) \right], \tag{3.2.2}$$

where $G_{mix}^{0,\alpha}$ is the molar free energy of mixing for the solute in the α-phase and $G_{mix}^{0,\beta}$ is the molar free energy of mixing for the β-phase. Note that $G_{mix}^{0,\alpha}$ and $G_{mix}^{0,\beta}$ are dependent on composition and temperature, but their exact dependence varies depending on the phase field model employed (e.g., $G_{mix}^{0,\alpha}\left(X, T\right)$ for the WBM model and $G_{mix}^{0,\alpha}\left(X^\alpha, T\right)$ for the KKS model, where X^α is the composition in the α phase. In addition, Ω_0 is the molar volume, $h\left(\eta\right) = \eta^2\left(3 - 2\eta\right)$ is the interpolation function that increases monotonically from $h\left(0\right) = 0$ to $h\left(1\right) = 1$, $k\left(\eta\right) = \eta^2\left(\eta - 1\right)^2$ is the double well function, and w controls the height of the barrier, though other terms may contribute to the total energy barrier.

The microstructural evolution of the system is governed by coupled conserved-nonconserved dynamics [97]. The Cahn-Hilliard equation [81] governs the evolution of the atomic frac-

tion of solute. To reduce computational resource requirements, the Cahn-Hilliard equation may be split into two second-order equations [128, 129]. The time evolution of X is given by

$$\frac{1}{\Omega_0}\frac{\partial X\left(\mathbf{r},t\right)}{\partial t}=\nabla\cdot M\nabla\frac{\delta G}{\delta X}, \tag{3.2.3}$$

where M is the mobility, and

$$\frac{\delta G}{\delta X}=\frac{\partial g_{chem}}{\partial X}-\kappa_X\nabla^2 X. \tag{3.2.4}$$

When $\kappa_X = 0$, the form of the phase field model in Ref. [97] is recovered; note that a non-zero value of κ_X may be required to control the maximum gradient of X. In addition, the Allen-Cahn equation [94] governs the evolution of the structural order parameter as

$$\frac{\partial\eta\left(\mathbf{r},t\right)}{\partial t}=-L\frac{\delta G}{\delta\eta}=-L\left(\frac{\partial g_{chem}}{\partial\eta}-\kappa_\eta\nabla^2\eta\right), \tag{3.2.5}$$

where L is the kinetic coefficient.

3.2.2 Generic CALPHAD free energy approximation

In the CALPHAD method, a molar free energy of mixing in a single phase is expressed in the form

$$G^{0,i}_{mix}\left(X,T\right)=G^{0,i}_{ref}\left(X,T\right)+G^{0,i}_{ideal}\left(X,T\right)+G^{0,i}_{excess}\left(X,T\right), \tag{3.2.6}$$

as described in Chapter II. The equation for $G_{mix}^{0,i}$ presents several difficulties for numerical discretization. Depending on the exact energy formulation, the presence of the natural logarithm terms in $G_{ideal}^{0,i}$ may result in $G_{mix}^{0,i}$ not being defined over the entire atomic fraction range of $(0,1)$ but only a subset (e.g., $(0,0.5)$). For example, the sublattice model may encounter this issue. If $G_{mix}^{0,\alpha}$ and $G_{mix}^{0,\beta}$ are defined over different atomic fraction ranges, then the phase field formulation for the chemical free energy density (Eq. 3.2.2) may require calculation of energies outside the composition range of one $G_{mix}^{0,i}$ but within the composition range of the other. In addition, both $\partial G_{mix}^{0,\alpha}/\partial X$ and $\partial G_{mix}^{0,\beta}/\partial X$ exhibit highly nonlinear behavior near their composition bounds due to the natural logarithm terms in $G_{ideal}^{0,\alpha}$ and $G_{ideal}^{0,\beta}$. Finally, the numerical solution method may attempt to calculate energies for $X < 0$. Therefore, either numerical exception handling or free energy reformulation to avoid these undefined values is necessary.

To eliminate the instances in which Eq. 3.2.2 becomes undefined, we approximate $G_{mix}^{0,i}(X,T)$ as a piecewise function $\tilde{G}_{mix}^{0,i}(X,T)$, where $i = \alpha$ or β. This approximation is given by Eq. 3.2.7 and is schematically illustrated in Fig. 3.2.1. Each piecewise function $\tilde{G}_{mix}^{0,i}(X,T)$ is composed of three subfunctions that are defined on subdomains of X. The low and high subdomain boundary compositions (X_{low} and X_{high}, respectively) are chosen within the composition domain over which each $G_{mix}^{0,i}(X,T)$ is defined. These subdomain boundary compositions (collectively referred to as X_{bound}) must be selected to be sufficiently outside the composition range expected to be encountered in the physical system. The free energy for $X < X_{low}$ is approximated by the second-order Taylor expansion of $G_{mix}^{0,i}(X,T)$ around X_{low}, denoted as G_{Taylor}^{low}. Similarly, the second-order Taylor expansion of $G_{mix}^{0,i}(X,T)$ around X_{high} is used to approximate $G_{mix}^{0,i}(X,T)$ for $X > X_{high}$, denoted as G_{Taylor}^{high}. The resulting function retains the derivatives of the free energy

within the X_{bound} values and creates a new energy that is second-order differentiable for all composition and temperature ranges, as long as the original CALPHAD energies are second-order differentiable. The resulting expression for $\tilde{G}^{0,i}_{mix}(X,T)$ is given by

$$\tilde{G}^{0,i}_{mix}(X,T) = \begin{cases} G^{0,i}_{mix}(X,T)\,|_{X=X_{low}} \\ +\dfrac{\partial G^{0,i}_{mix}(X,T)}{\partial X}|_{X=X_{low}}(X-X_{low}) \\ +\frac{1}{2}\dfrac{\partial^2 G^{0,i}_{mix}(X,T)}{\partial X^2}|_{X=X_{low}}(X-X_{low})^2 & : X < X_{low} \\ G^{0,i}_{mix}(X,T) & : X_{low} \leq X \leq X_{high} \\ G^{0,i}_{mix}(X,T)\,|_{X=X_{high}} \\ +\dfrac{\partial G^{0,i}_{mix}(X,T)}{\partial X}|_{X=X_{high}}\left(X-X_{high}\right) \\ +\frac{1}{2}\dfrac{\partial^2 G^{0,i}_{mix}(X,T)}{\partial X^2}|_{X=X_{high}}\left(X-X_{high}\right)^2 & : X > X_{high}. \end{cases} \tag{3.2.7}$$

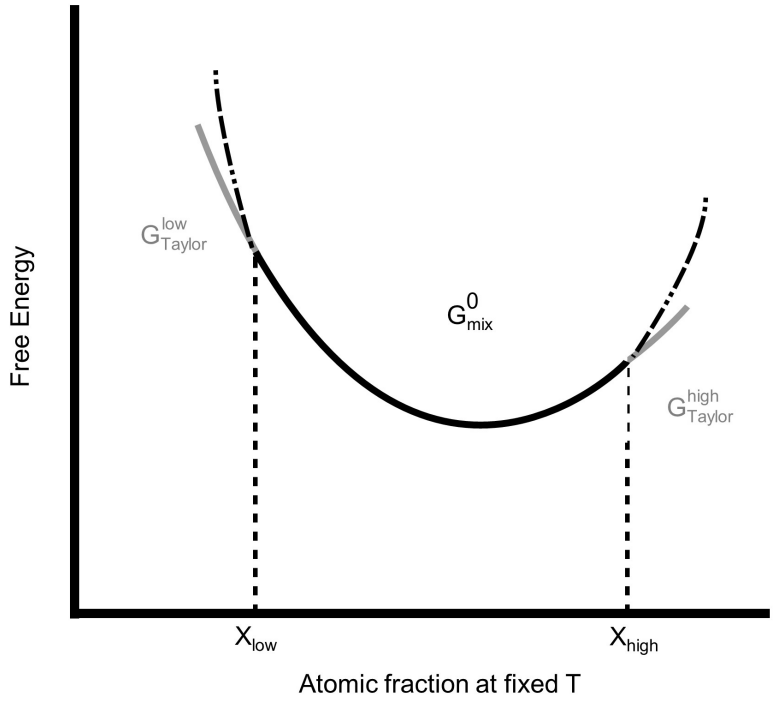

Figure 3.2.1: Schematic illustration of the approximation method. The original CALPHAD-based free energy is labeled $G^{0,i}_{mix}$ (black curve). At and below the subdomain boundary composition X_{low}, G^{low}_{Taylor} is substituted for $G^{0,i}_{mix}$, and at and above the composition X_{max}, G^{high}_{Taylor} is substituted (two gray curves). The functions G^{low}_{Taylor} and G^{high}_{Taylor} are the second-order Taylor expansions of $G^{0,i}_{mix}(X,T)$ at X_{low} and X_{high}, respectively. The approximated function $\tilde{G}^{0,i}_{mix}$ is given by the combination of the solid gray and black curves. The dashed lines indicate where $G^{0,i}_{mix}$ is discarded.

3.2.3 The α-zirconium/δ-hydride model

Phase field model formulation

The CALPHAD free energy approximation method is demonstrated for the α-zirconium/δ-hydride system. The model is presented in Chapter II and is summarized here for con-

venience. In this model, X is the atomic fraction of hydrogen and η tracks the structural transformation between the α-zirconium and δ-hydride phases, where $\eta = 0$ for the α phase and $\eta = 1$ for the δ phase. Zirconium hydride precipitation in zirconium induces elastic strains [28], but chemical and elastic energy contributions are typically incorporated separately in a phase field model [72]. Therefore, we neglect the elastic strain energy contribution in Eq. 3.2.1 in order to focus on the verification of the chemical free energy calculation. The chemical free energy is written as

$$g_{chem} = \frac{1}{\Omega_0}\left[\left(1 - h\left(\eta\right)\right) G_{mix}^{0,\alpha}\left(X,T\right) + h\left(\eta\right) G_{mix}^{0,\delta}\left(X,T\right) + wk\left(\eta\right)\right], \tag{3.2.8}$$

where $G_{mix}^{0,\alpha}\left(X,T\right)$ is the molar free energy of mixing of α-zirconium with hydrogen, $G_{mix}^{0,\delta}\left(X,T\right)$ is the molar free energy for δ-hydride, and $\Omega_0 = 1.4 \times 10^{-5}$ m^3/mol is the molar volume of α-zirconium. The microstructural evolution of the system is governed by Eqs. 3.2.3 and 3.2.5.

The interface energy is calculated as described in Chapter II. To summarize, the interfacial energy is estimated according to

$$\gamma = \gamma_{ch} + \gamma_{st}, \tag{3.2.9}$$

where γ_{ch} is the chemical energy of the interface and γ_{st} is the energy due to the presence of dislocations reducing the misfit strain between the α and δ phases. In this chapter, $\gamma_{ch} = 35$ mJ/m^2 is chosen, which was calculated in Ref. [150] for other coherent zirconium hydride phases. The dislocation contribution to the interfacial energy is modeled as

$$\gamma_{st} \approx \frac{1}{2} Sb \cdot \left(1 - \psi\right) \epsilon^0 \tag{3.2.10}$$

as described in Chapter II. To represent an intermediate state with respect to the fully coherent interface and the fully relaxed interface, $\lambda = 0.5$ is chosen such that $\gamma_{st} \approx 280\,\mathrm{mJ/m^2}$ and $\gamma = 305\,\mathrm{mJ/m^2}$. For $w = 0$, $\kappa_X = 0$, and this interface energy, $\kappa_n = 4 \times 10^{-10}\,\mathrm{J/m}$ was found numerically, resulting in a diffuse interface width of 1 nm when measured between $0.1 < \eta < 0.9$.

The mobility of hydrogen in the system was calculated according to the formulation in Chapter II. For the α-zirconium/δ-hydride phase field model, the mobility in the α phase is given as

$$M^{\alpha}\left(X,T\right) = \frac{D^{\alpha}\left(T\right)}{\partial^2 \tilde{G}^{0,\alpha}_{mix}/\partial X^2} \tag{3.2.11}$$

and the mobility in the δ phase is given as

$$M^{\delta}\left(X,T\right) = \frac{D^{\delta}\left(T\right)}{\partial^2 \tilde{G}^{0,\delta}_{mix}/\partial X^2} \tag{3.2.12}$$

such that the total mobility in Eq. 3.2.3 is

$$M\left(X,\eta,T\right) = \left(1 - h\left(\eta\right)\right) M^{\alpha}\left(X,T\right) + h\left(\eta\right) M^{\delta}\left(X,T\right), \tag{3.2.13}$$

where $D^{\alpha}\left(T\right)$ is the diffusivity of hydrogen in α-zirconium [131] and $D^{\delta}\left(T\right)$ is the diffusivity of hydrogen in δ-hydride [132].

The governing equations are nondimensionalized in this work, which improves numerical behavior by ensuring all quantities are within approximately an order of unity. The nondimensionalization method was presented in Chapter II.

CALPHAD free energy approximations

The CALPHAD free energies of mixing for α-zirconium and δ-hydride were parameterized by Dupin et al. [98] and are discussed in Chapter II. For illustrative purposes, they are reproduced here. The molar free energy of mixing for hydrogen in α-zirconium is given as

$$\begin{aligned} G_{mix}^{0,\alpha}(X,T) &= \left[(1-2X)\, G_{Zr}^{0,hcp}(T) + X G_{ZrH}^{0,hcp}(T)\right] \\ &\quad + RT\left[X\ln\left(\frac{X}{1-X}\right) + (1-2X)\ln\left(\frac{1-2X}{1-X}\right)\right] \end{aligned} \tag{3.2.14}$$

and that for δ-hydride is given as

$$\begin{aligned} G_{mix}^{0,\delta}(X,T) &= \frac{1}{2}\left[(2-3X)\, G_{Zr}^{0,fcc}(T) + X G_{ZrH_2}^{0,fcc}(T)\right] \\ &\quad + RT\left[X\ln\left(\frac{X}{2(1-X)}\right) + (2-3X)\ln\left(\frac{2-3X}{2(1-X)}\right)\right] \\ &\quad + \left(\frac{3X^2-2X}{4(X-1)^2}\right)\left[(X-1)\, L_{fcc}^{0}(T) + (1-2X)\, L_{fcc}^{1}(T)\right] \end{aligned} \tag{3.2.15}$$

where R is the gas constant [98].

The free energy $G_{mix}^{0,\alpha}$ is defined over the composition range of $X = (0, 0.5)$, and $G_{mix}^{0,\delta}$ is defined over $X = \left(0, \frac{2}{3}\right)$, while the equilibrium atomic fraction of hydrogen in the δ-hydride phase is approximately $X = 0.6$. The phase field formulation for the chemical free energy density necessitates calculation of energies outside the composition range of $G_{mix}^{0,\alpha}$ when the system is in the δ-hydride phase. Equations 2.2.4 and 2.2.5 are approximated using Eq. 3.2.7 to obtain $\tilde{G}_{mix}^{0,\alpha}(X,T)$ and $\tilde{G}_{mix}^{0,\delta}(X,T)$, which are substituted

for $G_{mix}^{0,\alpha}(X,T)$ and $G_{mix}^{0,\delta}(X,T)$ in Eq. 3.2.8. Following the method in Section 2.2.1, four X_{bound} compositions were chosen as $X_{low}^{\alpha} = 0.001$, $X_{high}^{\alpha} = 0.499$, $X_{low}^{\delta} = 0.5$, and $X_{high}^{\delta} = 0.665$. Figure 3.2.2 shows the surface of the chemical free energy density (Eq. 3.2.8) that results from using the approximated $\tilde{G}_{mix}^{0,\alpha}$ and $\tilde{G}_{mix}^{0,\delta}$; the surface is continuous and differentiable everywhere.

The mobility must be a positive quantity. Given that diffusion coefficients are measured in a single phase and are thus always positive, the phase field formulation requires a positive second derivative of the free energy (thermodynamic factor) to obtain a positive, non-divergent hydrogen mobility (Eq. 2.2.18). The value for X_{low}^{δ} was chosen because the sign of the second derivative of $G_{mix}^{\delta,0}(X,T)$ changes at $X \approx 0.48$. For $X \geq 0.5$, the second derivative of $G_{mix}^{\delta,0}(X,T)$ is positive; by choosing $X_{low}^{\delta} = 0.5$, $\tilde{G}_{mix}^{\delta,0}(X,T)$ exhibits a positive second derivative for all X and all T within 485 K to 750 K.

Simulation conditions

To verify the approximation method, several planar interface simulations were run to equilibrium, i.e., uniform chemical potential, and the phase fractions and compositions were compared to the values obtained from the common tangent construction of $G_{mix}^{0,\alpha}(X,T)$ and $G_{mix}^{0,\delta}(X,T)$. A planar interface was chosen to eliminate the Gibbs-Thomson effect, which shifts equilibrium phase compositions due to the presence of a curved interface. No-flux boundary conditions were applied for X and η, and isothermal conditions with $T = 485$, 550, 600, 650, and 750 K were chosen. The lowest temperature, 485 K, was chosen because X_{low}^{α} is approximately equal to the composition of the α-zirconium phase boundary at that temperature and thus represents the lower limit for the applicability of the approximation. The highest temperature, 750 K, is close to the β-zirconium

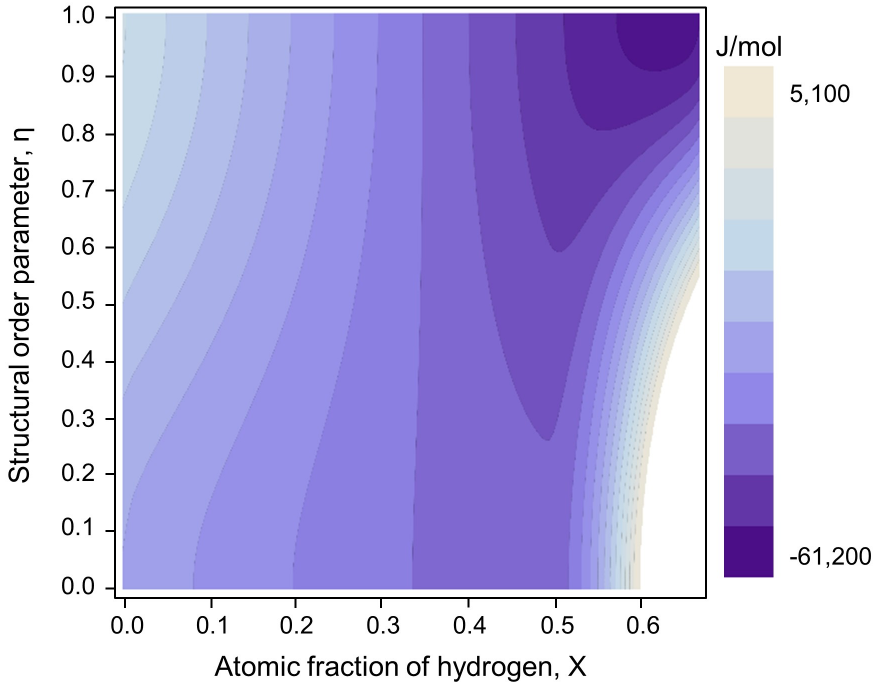

Figure 3.2.2: A contour plot of the free energy surface $f_{chem}\left(X, \eta, T\right)$ at 600 K formed by applying the approximation method to $G_{mix}^{0,\alpha}$ and $G_{mix}^{0,\delta}$.

eutectoid, and the intermediate temperature, 600 K, is a typical operating temperature for fuel cladding in a light water reactor. The initial condition for each simulation was a narrow planar hydride in the center of a zirconium domain (Fig. 3.2.3), with the overall hydrogen atomic fraction fixed at either X_H^{total} =0.03 or 0.10 (340 or 1230 wt ppm). These compositions are representative of a typical hydrogen content in fuel cladding toward the end of its service lifetime and a high hydrogen content that might occur during accident conditions, respectively. Two-dimensional simulations, rather than 1D, were performed for convenience (see below), with a domain size of 480 nm $\times$ 120 nm.

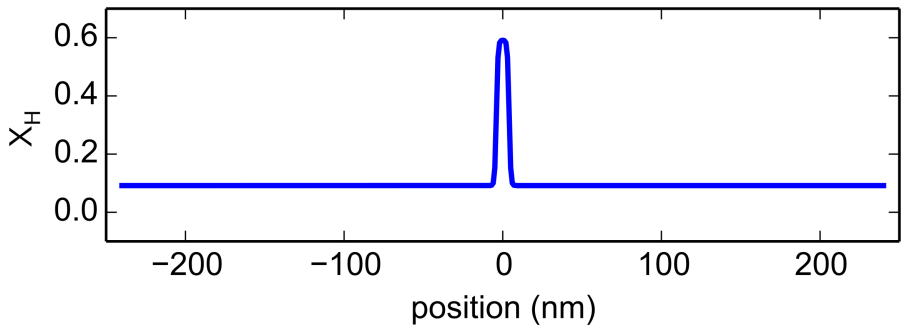

(a)

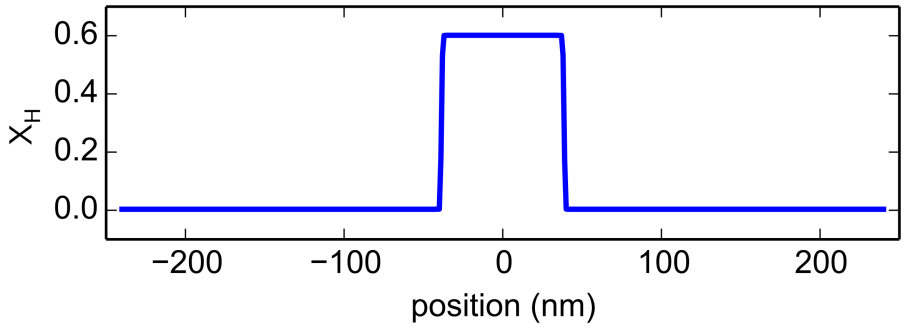

(b)

Figure 3.2.3: Line cuts of the (a) initial and (b) final hydrogen atomic fraction fields for the 2D planar hydride simulation at 550 K and an overall hydrogen composition of $X_H = 0.1$. In both cases, the hydride is in the center and has a composition $X_H^\delta \approx 0.6$. In (a), the atomic fraction of hydrogen in α-zirconium is $X = 0.0917$, while in (b) it is 3.54×10^{-3}.

The simulations were performed with Hyrax, which is described in Chapter II. Two-dimensional simulations were performed because microstructural evolution simulations will need to be performed in at least 2D, and the runtime of 2D simulations was short enough such that there was no explicit need for 1D simulations. Square, four-node quadrilateral elements were used for the mesh and linear Lagrange shape functions were used for η, X, and $\delta G/\delta X$. Adaptive meshing was employed to resolve the interface

without incurring unnecessary computational expense, with a maximum element side length of 2.4 (in nondimensionalized units, equivalent to 2.4 nm) and a minimum element side length of 0.30, corresponding to a maximum of three levels of refinement. The BDF2 time integration scheme [196] was applied with an initial nondimensionalized time step size of 1×10^{-4} (equivalent to 0.5613 s). The adaptive time-stepping scheme allowed a maximum of 10% increase per time step with a maximum time step size of 0.10. This percent increase was chosen to reduce the amount of time required to achieve equilibrium conditions; for simulations of microstructural evolution, less aggressive time adaptivity should be applied. The simulations, which were performed in parallel, used a single matrix preconditioner and the Additive Schwarz Method preconditioning process.

3.3 Results and discussion

In this section, the equilibrium phase fractions and compositions from the simulations were compared to values obtained from $G^{0,\alpha}_{mix}$ and $G^{0,\delta}_{mix}$ via a common tangent construction, denoted with PF and CP, respectively. An example of the initial and final conditions of the planar interface simulations is shown in Fig. 3.2.3 for $X_H^{total} = 0.10$ at 550 K. An initial hydride plate is present in a supersaturated zirconium matrix; at equilibrium it has grown to its final phase fraction (ϕ^δ) and the matrix and hydride phases have achieved their final compositions (X_H^α and X_H^δ, respectively). The ϕ^δ values were found for the phase field simulation by thresholding at $\eta = 0.5$ and numerically integrating to find the area of the resulting spatial region.

Table 3.3 shows the comparisons between the simulation results and the values obtained from the common tangent construction for the phase fractions and phase compositions. In addition, Table 3.4 shows the difference and percent error for ϕ^δ, X_H^δ, and X_H^α at

each temperature and X_H^{total}. Overall, the results indicate that there is excellent agreement between the calculated and simulated values of ϕ^{δ}, X_H^{δ}, and X_H^{α} over the range of 485 K - 750 K. The difference in $\phi^{\delta,PF}$ and $\phi^{\delta,CP}$ values for all simulations is less than or equal to 0.001; this small difference may be due to the thresholding procedure used in calculating ϕ^{δ}. The X_H^{δ} values are identical within three significant figures except for two cases, for which the error is less than 0.2%. The most error occurs in X_H^{α}, although it is still very low. The error in X_H^{α} is at most 5.6% at 485 K and is between 1-2% at 550, 600, and 650 K. For the $X_H^{\alpha,PF}$ and $X_H^{\alpha,CP}$ values that differ, the difference is on the order of 1×10^{-4}, and the differences generally increase slightly with increasing temperature. The error in X_H^{α} is greater than the error in X_H^{δ}, which is due to the shape of $G_{mix}^{0,\alpha}$ and $G_{mix}^{0,\delta}$. Because the curvature of the energy well of $G_{mix}^{0,\delta}$ is much greater than that of $G_{mix}^{0,\alpha}$, small changes in $G_{mix}^{0,\alpha}$ will have a greater effect on the equilibrium phase compositions than small changes in $G_{mix}^{0,\delta}$.

Table 3.3: Theoretical and simulated equilibrium phase characteristics of the α-zirconium/δ-hydride system.

Temperature (K)	X_H^{total}	$X_H^{\alpha,CP}$	$X_H^{\alpha,PF}$	$X_H^{\delta,CP}$	$X_H^{\delta,PF}$	$\phi^{\delta,CP}$	$\phi^{\delta,PF}$
485	0.03	1.07×10^{-3}	1.07×10^{-3}	0.605	0.605	0.0479	0.0483
	0.10		1.12×10^{-3}		0.605	0.164	0.164
550	0.03	3.49×10^{-3}	3.49×10^{-3}	0.601	0.601	0.0443	0.0447
	0.10		3.54×10^{-3}		0.601	0.162	0.163
600	0.03	7.22×10^{-3}	7.15×10^{-3}	0.599	0.598	0.0385	0.0392
	0.1		7.36×10^{-3}		0.599	0.157	0.158
650	0.03	1.32×10^{-2}	1.31×10^{-2}	0.595	0.595	0.0289	0.030
	0.10		1.32×10^{-2}		0.595	0.149	0.150
750	0.03	3.00×10^{-2}	3.00×10^{-2}	-	-	0.00	0.00
	0.10	3.38×10^{-2}	3.38×10^{-2}	0.587	0.587	0.120	0.120

X_H: overall atomic fraction of hydrogen, X_H^{α}: atomic fraction of hydrogen in α-zirconium, X_H^{δ}: atomic fraction of hydrogen in δ-hydride, ϕ^{δ}: area fraction of δ-hydride, ''CP'': calculated from $G_{mix}^{0,\alpha}$ and $G_{mix}^{0,\delta}$ using the common tangent construction, ''PF'': simulated using phase field method.

Table 3.4: Difference and percent error between theoretical and simulated equilibrium phase characteristics of the α-zirconium/δ-hydride system.

Temperature (K)	X_H^{total}	ΔX_H^{α}	error (%)	ΔX_H^{δ}	error (%)	$\Delta\phi^{\delta}$	error (%)
485	0.03	0.0	0.0	0.0	0.0	0.0004	0.8
	0.10	6.0×10^{-5}	5.6	0.0	0.0	0.001	0.6
550	0.03	0.0	0.0	0.0	0.0	0.0004	0.9
	0.10	5.0×10^{-5}	1.4	0.001	0.17	0.001	0.6
600	0.03	-7.0×10^{-5}	1.0	-0.001	0.17	0.0007	1.8
	0.1	1.4×10^{-4}	1.8	0.0	0.0	0.001	0.6
650	0.03	-1.0×10^{-4}	0.8	0.0	0.0	0.0011	3.8
	0.10	0.0	0.0	0.0	0.0	0.001	0.7
750	0.03	0.0	0.0	-	-	0.0	0.0
	0.10	0.0	0.0	0.0	0.0	0.0	0.0

$\Delta X_H^{\alpha} = X_H^{\alpha,PF} - X_H^{\alpha,CP}$; $\Delta X_H^{\delta} = X_H^{\delta,PF} - X_H^{\delta,CP}$; $\Delta\phi^{\delta} = \phi^{\delta,PF} - \phi^{\delta,CP}$.

We now examine the impact of X_{bound} values on the simulated X_H^{α}, X_H^{δ}, and ϕ^{δ} values. To this end, two additional sets of simulations are performed to explore the effect of X_{bound} values. The original set of simulations, detailed above, is labeled Set A and has $X_{low}^{\alpha} = 0.001$, $X_{high}^{\alpha} = 0.499$, $X_{low}^{\delta} = 0.5$, and $X_{high}^{\delta} = 0.665$. Set B improves the approximation by decreasing the lower α subdomain boundary composition to $X_{low}^{\alpha} = 1 \times 10^{-6}$ while keeping X_{high}^{α}, X_{low}^{δ}, and X_{high}^{δ} the same as in Set A. Finally, Set C tests the sensitivity of the results on the choice of X_{bound} values. The X_{bound} values of Set A were changed by 5% to reduce the ranges over which $G_{mix}^{0,\alpha}$ and $G_{mix}^{0,\alpha}$ remain un-approximated. Specifically, $X_{low}^{\alpha} = 1.05 \times 10^{-3}$, $X_{high}^{\alpha} = 0.474$, $X_{low}^{\delta} = 0.525$, and $X_{high}^{\delta} = 0.632$ are used.

The percent errors in $X_H^{\alpha,PF}$ and $\phi^{\delta,PF}$ for the three sets with respect to $X_H^{\alpha,CP}$ and $X_H^{\delta,CP}$ are shown in Fig. 3.3.1 as well as the root-mean-square (RMS) of the error over the

temperature range examined. The results for $X_H^{\delta,PF}$ are not shown because they show no variation within three significant figures except for Set C, $X_H^{total} = 0.03$, $T = 600$ K, for which $X_H^{\delta,PF} = 0.599$. The data sets A and B are identical within three significant figures except for one value, ϕ^{δ} at 600 K for $X_H^{total} = 0.03$, indicating that the larger value of X_{low}^{α}=0.001 versus 1×10^{-6} does not affect the result. Conversely, the results of Set A and Set C differ. Most notably, the simulations at 485 K did not converge to equilibrium, as discussed further below. However, no obvious trends in error are evident when comparing the results of sets A and C. For some quantities, the RMS of the error is greater for Set A versus Set C, while for others, it is less; the maximum RMS error is less than 3%.

The two simulations for Set C at 485 K failed to reach equilibrium. The ϕ^{δ} values for both simulations attained 99% of $\phi^{\delta,CP}$, but the solver was unable to reduce the residual further. Because the simulations at higher temperatures did not experience this issue, it appears that the choice of X_{low}^{α} is the cause. While $X_{low}^{\alpha} = 1.05 \times 10^{-3}$ is less than $X_H^{\alpha,CP} = 1.07 \times 10^{-3}$, the function approximation may occur at a value too close to $X_H^{\alpha,CP}$. The curvature of the approximated function $G_{low}^{\alpha,Taylor}$ is less than the original function $G_{mix}^{0,\alpha}$, which may interfere with the ability of the numerical solver to determine the solution near equilibrium. To avoid this issue, we suggest that X_{low}^{α} be chosen around 90% of $X_H^{\alpha,CP}$. A similar consideration is likely necessary for X_{high}^{δ}. In general, we recommend conducting planar interface simulations to quantify the error in a given system when applying the proposed approximation method.

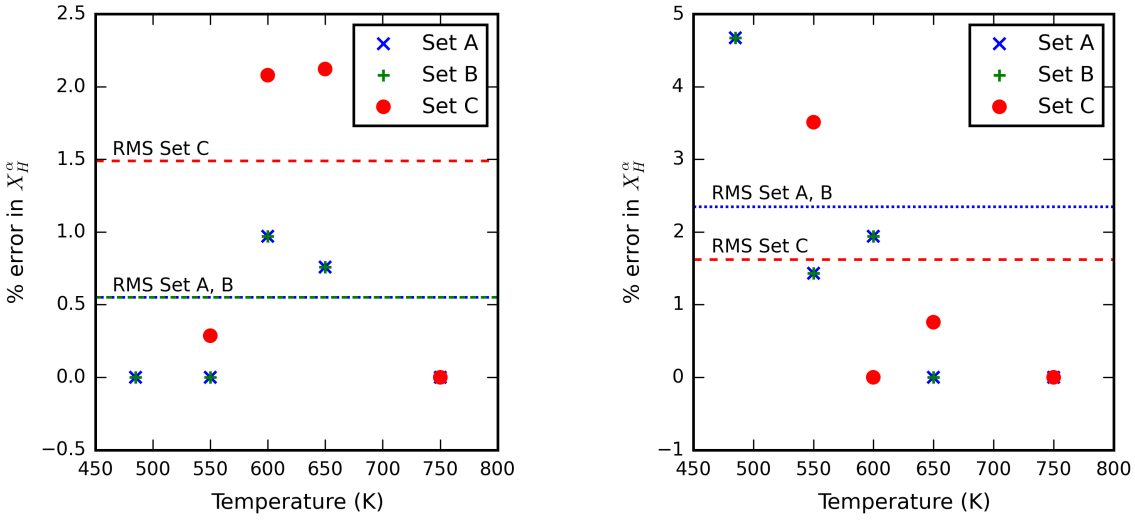

(a)

(b)

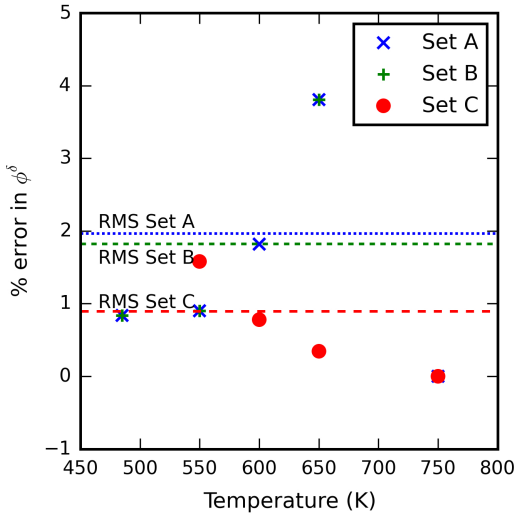

(c)

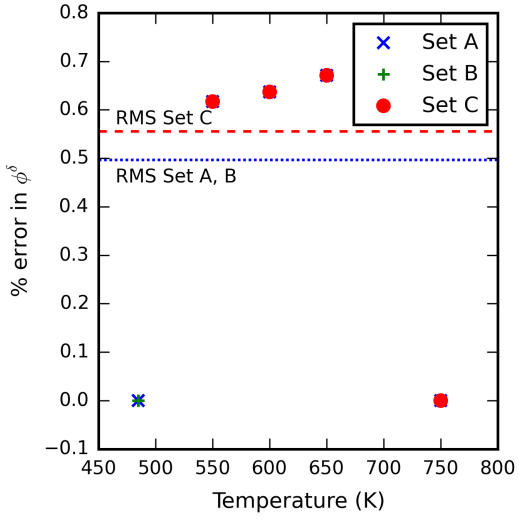

(d)

Figure 3.3.1: The percent error in $X_H^{\alpha,PF}$ and $\phi^{\delta,PF}$ versus $X_H^{\alpha,CP}$ and $\phi^{\delta,CP}$ for three sets of simulations with different X_{bound} values. The root-mean-square value of the error over the temperature range is indicated by the dashed lines. The parameter values for each set are given in the text. Subfigures (a) and (c) illustrate the percent error in X_H^α and ϕ^δ for $X_H^{total} = 0.03$, respectively. Subfigures (b) and (d) illustrate the percent error in X_H^α and ϕ^δ for $X_H^{total} = 0.10$, respectively.

The proposed approximation method is advantageous over other techniques of incorporating CALPHAD-based free energy expressions into phase field simulations because it is both simple to implement and addresses the issues in using these free energies. One alternative method, linking the phase field software directly to a thermodynamic database [105,190,191], requires an interface to database software, potentially costly software licensing, and additional computational expense to query the database at each mesh point and each time step. Another alternative method, polynomial approximation of the free energy expressions [113,192--195,197], requires more effort than the proposed method. For example, one must make choices among many options, e.g., various fitting and error weighting schemes, when performing a polynomial fit. In contrast, the proposed approximation method allows the free energy expression to be directly incorporated into the phase field software with negligible error and little effort. While the implementation was performed for a finite element framework, the method may be used with other numerical methods such as the finite difference method.

Figure 3.3.2 illustrates how the approximation method handles the extreme case of a negative atomic fraction value. Two δ-hydride precipitates were seeded into an α-zirconium matrix with a composition of $X = 0.015$ at 485 K, and $X^{\alpha}_{low} = 1 \times 10^{-6}$ (Fig. 3.3.2a). Both hydride precipitates induce a depletion zone around themselves as they grow. During the first several time steps, in which the system rapidly adjusts from the initial conditions, the atomic fraction of hydrogen between the two hydrides becomes slightly negative (Fig. 3.3.2b). This transient is resolved when longer-range diffusion supplies additional solute, and physical behavior is quickly reestablished (Fig. 3.3.2c). The approximation method results in a free energy that is well behaved even when the evolution equations of the phase field model temporarily drive the system toward

unphysical values. In this scenario, it is acceptable to allow small, transient values of negative concentration because the driving force and kinetics of the system tends to correct them. On the other hand, if we were to simply use the CALPHAD free energy, the code will yield undefined values.

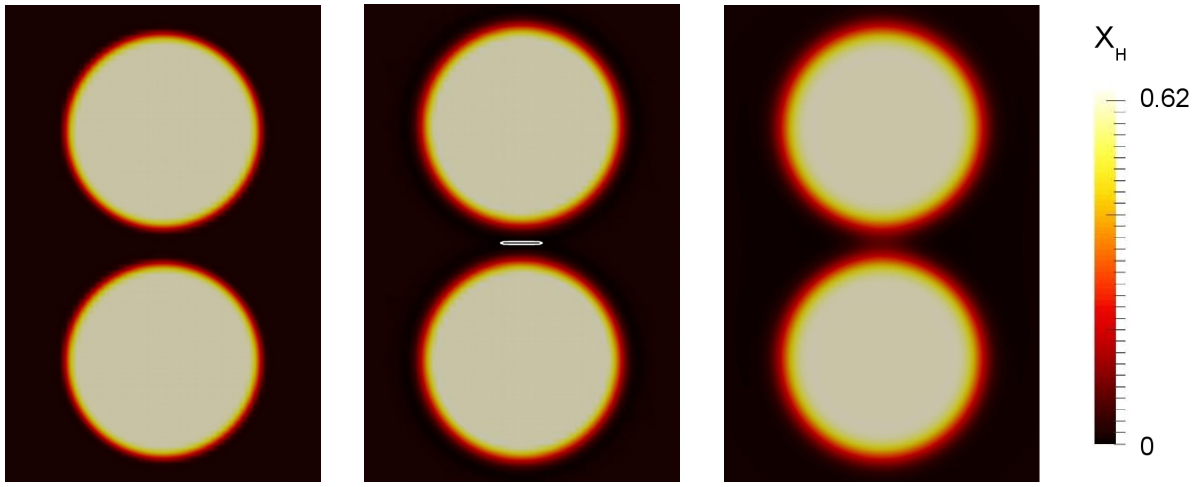

Figure 3.3.2: An example of precipitate growth and hydrogen depletion. (a) The initial condition, in which two δ-hydride precipitates were seeded into an α-zirconium matrix with a composition of $X = 0.015$ at 485 K. (b) After two time steps, depletion regions have started to form around both precipitates. The white contour line indicates a small region between the precipitates in which the hydrogen atomic fraction has become slightly negative. (c) After thirty time steps, longer-range diffusion has supplied additional solute, and the hydrogen atomic fraction has increased such that the solute value is positive everywhere.

3.4 Conclusions

The proposed free energy approximation method is a simple and efficient technique to overcome the numerical challenges encountered during phase field simulations that incorporate CALPHAD-based free energies of mixing. The free energies are transformed

into piecewise functions composed of three subfunctions that are defined on subdomains of solute composition. Low and high subdomain boundary compositions are chosen within the composition domain over which each free energy is defined. The subdomain boundary compositions are chosen to be sufficiently outside the composition range expected to be encountered in the simulation. These values may be chosen to avoid unwanted behavior in the free energy or its derivatives, such as an undefined energy at a composition that will be evaluated within the phase field model, or a free energy curvature that will yield a negative mobility. At each boundary composition, the free energy is approximated as a second-order Taylor expansion of the free energy around the boundary composition. The free energy between the low and high subdomain boundary compositions retains the original form, while outside this region, the Taylor expansions are substituted. The resulting free energy is second-order differentiable over the entire range of structural order parameter and composition values encountered within the simulation.

A phase field model for the α-zirconium/δ-hydride system was employed to demonstrate the free energy approximation method. Planar interface simulations were performed to verify the approximation method over a range of temperatures. The compositions of the α and δ phases as well as the δ phase fraction obtained from the phase field simulations were compared to the values calculated from the common tangent construction of the original CALPHAD free energies. The results indicate that the approximation method does not appreciably affect the equilibrium compositions and phase fractions of the α-zirconium/δ-hydride system. In addition, the error in the compositions of the α and δ phases as well as the δ phase fraction obtained from the phase field simulations were examined. We found that for the α-zirconium/δ-hydride system, X_{low}^{α} should be approximately 10% less than equilibrium composition of the α phase to ensure that simulations can run to equilibrium.

We also found that while the simulation results do change slightly with a 5% variation in X_{bound} values, the RMS of the error is less than 3% for all quantities examined as long as the aforementioned condition on X_{low}^{α} is met.

The approximation method presented here is general and can be straightforwardly applied to other materials systems. It is particularly useful for CALPHAD free energies developed using sublattice models, because these energies may not be defined over the entire range of compositions that would be encountered in the phase field model. As the free energies of many substitutional and interstitial solutions are modeled using sublattice models, this method will increase the applicability of phase field models to a wide range of alloy systems. In addition, the method reduces the stiffness of the equations at the composition domain boundaries, which may improve numerical behavior. However, in the WBM formulation, the diffuse interface width that results from using physically appropriate interface energies can be constrained to several nanometers due to the presence of an inherent energy barrier in the free energy. This interface width increases the computational cost, making large-scale simulations prohibitively expensive. Thus, the KKS phase field model formulation may be better suited for incorporating CALPHAD-based free energies so that the interfacial thickness may be readily adjusted.

CHAPTER IV

A Nucleation Algorithm for the Coupled Conserved-Nonconserved Phase Field Model

In this chapter, a refinement to the existing nucleation algorithm for a coupled conserved-nonconserved phase field model is presented. In the new method, which offers greater ease of implementation as compared to the existing approach, only the nonconserved order parameter is modified to seed supercritical nuclei (thus termed order-parameter-only seeding). The order-parameter-only seeding method naturally satisfies the conservation law for the conserved order parameter. In addition, the implementation within Hyrax is described. The evolution of a single nucleus is examined to ensure that the precipitate growth kinetics are not affected by the seeding method. After a brief initial transient period, order-parameter-only nucleation yields similar precipitate growth characteristics to that of the existing model. The kinetics of a phase transformation exhibiting concurrent nucleation and growth is analyzed in the form of the Avrami equation, and a statistical analysis is performed to determine if mesh and/or time adaptivity affects the simulation results. The statistical analysis indicates that the nucleation algorithm is amenable to

adaptive meshing and adaptive time stepping.

4.1 Methods

4.1.1 Phase field model

The proposed OPO seeding method relies on the coupling between a conserved order parameter and a nonconserved order parameter through the free energy. Although OPO seeding can be implemented into any coupled conserved-nonconserved phase field model, a model describing the zirconium/zirconium hydride system [63] is adopted to demonstrate the approach. The zirconium/zirconium hydride system is described using a conserved field variable, c, that represents the concentration of hydrogen, and a nonconserved structural order parameter, η, that distinguishes the different structures of the two phases, where $\eta = 0$ for zirconium and $\eta = 1.5$ for the hydride. To demonstrate the nucleation algorithm, the free energy functional from Ref. [63] is simplified by neglecting elastic energy and by retaining only one structural order parameter corresponding to one of the three equivalent orientation variants. The free energy is given as

$$G = \int_V \left\{ g_{chem}\left(c, \eta\right) + \frac{\kappa_c}{2}|\nabla c|^2 + \frac{\kappa_\eta}{2}|\nabla \eta|^2 \right\} dV, \tag{4.1.1}$$

where κ_c is the gradient energy coefficient for concentration, κ_η is the gradient energy coefficient for the structural order parameter, g_{chem} is the bulk chemical free energy density, and V is the volume. The expression for g_{chem} used in this work is

$$g_{chem}(c,\eta) = \frac{A_1}{2}(c-c_1)^2 + \frac{A_2}{2}(c-c_2)\eta^2 - \frac{A_3}{4}\eta^4 + \frac{A_4}{6}\eta^6, \tag{4.1.2}$$

where c_1, c_2, $A_i\,(i=1,...,4)$ are constants. The values of c_1 and c_2 are the equilibrium concentrations of hydrogen in the matrix and hydride, respectively, while the A_i's control the shape of the free energy surface [63].

The microstructural evolution of the system is governed by coupled conserved-nonconserved dynamics. The Cahn-Hilliard equation [81] governs the evolution of the concentration of hydrogen as

$$\frac{\partial c}{\partial t} = \nabla \cdot [M \nabla \mu], \tag{4.1.3}$$

where the chemical potential, μ, is

$$\mu = \frac{\partial f_{chem}}{\partial c} - \kappa_c \nabla^2 c, \tag{4.1.4}$$

t is the time, and M is the mobility of hydrogen.In addition, the Allen-Cahn equation [94] governs the evolution of the nonconserved structural order parameter as

$$\frac{\partial \eta}{\partial t} = -L\left[\frac{\partial f_{chem}}{\partial \eta} - \kappa_\eta \nabla^2 \eta\right], \tag{4.1.5}$$

where L is the kinetic coefficient. Both the mobility and the kinetic coefficient are assumed to be isotropic. Following Ref. [63], we use $L = M = 0.4$, $A_1 = 18.5$, $A_2 = -8.5$, $A_3 = 11.5$, $A_4 = 4.5$, $\kappa_c = \kappa_\eta = 1.5$, $c_1 = 0.006$, and $c_2 = 0.59$ in nondimensionalized units. Nondimensionalization of the governing equations is found in the Appendix.

4.1.2 Explicit nucleation algorithm

Simmons et al. pioneered the development of an algorithm that explicitly introduces nuclei in a phase field simulation based on classical nucleation theory [155]. Hereafter, this method will be referred to as the explicit nucleation algorithm. The concepts from that algorithm that are incorporated into our model are discussed in Chapter II and are summarized in this section. The local nucleation rate for critical nuclei, $J_C(\mathbf{r}, t)$, is calculated following classical nucleation theory [96] as [155]

$$J_C(\mathbf{r}, t) = Zn\Delta v\beta^* \exp\left(\frac{-\Delta G^*}{k_B T}\right) \exp\left(\frac{-\tau}{t}\right), \tag{4.1.6}$$

where $N = n\Delta v$, n is the number density of atoms and Δv is the volume of the element. Following Ref. [155], Eq. 4.1.6 is simplified to

$$J_C(\mathbf{r}, t) = k_1 \exp\left(\frac{-k_2}{\Delta c}\right), \tag{4.1.7}$$

where k_1 and k_2 are adjustable parameters that control the nucleation rate and Δc is the supersaturation. The local nucleation probability, $P(\mathbf{r}, t)$, is calculated as [155]

$$P(\mathbf{r}, t) = 1 - \exp\left(-J_C \Delta t\right), \tag{4.1.8}$$

where Δt is the time interval over which the nucleation probability is calculated.

In the explicit nucleation algorithm, the nucleation step is executed after each phase field time step [155], and J_C and P are calculated for each volume element in the simulation. It is assumed that nucleation rates are low enough for the given mesh that only one nucleus may form in any volume element [155]. After P is computed, the positions of new nuclei

are determined. This is accomplished by performing a binary test on the local nucleation probability: a random number, $R(t)$ between $[0,1]$ is generated, and if $R(t) < P(\mathbf{r},t)$, a nucleus is introduced at that position [160].

4.1.3 Order-parameter-only nucleation algorithm and implementation details

The implementation flow chart of the nucleation algorithm within Hyrax is shown in Fig. 4.1.1. After each phase field step, the nucleation step is executed. Within the nucleation step, ΔG_C, J_C, and P are calculated for each element (for the specific example in this work, Δc is calculated during ΔG^* step). If the element contains a second-phase particle or is within the interface, the probability is set to zero; we set $P = 0$ for $\eta > 0.1$, although a different threshold value could be taken. After P is computed, the positions of new nuclei are determined. In a similar manner as Ref. [160], a pseudorandom number, $R(\mathbf{r},t)$, is generated with a uniform distribution between $[0,1]$ for each element. If $R(\mathbf{r},t) < P(\mathbf{r},t)$, a nucleus is introduced at that position. In the rare event that nucleation occurs in two adjacent elements, the two nuclei will merge into one precipitate. When a nucleation event occurs in a particular mesh element, the centroid of that element is chosen as the center point of the nucleus. The position of the nucleus and the time of its formation are stored in a list, which is accessed by the mesh adaptivity and nucleus introduction functions. If mesh adaptivity is enabled, the finite element mesh is refined as necessary so that the mesh has appropriate local resolution for the subsequent introduction of each nucleus. Nuclei are seeded accordingly by direct modification of the nodal solution vector of the structural order parameter. If time adaptivity is used, the time step is reduced upon a

nucleation event to a specified time step size. After the modification of the structural order parameter, the system is allowed to evolve according to Eqs. 4.1.3 and 4.1.5.

To use the explicit nucleation algorithm with a nonuniform mesh, we define a volumetric nucleation rate, $J_{C,V}$. In this work, $J_{C,V}$ is based on Eq. 4.1.7 and is formulated as

$$J_{C,V}\left(\mathbf{r},t\right)=\tilde{k}_1\cdot\exp\left(\frac{-k_2}{\Delta c}\right), \tag{4.1.9}$$

where $\tilde{k}_1=k_1/\Delta v$. Thus, the nucleation probability for an element is given by

$$P\left(\mathbf{r},t\right)=1-\exp\left(-J_{C,V}\Delta v\Delta t\right). \tag{4.1.10}$$

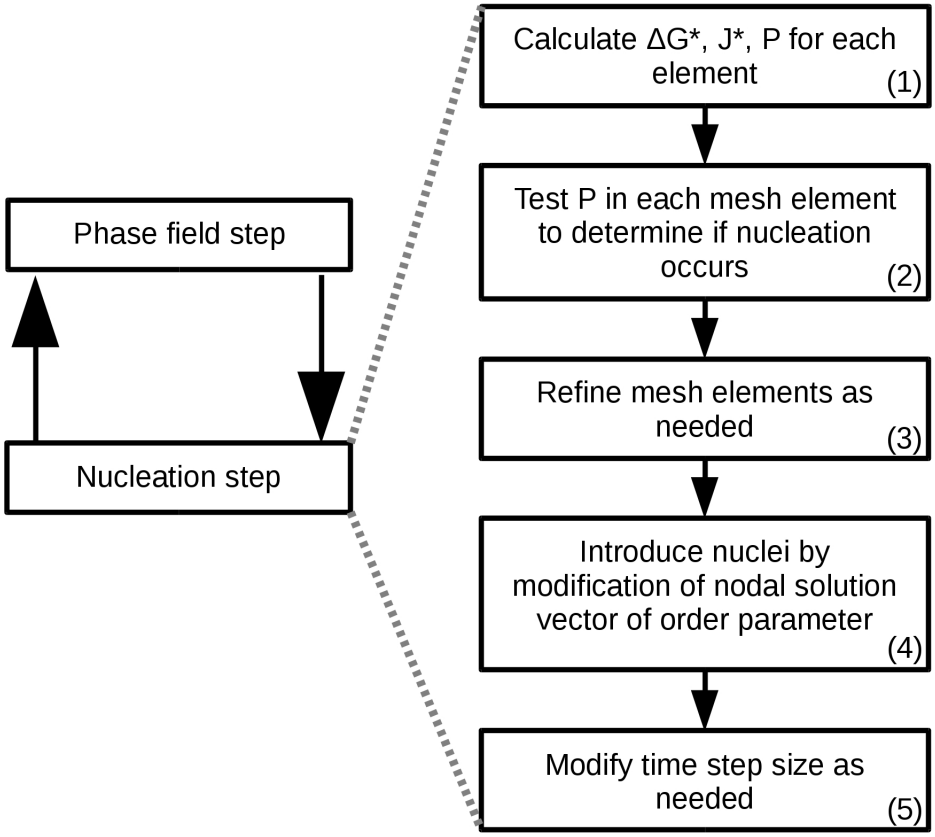

Figure 4.1.1: A flow chart of the order-parameter-only nucleation algorithm implemented within Hyrax. After a phase field time step, the nucleation algorithm is executed. (1) The nucleation activation energy, nucleation rate, and nucleation probability are calculated for each element. (2) The nucleation probability in each element is tested to determine if nucleation occurs. If mesh adaptivity is enabled, (3) mesh elements are refined as needed to obtain sufficient resolution for new nuclei. (4) The nodal solution vector for the order parameter is explicitly modified to reflect the formation of the new nuclei. (5) The time step size is modified as needed. Upon the completion of the nucleation step, the next phase field time step is executed.

The nucleus seeding method described in this work differs significantly from that described in Refs. [155,160]. Unlike that method, the concentration field is left unchanged, and thus mass conservation is naturally met. OPO nucleus seeding is more computationally efficient and significantly easier to implement because it eliminates the need

to calculate mass conservation requirements before nucleus introduction. Figure 4.1.2 illustrates how the concentration and structural order parameter are altered in the OPO seeding method for initially uniform fields. Upon determination of a new nucleus position, an OPO nucleus is introduced by altering the value of the structural order parameter to reflect the presence of the second phase (Fig. 4.1.2a). The OPO nucleus introduced into the simulation domain must be larger than the critical nucleus size for the given solute concentration. Each nucleus has a finite size and encompasses multiple elements such that the interface is well-resolved. Although we choose a circular nucleus with a diffuse interface profile, alternative nucleus shapes such as those described in Refs. [166--168] could be incorporated. The modification of the order parameter field may either be carried out for only one time step (when a new nucleus is seeded), or be held fixed for several time steps; both cases are studied in this work.

For comparison purposes, we use the nucleus seeding method in Ref. [155] as the initial condition for a single-particle simulation by altering both the concentration and the structural order-parameter (hereafter referred to as ''order parameter and concentration'' or OPC seeding). The treatment of the structural order parameters is the same for both OPO seeding and OPC seeding (Fig. 4.1.2a). However, the solute concentration is increased in the nucleus and depleted in the surrounding region for OPC seeding (Fig. 4.1.2c). The total quantity of solute in the computational domain is the same for OPO and OPC seeding. In this work, the depletion region width and concentration is determined in a fashion similar to Ref. [155], but we choose to minimize the width of the depletion region, w_d, by setting the concentration in the depletion region, c_d, close to zero due to the low initial solute concentration. The amount of solute that must be compensated for by the reduced concentration in the depletion region, Δs, is calculated from the initial concentration, the

system volume, and the nucleus volume and composition. We then estimate w_d as the width that is needed to compensate for Δs assuming $c_d = 0$. For simplicity, we round w_d up to the nearest integer, and adjust c_d such that the amount of solute is identical in both the OPO and OPC simulations

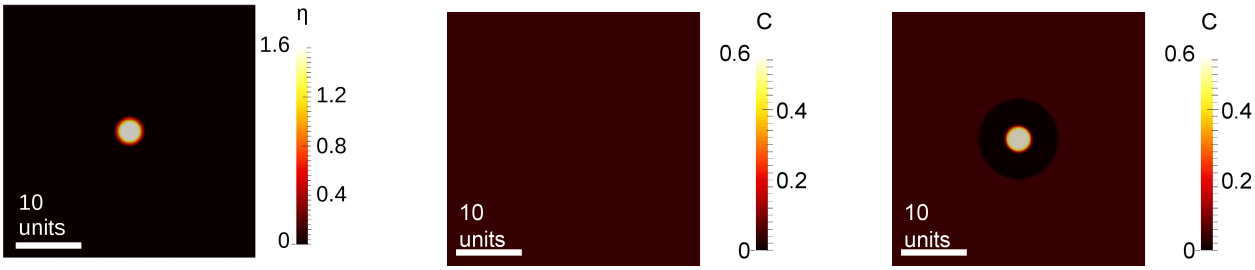

(a) (b) (c)

Figure 4.1.2: The profiles of the concentration and structural order parameter upon nucleus seeding. (a) The structural order parameter for both an OPO seed and an OPC seed. (b) The concentration for an OPO seed, which is uniform. (c) The concentration for an OPC seed, which is non-uniform.

4.1.4 Simulation conditions

In this work, simulations are performed in two dimensions. No-flux boundary conditions are applied for the concentration and structural order parameters, and the initial hydrogen concentration is set to $c = 0.0562$, which is less than the concentration used in Ref. [63] but high enough to induce concurrent nucleation and growth. The equilibrium interface width is 1.33 in nondimensionalized units measured between $0.1\eta_p < \eta < 0.9\eta_p$, where η_p is the value of η in the hydride. Introduced nuclei have a radius of $r = 1.8$, which is twice the minimum stable particle size at this composition so that nuclei will grow even if introduced into regions with decreased supersaturation. The diffuse interface width of the nuclei is 0.9

and the profile is specified by a sine function, though a different profile and width could be chosen. The BDF2 implicit time integration scheme [196]) is employed. The nonlinear relative convergence tolerance is 10^{-8}. The simulations use a single matrix preconditioner and the Additive Schwarz Method preconditioning process. For simulations with a fixed time step size, a nondimensionalized time step size of $\Delta t = 0.01$ is used. For simulations with time adaptivity, computational efficiency is optimized by employing a variable time step size based on the ratio of the time step size to the CPU time required to iteratively solve the system of equations for each time step [198]. A maximum of 1% increase per time step is allowed, and the maximum $\Delta t = 1.0$ is chosen. Upon a nucleation event, the time step is reduced to $\Delta t = 0.01$. The mesh is composed of square, four-node quadrilateral elements and linear Lagrange shape functions are used for the structural order parameter, concentration, and chemical potential variables. Simulations without mesh adaptivity are performed with an element side length of 0.32. Simulations with adaptive meshing have a maximum element side length of 5.12 and a minimum element side length of 0.32, corresponding to a maximum of four levels of refinement. Adaptive mesh refinement involves splitting and refining elements based on an error indicator. We use the gradient jump indicators [69,183] for c and η, which computes the change in the gradient from one element to the next. The mesh is refined for any element within 75% of the maximum jump, and the mesh is coarsened for any element within 5% of the minimum jump, where the maximum and minimum are taken over the entire mesh. These refinement parameters are chosen to ensure that introduced nuclei are appropriately resolved.

Single-particle simulations are performed with a nondimensionalized domain size of 38.4×38.4 to study the evolution of OPO and OPC nuclei. The field of the structural order parameter initially contains one seed in the center of the computational domain. The

OPC nucleus has a concentration of $c = 0.59$, the depletion region has a concentration of $c_d = 3.13 \times 10^{-4}$ and a depletion width of $w_d = 8$, and the matrix outside the depletion region has a concentration of $c = 0.0562$. No mesh or time adaptivity are used for the single-particle simulations.

The equilibrium phase fraction for the given concentration is needed for the Avrami analysis. The equilibrium phase fraction is found by allowing a planar interface simulation with a domain size of 76.8×9.6 to achieve equilibrium, where equilibrium is defined as uniform chemical potential within convergence tolerance. The initial condition for the simulation is an OPO hydride plate at the left edge of the computational domain and a uniform concentration of $c = 0.0562$. No mesh adaptivity is used, but time adaptivity is employed to attain equilibrium efficiently.

The Avrami analysis simulations are performed with a nondimensionalized domain size of 460.8×460.8. The values $\tilde{k}_1 = 2.5 \times 10^{-4}$ and $k_2 = 4.71 \times 10^{-2}$ are chosen to induce concurrent nucleation and growth conditions with a constant nucleation rate. The value of k_2 controls the nucleation rate by affecting the driving force for nucleation, while the value of $\tilde{k}_1$ controls the number of nuclei formed during the early stage of the simulation [155]. Finally, the structural order parameter initially contains one randomly located nucleus. This initial condition is chosen based on numerical considerations; by introducing a nucleus, the residual of the initial condition is large enough such that the relative-tolerance convergence criterion is met.

The parameters for the phase field model used in the nucleation algorithm verification are given in nondimensionalized units. The non-dimensionalization of the model is given as follows. Ref. [63] indicates that the free energy functional was fit to the Zr-H phase diagram at 523 K. A nondimensionalized quantity q in the phase field model has a

corresponding dimensional quantity $\hat{q}$. Characteristic scale values for the system's length, energy, and time are defined, and the equations are nondimensionalized using these values. The characteristic length scale was set to $\hat{l} = 1 \times 10^{-9}$ m so that nucleation may be simulated. The characteristic volumetric energy scale was chosen as $|\Delta\hat{g}| = 1 \times 10^{8}$ J/m^3, on the order of volumetric energy of mixing for the Zr-H system [98]. The volumetric energy can be converted to a molar energy as $|\Delta\hat{g}_m| = \Delta f \cdot \Omega_0 = 1.40 \times 10^{3}$ J/mol, where the atomic volume of zirconium is $\Omega_0 = 1.4 \times 10^{-5}$ m^3/mol. While no experimental information exists for the Allen-Cahn kinetic coefficient, $L = 1\,\mathrm{J}^{-1}\mathrm{s}^{-1}$ was chosen to maintain a diffusion-controlled transformation [113]. Therefore, the characteristic time is $t_0 = 2.86 \times 10^{-4}$ s. The relationships between the dimensional and dimensionless quantities are presented in Table 4.5.

Table 4.5: Nondimensionalization expressions for quantities within the phase field model.

Quantity	Nondimensionalization expression
Time	$t = \hat{t} \cdot \hat{L} \cdot \lvert\Delta\hat{g}_m\rvert$
Length	$r = \hat{r}/\hat{l}$
Hydrogen mobility	$M = \hat{M} \cdot \hat{t}_0 \cdot \hat{l} \cdot \lvert\Delta\hat{g}\rvert$
Allen-Cahn kinetic coefficient	$L = \hat{L} \cdot \lvert\Delta\hat{g}_m\rvert \cdot \hat{t}_0$
Gradient coefficient	$\kappa = \hat{\kappa}/\left(\lvert\Delta\hat{g}\rvert \cdot \hat{l}^2\right)$
Chemical energy	$g_{chem} = \hat{g}_{chem}/\lvert\Delta\hat{g}\rvert$

4.2 Results and discussion

4.2.1 OPO nucleus evolution

To assess the OPO nucleus seeding method, the evolution of an OPO nucleus is compared to that of an OPC nucleus. The values of the concentration and structural order parameter at the center of the nucleus, denoted as c_{p0} and η_{p0}, respectively, are used to quantify the evolution of an OPO nucleus. Figure 4.2.1 shows c_{p0} and its derivative with respect to time, which indicate how solute accumulates in the precipitate during nucleus formation. Initially c_{p0} increases rapidly; this behavior is hereafter termed the ''solute accumulation'' (SA) stage. As c_{p0} approaches the equilibrium concentration, solute accumulation slows, with $\partial c_{p0}/\partial t$ decreasing below 1.0 at $t = 0.16$, which we hereafter refer to as t_c. During the SA stage, a solute depletion region with a smooth gradient profile is naturally formed around the nucleus. Note that the equilibrium value of c_{p0} is not yet attained during the time examined, but the plot range is selected to focus on the early transient behavior that occurs immediately following nucleus introduction. In addition, η_{p0} and its time derivative are plotted in Fig. 4.2.2. The value of η_{p0} decreases during the SA stage and exhibits a minimum at $t = 0.08$, hereafter referred to as t_{min}, but subsequently increases rapidly, with $\partial \eta_{p0}/\partial t$ attaining a maximum at $t = 0.15$. The value of η in the precipitate is slightly higher than its equilibrium value during the time examined, but the value decreases as the fraction of the precipitate phase evolves toward its equilibrium value. This behavior of η in the precipitate is a result of the shape of the free energy well shown in Fig. 4.2.3, and will in general depend on the details of the specific free energy function.

The behavior of c_{p0} and η_{p0} can be elucidated by examining the free energy of the

introduced seed. Figure 4.2.3 is a contour plot of f_{chem} with the (c_{p0}, η_{p0}) path indicated by the red squares. The OPO nucleus has a much higher free energy density than either the matrix or precipitate phases as it is initialized (the leftmost square). As such, there is a large driving force to diffuse solute into the nucleus. Once the presence of additional solute has lowered the free energy of the nucleus, further energy reduction occurs by the increase of η_{p0} toward its equilibrium value.

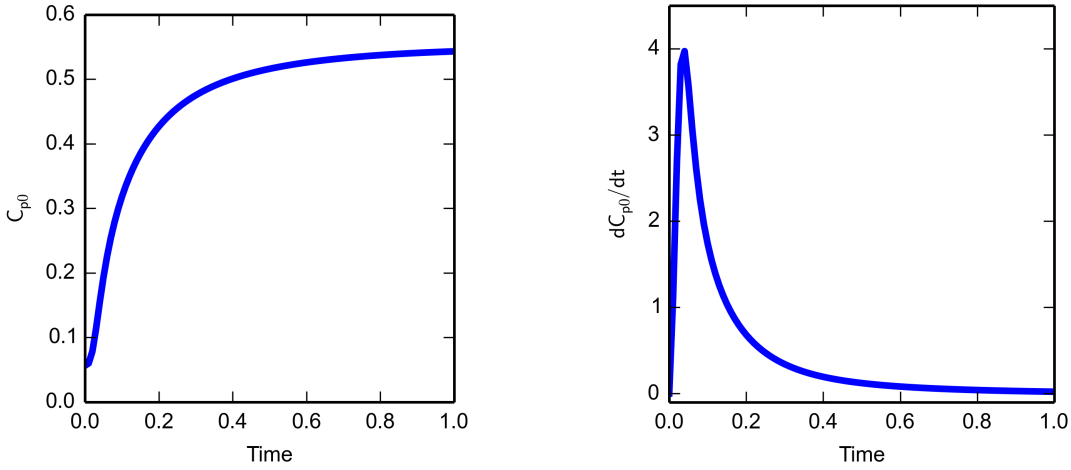

(a) (b)

Figure 4.2.1: (a) The value of the concentration at the center of the nucleus for OPO seeding without order parameter holding. (b) The rate of change of the concentration value at the center point with respect to time.

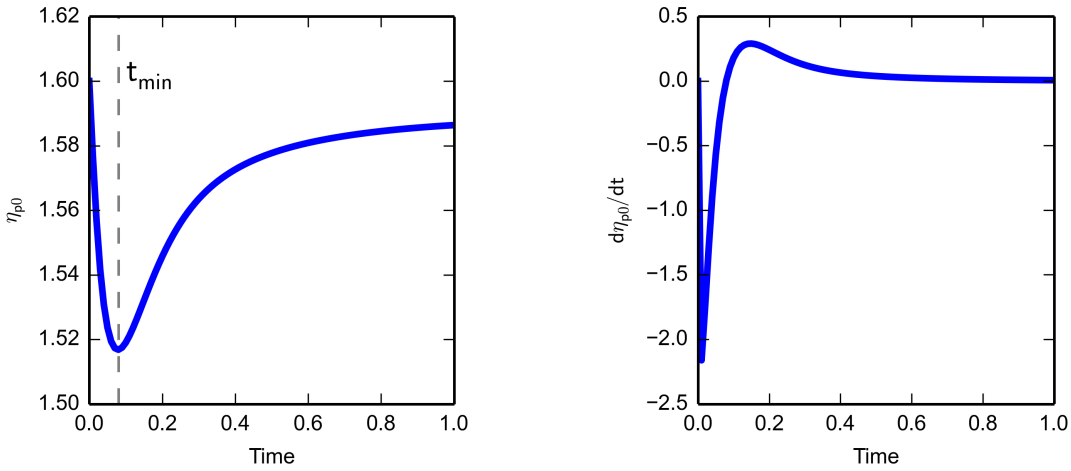

(a) (b)

Figure 4.2.2: (a) The value of the structural order parameter at the center of the nucleus for OPO seeding without order parameter holding. (b) The rate of change of the value of the structural order parameter at the center point with respect to time.

While OPO seeding naturally generates a nucleus with a surrounding depletion region, the initial SA stage will delay the precipitate growth versus an OPC nucleus, which seeds both concentration and order parameter fields. We first examine the (c_{p0}, η_{p0}) path of an OPC nucleus, shown by the orange triangles in Fig. 4.2.3. Although the OPC nucleus is near the energetic minimum, its c_{p0} and η_{p0} values evolve slightly following the introduction of the seed. Figure 4.2.4a shows the precipitate area fractions of an OPO and an OPC nucleus. The area is found by thresholding the structural order parameter at $\eta = 1.5$ and summing the area of each element within the thresholded region. The area of the OPO nucleus is smaller than the area of the OPC nucleus at any given time over the time simulated. The maximum difference in area is 9% at $t = 1.8$ and the difference decreases slowly after that to 4% at $t = 10$. Growth of the OPO nucleus may be delayed both due to the time needed to accumulate solute and due to the initial decrease in the structural order parameter,

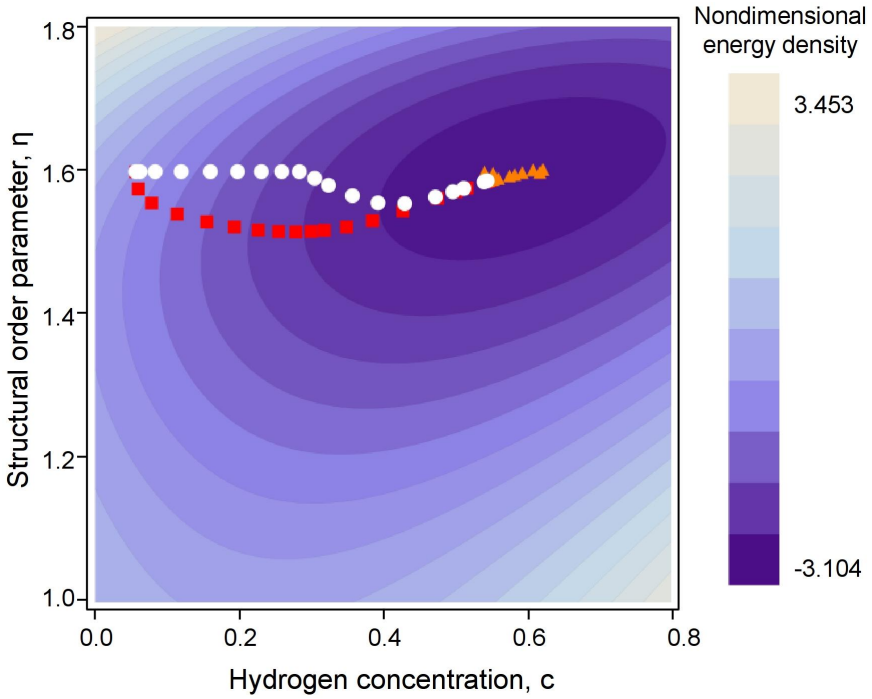

Figure 4.2.3: The contour plot of f_{chem} and the (c_{p0}, η_{p0}) paths for the different nucleus seeds. The red squares are for the OPO nucleus and the white circles are for the OPO+hold nucleus; in both cases the energy of the as-seeded nucleus is indicated by the leftmost point. The orange triangles are for the OPC nucleus.

which lowers the driving force for solute accumulation.

To maintain the driving force and to prevent nucleus dissolution, the structural order parameter may be held fixed during the SA stage (termed an ''OPO+hold'' seed). The hold time, t_{hold}, can be found by examining the evolution of c_{p0}, η_{p0}, and the area fraction of the OPO seed. The area fractions of an OPO+hold nucleus and an OPC nucleus are compared for a given t_{hold}, and the t_{hold} value that yields the smallest maximum difference in area fractions is chosen. The characteristic times t_c and t_{min} provide a guideline for choosing t_{hold}. Figure 4.2.4a shows the area fraction of an OPO+hold nucleus with $t_{hold} = t_{min}$. The maximum difference in the area fraction for the OPO+hold nucleus versus the OPC nucleus is approximately 4% at $t = 2.8$ and the difference decreases slowly after that to

1.6% at $t = 10$. The difference is significantly less than the difference between the OPO nucleus and the OPC nucleus. For the cases examined, the area fraction of the OPO+hold nucleus is insensitive to t_{hold} values between t_{min} and t_c, and we believe this finding is likely general. This insensitivity is beneficial when using time adaptivity in simulations. A comparison of η_{p0} for the OPO nucleus and the OPO+hold nucleus is shown in Fig. 4.2.4b; the undershoot of η_{p0} is much less in the OPO+hold case. In addition, the (c_{p0}, η_{p0}) path for the OPO+hold nucleus is shown in Fig. 4.2.3 by the white circles. During the time that the structural order parameter is held fixed, the (c_{p0}, η_{p0}) path remains where the driving force for solute accumulation is larger than that followed by the OPO nucleus, accelerating the stabilization of the OPO+hold nucleus.

The value of t_{min} varies depending on the simulation setup, and thus the value chosen for t_{hold} should be adjusted accordingly. However, the hold time should not be longer than necessary because it may delay growth by preventing the interface from propagating even under growth conditions. The value of t_{min} may vary depending on the solute mobility and the kinetic coefficient of the structural order parameter, the driving force of the transformation, the local solute concentration, and the size of the seeded nucleus. For example, a lower solute concentration will likely require a longer hold time to accumulate solute.

The size of the introduced nucleus will vary depending upon the model system and the simulation parameters, and thus needs to be adjusted accordingly. The nucleus size can be determined based on the results of single-particle simulations for each system. The introduced nucleus should be as small as possible without dissolving. The critical nucleus size, which is typically on the order of a nanometer, presents a lower bound on the nucleus size and may be determined by classical nucleation theory. However, the

size of the introduced nucleus is also affected by the maximum mesh resolution of the simulation and the diffuse interface width, which are numerical parameters. The size of the introduced nucleus should be larger than the diffuse interface width to ensure a bulk region exists. It is likely that the introduced nucleus will be larger than the critical nucleus size, unless the mesh resolution is extremely high. If the introduced nuclei are much larger than the critical size and the time to grow to that size is significant, a time correction will be necessary. In this work, r is sufficiently small that this correction is unnecessary. We also note that a larger r will require a larger t_{hold} for a given system, and thus these parameters need to be consistently determined.

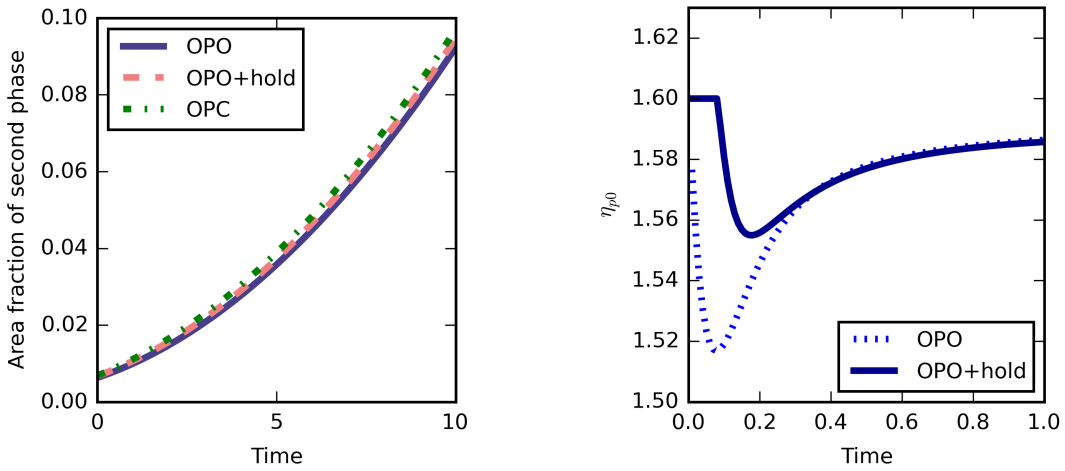

(a) (b)

Figure 4.2.4: (a) The area fraction of the second-phase particle using OPO, OPO+hold, and OPC methods. (b) The value of the structural order parameter at the center of an OPO nucleus and at the center of an OPO+hold nucleus with $t_{hold} = t_{min} = 0.08$.

4.2.2 Validation of OPO nucleation and growth

The early-stage kinetics of precipitation and growth simulated with the OPO nucleation algorithm are analyzed by fitting the simulation results to the Avrami equation [199--201]. For these simulations, we do not use time or mesh adaptivity; these simulations have the highest numerical resolution and accuracy considered in this work. Nine simulations, denoted with the subscript ''0,'' are performed with different seeds for random number generation to obtain statistical information. We use a hold time of $t_{hold} = 1.25t_{min} = 0.1$.

First, the number of precipitates and the area fraction of the transformed phase are examined. Figure 4.2.5a presents the snapshots of one of the nine simulations performed, showing the distribution of precipitates with varying size as a result of concurrent nucleation and growth. For the set of simulations, approximately 30 nuclei form by $t = 2$. By $t = 20$, nucleation is almost complete, and approximately 200 nuclei have formed.

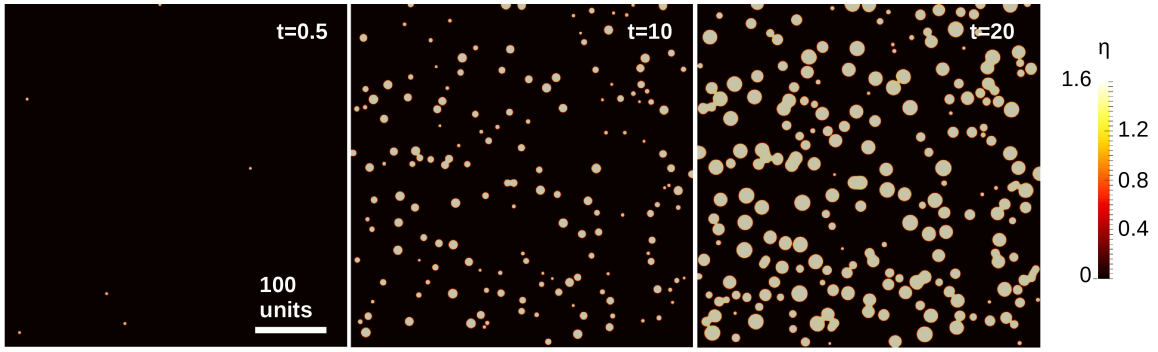

(a)

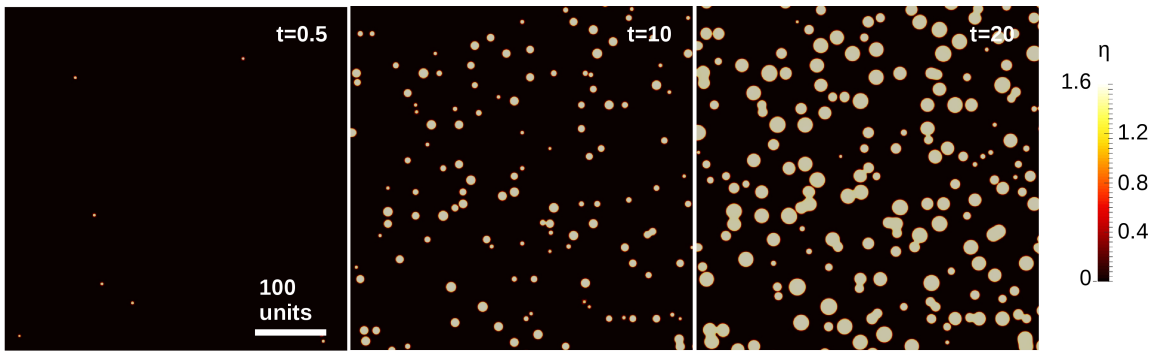

(b)

Figure 4.2.5: The structural order parameter showing concurrent nucleation and growth (CNG) conditions (a) with no mesh or time adaptivity used for the simulation and (b) with mesh and time adaptivity used.

The area fraction of the transformed phase, $A\,(t)$, for the fastest and slowest transformations are shown in Fig. 4.2.6a. The area fraction varies by 20% at $t = 20$ between the slowest and fastest transformations. This variation is due to the stochastic nature of the nucleation algorithm, which causes the exact location and timing of the nucleation events to be different for each simulation.

To confirm that the OPO+hold algorithm and implementation reproduce the results expected from classical nucleation theory, we consider the Avrami equation

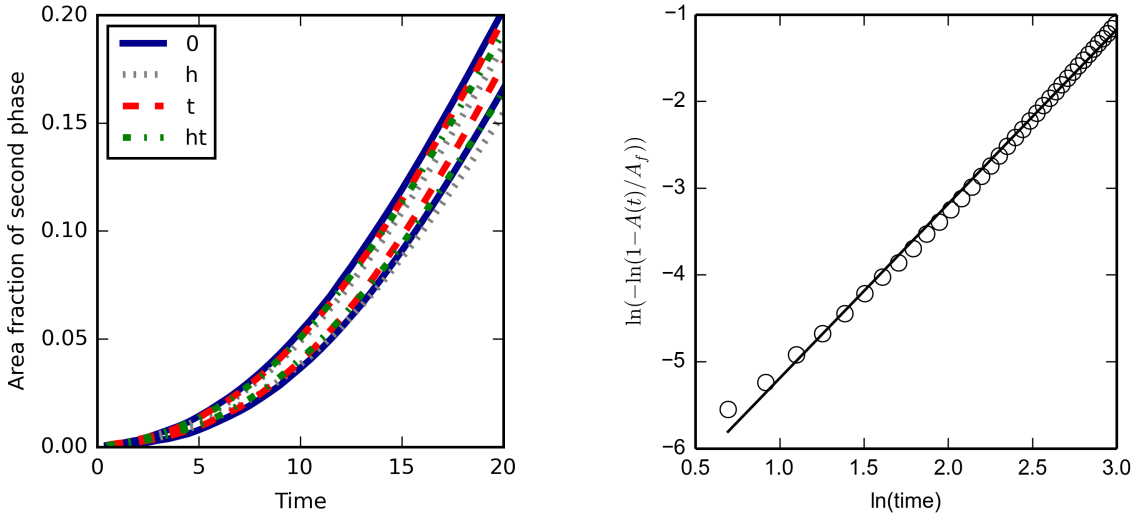

(a) (b)

Figure 4.2.6: (a) The area fraction of the transformed phase is plotted for the fastest and slowest cases within each set of simulations performed with with no adaptivity (solid, 0), with mesh adaptivity (gray dots, h), with time adaptivity (red dash, t), and both mesh and time adaptivity (green dash-dot, ht). (b) An example of an Avrami fit for the area fraction of the transformed phase (the data is indicated by the circles and the fit is the solid line).

$$A\left(t\right)/A_f = 1 - \exp\left(-Kt^m\right) \tag{4.2.1}$$

where t is time, A_f is the equilibrium area fraction, m is the Avrami coefficient, which indicates the type of transformation kinetics, and K is the time constant. To perform the Avrami analysis, Eq. 4.2.1 is rewritten as

$$\ln\left[-\ln\left(1 - A\left(t\right)/A_f\right)\right] = \ln K + m\ln\left(t\right). \tag{4.2.2}$$

The value of $A\left(t\right)/A_f$ is inserted into the left-hand side of Eq. 4.2.2, and the resulting values are fit to the right-hand side of Eq. 4.2.2, such that m and K are determined from

the slope and the intercept of the line, respectively. An example is given in Fig. 4.2.6b. Although there is some deviation of the data from the single linear fit, the fit provides simple a quantitative metric of the phase transformation kinetics and the effects of mesh and/or time adaptivity on it. Because the slope varies over the time period examined, the value obtained from the linear fit is an average of the slope over that time period. The time constant K is found by calculating the value of the linear fit when $\ln(t) = 0$. In this work, m and K are calculated using $A(t)$ between $2 \leq t \leq 20$, while nucleation and growth are ongoing. As we mentioned previously, for a given initial condition, the stochastic nature of the nucleation algorithm will generate a range of transformation kinetics. This variation is quantified by the Avrami coefficient and time constant averaged over the nine simulations, $\bar{m}$ and $\bar{K}$, respectively, and their standard deviations, σ_m and σ_K. For the validation simulations, we find the values $\bar{m}_0 = 2.01$, $\sigma_{m,0} = 0.0370$, $\bar{K}_0 = 7.44 \times 10^{-4}$, and $\sigma_{K,0} = 1.18 \times 10^{-4}$. These Avrami coefficients are in agreement with the value resulting from a simplified analysis of an early-stage diffusional transformation with a constant nucleation rate [199,202], when taking the dimensionality of the simulations into account.

Table 4.6: Average kinetic coefficients and their standard deviations for the concurrent nucleation and growth simulations. Listed are the average Avrami coefficient and its standard deviation, $\bar{m}$ and σ_m, respectively, and the average time constant and its standard deviation, $\bar{K}$ and σ_K, respectively.

Adaptivity type	$\bar{m}$	σ_m	$\bar{K}$	σ_K
no adaptivity	2.01	0.0370	7.44×10^{-4}	1.18×10^{-4}
mesh adaptivity	2.02	0.0719	6.53×10^{-4}	1.59×10^{-4}
time adaptivity	1.98	0.0499	8.15×10^{-4}	1.45×10^{-4}
mesh and time adaptivity	1.97	0.0479	7.79×10^{-4}	1.28×10^{-4}

The OPO nucleation algorithm allows for a broad range of nucleation conditions to

be modeled. By varying $\tilde{k}_1$ and k_2 in Eq. 4.1.9, more nuclei may be formed earlier in the simulation, resulting in $m < 2$ in two dimensions. Site saturation conditions, in which all nuclei are present at the start of the phase transformation, result in $m = 1$ in two dimensions. Simmons et al. reported difficulty in lowering the Avrami coefficient much below 1.67 due to numerical instabilities from the composition profiles of the nucleus and depletion region [155]. The OPO nucleation seeding method gives no such instability because it does not introduce sharp concentration gradients. By increasing $\tilde{k}_1$ by one order of magnitude, m decreases to 1.25. Further increasing $\tilde{k}_1$ should result in site saturation, indicating the flexibility of this algorithm at modeling different nucleation behavior.

4.2.3 Effect of adaptivity on concurrent nucleation and growth simulations

Large-scale three-dimensional phase field simulations of concurrent nucleation and growth are computationally intensive. To improve computational efficiency, time and mesh adaptivity may be used to reduce resolution while retaining sufficient accuracy. The time adaptivity scheme ensures a small time step during nucleation events but allows it to grow in the absence of nucleation. Mesh adaptivity reduces the degrees of freedom by using larger mesh elements in regions with lower field gradients; an example of the mesh adaptivity within the simulation is shown in Fig. 4.2.7. However, the effect of the reduced resolution must be evaluated, and sufficient mesh and time resolution must be retained within the simulation. For example, if a mesh is overly coarse with respect to the characteristic length scale of the microstructure, the spatial distribution of precipitates may be affected. If the time step is too large for the nucleation rate, the assumption that only one

nucleus may form per element may be violated, affecting the number of nuclei introduced into the simulation. While mathematical analyses to determine the upper limit of temporal and spatial discretization steps for nucleation and growth are beyond the scope of this work, we present a method to quantify the effect of adaptivity on the simulation results. We perform simulations with mesh adaptivity, time adaptivity, and combined mesh and time adaptivity, denoted with the subscripts ‘‘h,’’ ‘‘t,’’ and ‘‘ht,’’ respectively. As before, nine simulations are performed for each case to capture the statistical behavior.

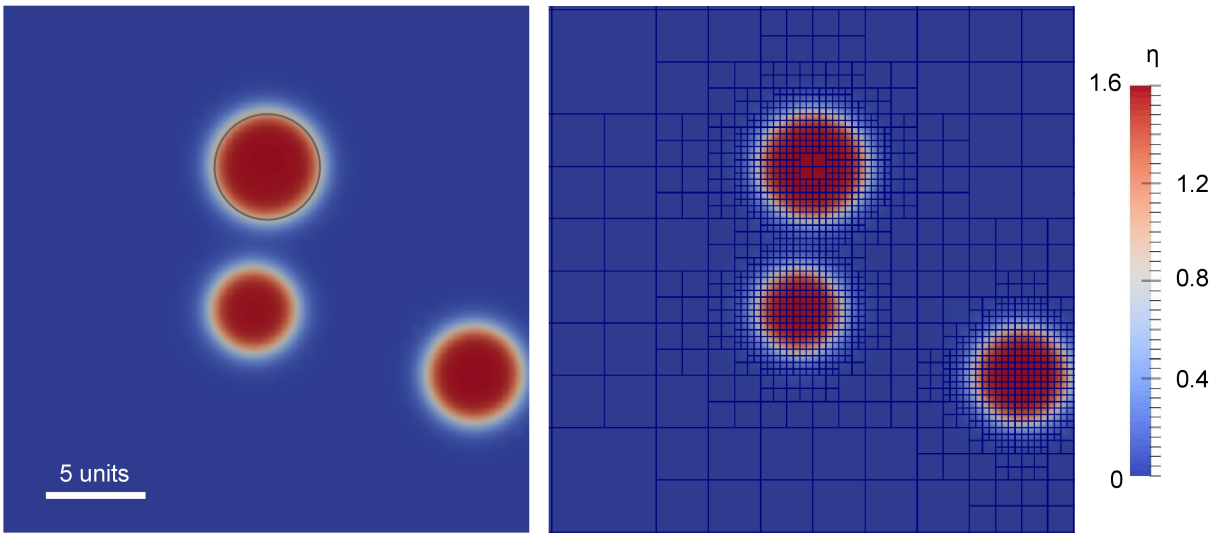

Figure 4.2.7: A magnified snapshot of a concurrent nucleation and growth simulation performed with mesh adaptivity. Left: Three precipitates are shown. A perfect circle has been imposed over the topmost precipitate (dashed gray line) as a guide for the eye. Right: The same snapshot, but with the mesh shown in blue, which contains both the largest and smallest mesh elements. The mesh is finest at the precipitate interfaces.

Following the discussion in Section 4.2.2, we examine the microstructure and the transformation kinetics simulated when using adaptivity. Figure 4.2.5b shows the snapshots of a concurrent nucleation and growth simulation performed with both mesh and time adaptivity; the initial condition is identical to that in Fig. 4.2.5a. The microstructure is

similar to the previous case presented in Fig. 4.2.5a, although for this specific simulation, there are fewer precipitates at $t = 20$. To examine the kinetics, the area fraction of the transformed phase is shown in Figure 4.2.6 for the fastest and slowest cases for each set of simulations. The area fractions for simulations with different adaptivities are similar to those of the simulations with no adaptivity. Therefore, for the given adaptivity parameters, time or mesh adaptivity do not appear to affect the simulated kinetics.

Following the discussion in Section 4.2.2, we examine the microstructure and the transformation kinetics simulated when using adaptivity. Figure 4.2.5b shows the snapshots of a concurrent nucleation and growth simulation performed with both mesh and time adaptivity; the initial condition is identical to that in Fig. 4.2.5a. The microstructure is similar to the previous case presented in Fig. 4.2.5a, although for this specific simulation, there are fewer precipitates at $t = 20$. To examine the kinetics, the area fraction of the transformed phase is shown in Figure 4.2.6 for the fastest and slowest cases for each set of simulations. The area fractions for simulations with different adaptivities are similar to those of the simulations with no adaptivity. Therefore, for the given adaptivity parameters, time or mesh adaptivity do not appear to affect the simulated kinetics.

We perform the Avrami analysis described in Section 4.2.2 to quantify the transformation kinetics obtained from simulations that utilize adaptivity, and means and standard deviations are shown in Fig. 4.2.8. As presented in Table 4.6, the values of $\bar{m}_t$, $\bar{m}_h$, and $\bar{m}_{ht}$ are equal to $\bar{m}_0$ within two significant figures, and $\sigma_m/\bar{m}$ values are in the range of 0.018 to 0.036, indicating a narrow distribution. Mesh adaptivity results in the largest σ_m ($\sigma_{m,h} \approx 1.9\sigma_{m,0}$), while time adaptivity and combined time and mesh adaptivity result in similar σ_m ($\sigma_{m,t} \approx \sigma_{m,ht} \approx 1.3\sigma_{m,0}$). These results indicate that the power-law exponent in Eq. 4.2.1 is insensitive to both the stochastic nature of nucleation and to adaptivity.

In contrast, the time constant K exhibits more variation from simulation to simulation within each set. The values of $\bar{K}_h$ and $\bar{K}_t$ differ from $\bar{K}_0$ by more than 10%, with the largest differences in K occurring when using mesh adaptivity. These values also exhibit larger scatter, as evidenced by $\sigma_K / \bar{K}$ in the range of 0.16 to 0.24. This greater variation indicates that K is sensitive to the details of when and where nucleation events occur. Overall, the case with no adaptivity results in the smallest values of σ_m and σ_K, showing that adaptivity tends to increase the variation in the simulated kinetics. However, the overlap in the error bars between the data sets indicates that no systematic differences are evident for differences in the average m and K values.

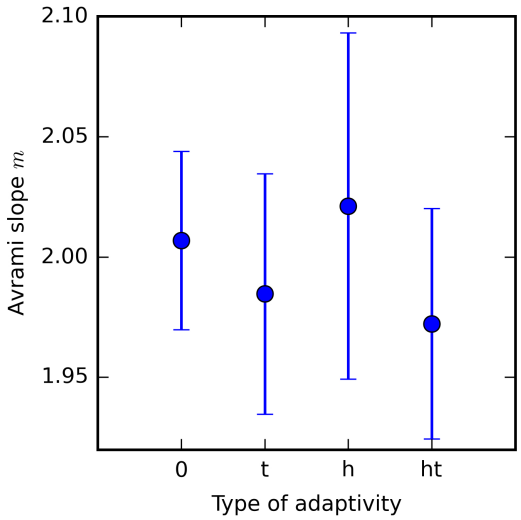

(a)

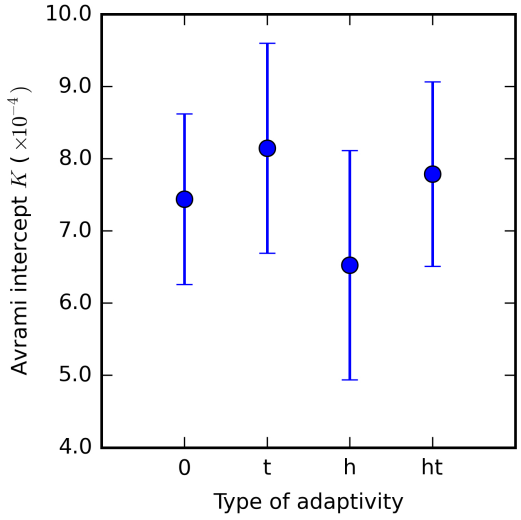

(b)

Figure 4.2.8: The average kinetic coefficients and one standard deviation (shown by the error bars) for the concurrent nucleation and growth simulations performed with no adaptivity (0), with mesh adaptivity (h), with time adaptivity (t), and both mesh and time adaptivity (ht). The information regarding the Avrami slope m is shown in (a) and the Avrami intercept K is shown in (b).

4.3 Conclusion

The explicit nucleation method described in this work is a refinement of the method developed by Simmons et al. [155, 160]. In the proposed method, OPO nucleation, a nonconserved structural order parameter is locally altered to introduce a nucleus in a coupled conserved-nonconserved phase field model. The OPO nucleus seeding method induces the formation of both a nucleus and a depletion region for the conserved variable, while naturally satisfying conservation rules. Mass conservation is naturally observed via the evolution equation instead of explicitly accounted for during nucleus introduction, simplifying the simulation code and allowing a depletion region to be formed whose profile is controlled by the model physics. In addition, numerical instabilities are avoided by eliminating sharp field gradients. The implementation details of the OPO nucleation algorithm in a finite element framework are presented, although the algorithm could be used with other numerical methods such as the finite difference method.

Upon introduction of an OPO nucleus, three processes occur concurrently: (a) a solute accumulation stage, in which solute diffuses to the nucleus, (b) the formation of a solute depletion region around the nucleus, and (c) a decrease in the structural order parameter. We describe two characteristic times within the solute accumulation stage that are based on the evolution of the conserved and nonconserved variables. The characteristic time for the conserved order parameter is the time at which solute accumulation slows significantly, and the characteristic time for the conserved order parameter identifies the time at which the value of the structural order parameter is minimal. In addition, the solute accumulation stage causes a precipitate formed by OPO seeding to be slightly smaller at a given time than one seeded with the appropriate values of both concentration and structural order parameter. However, this discrepancy can be reduced by holding the value of the structural

order parameter fixed during this stage. For the cases examined, we find that the area fraction of the OPO+hold nucleus is insensitive to the hold time for values between the the two characteristic times mentioned above. The evolution of an OPO nucleus is explained based on the free energy landscape.

The early-stage kinetics of precipitation and growth simulated with the OPO nucleation algorithm are analyzed by fitting the simulation results to the Avrami equation. With an increased nucleation rate coefficient, we obtained an Avrami coefficient as low as 1.25. A statistical analysis is performed to study the effect of mesh and/or time adaptivity on the simulated kinetics. We find the results are comparable between these data sets with different mesh and/or time adaptivity.

The explicit nucleation method presented here is general and can be straightforwardly applied to other materials systems that are described by a coupled conserved-nonconserved phase field model. However, the evolution behavior of an OPO nucleus must be analyzed to identify the hold time required, if necessary. In addition, the results should be analyzed to ensure sufficient spatial and temporal resolution with or without adaptivities. This work provides the framework for determining the adaptivity parameters, as well as the hold time.

CHAPTER V

Preliminary Work and Future Work

In this chapter, preliminary work that provides insights into the nucleation behavior of δ-hydride in α-zirconium is discussed, along with future work that would extend the α-zirconium/δ-hydride multiphysics phase field model. As described in Chapter I, hydride precipitates in zirconium develop a microstructure with features at two length scales [22,45--47]. TEM investigations have revealed that macroscopic hydrides are agglomerates of microscopic hydride stacks and that the orientation of microscopic hydrides with respect to each other affects the orientation of the resulting macroscopic hydride [22,47]. The arrangement of these microscopic δ-hydride platelets into aligned stacks is currently hypothesized to be caused by autocatalytic nucleation and elastic stabilization [22,53]. In the following sections, the sensitivities of the nucleation rate are quantitatively explored for small variations in temperature, hydrogen concentration, interfacial energy, and elastic energy. These results provide a first step in interpreting experimentally obtained hydride precipitation data, such as those found in Refs. [20,31,32,203]. Then, the spatial variation of the nucleation rate around a single, growing precipitate is studied to provide insight into the hypothesis of autocatalytic hydride nucleation. Furthermore, preliminary results of

concurrent nucleation and growth simulations are examined to study how the nucleation rate impacts the microstructural evolution. Finally, several extensions to the model are proposed as future work; topics include the terminal solid solubility hysteresis of hydrogen in zirconium and the effects of the α/δ interfacial energy, as well as thermodiffusion, plasticity, and irradiation, which are not yet accounted for in the model.

5.1 Preliminary work

5.1.1 Sensitivity of the volumetric nucleation rate

A preliminary parametric study is performed to examine the sensitivity of the nucleation rate in α-zirconium on the hydrogen content (X_H^{total}), temperature (T), interfacial energy between a nucleus and matrix (γ_{nuc}), and elastic energy density (Δg_{el}). Only one parameter is varied at a time from the nominal conditions. The nominal conditions of $T = 600$ K, within the range of the operating temperatures of fuel cladding, and $X_H^{total} = 0.05$ (approximately 580 wt ppm H), a typical hydrogen content at the end of service, are chosen. These parameters are varied over a small range of temperatures and compositions that may exist within fuel cladding during service. We also examine a range of interfacial energies within a plausible uncertainty range for interfacial energy.

The interfacial energy of a nucleating hydride, γ_{nuc}, may be a different value than the interfacial energy in the phase field model (Chapter II). While a value for the interfacial energy between the α and δ phases has not been definitively reported in the literature, the orientation relationship between microscopic δ-hydrides and α-zirconium indicates that hydrides likely precipitate with a coherent interface [152]. Therefore, $\gamma_{nuc} = 115$ mJ/m^2 is

chosen, which is within the range of 1 mJ/m^2 to 200 mJ/m^2 generally measured for coherent interfacial energies for metallic systems [152]. The only interfacial energy information available for the zirconium-hydrogen system are estimates provided for other hydride phases [150].

For the nominal conditions of $X_H^{total} = 0.05$, $T = 600$ K, $\gamma_{nuc} = 115$ mJ/m^2 and $\psi = 0.5$, the nucleation rate is $J_C = 3.76 \times 10^4$ s$^{-1}\mu m^{-3}$. At this temperature, this X_H^{total} results in a supersaturation of approximately 490 wt ppm H in the α phase. The effects of X_H^{total}, T, γ_{nuc}, or Δg_{el} on the nucleation rate are shown in Figs. 5.1.1, 5.1.2, 5.1.3, and 5.1.4 respectively. For Figs. 5.1.1, 5.1.2, and 5.1.3, $\Delta g_{el} = 0$. The nucleation rate increases by approximately an order of magnitude for each increment in X_H^{total} of 0.005 (approximately 60 wt ppm H), shown in Fig. 5.1.1. The nucleation rate decreases by approximately one order of magnitude with each 10 K increase in temperature (Fig. 5.1.2) and for every 5 mJ/m^2 increase of the interfacial energy (Fig. 5.1.3). Finally, the nucleation rate is extremely sensitive to the elastic energy density. For a misfit strain relaxation of $\psi = 0.5$, the elastic energy density within a hydride is on the order of 1×10^8 J/m^3. For that elastic energy density, the nucleation rate is decreased by five orders of magnitude with respect to the rate calculated when the elastic energy density is zero (Fig. 5.1.4), and the nucleation rate decreases more strongly as the elastic energy density increases.

The nucleation rate is extremely sensitive to the condition of the system. Small variations in temperature and hydrogen concentration, on the order of what may exist across fuel cladding while in service, have a large effect on the nucleation rate. The nucleation rate sensitivity is governed by the bulk free energy and interfacial energy. Temperature and hydrogen content, which are both variable conditions, will affect the free energy of the system and variations in their values will obviously result in variations of precipitate

microstructure. However, the calculated nucleation rate is also very sensitive to the interfacial energy, a property of the α-zirconium/δ-hydride system that should not vary with the condition of the material, and whose value has significant uncertainty. Because nucleation behavior generally has a significant impact on the resulting microstructure, the sensitivity of the calculated nucleation rate on the interfacial energy poses a significant challenge to accurate modeling of hydride precipitation and growth. Future work should examine the sensitivity of the nucleation rate for additional nominal conditions, particularly different temperatures and hydrogen compositions.

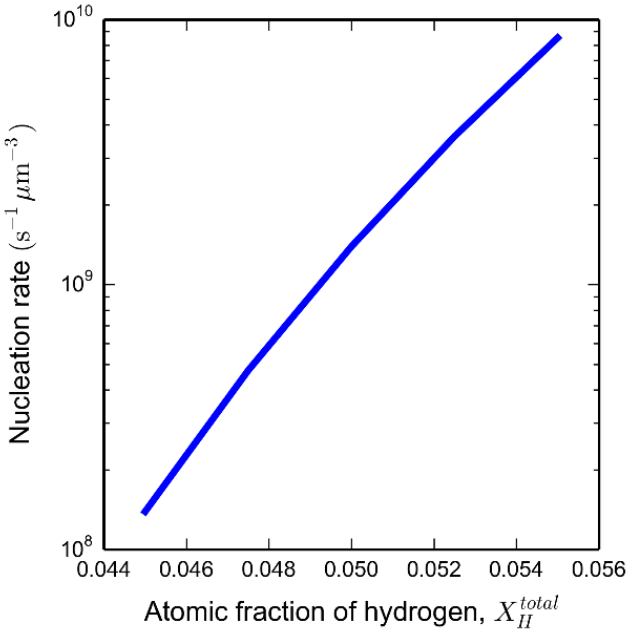

Figure 5.1.1: The nucleation rate for $X_H^{total} = 0.05 \pm 0.005$ at $T = 600$ K and $\gamma_{nuc} = 115$ mJ/m^2. The y-axis is logarithmic.

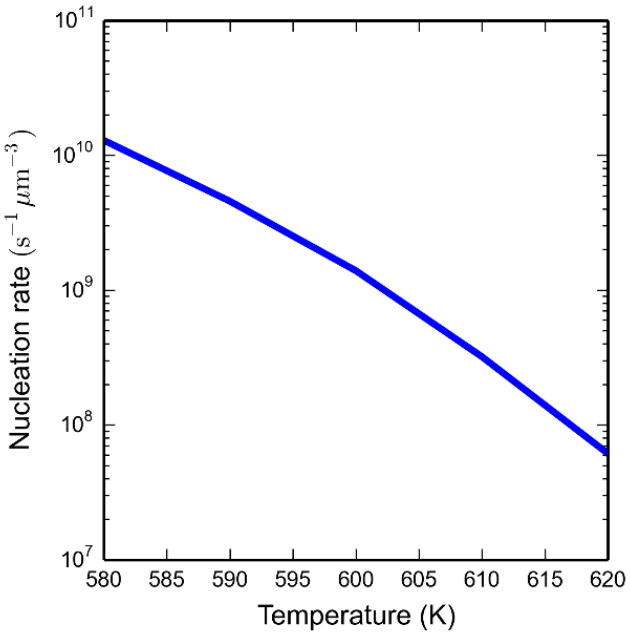

Figure 5.1.2: The nucleation rate for $T = 600 \pm 20$ K at $X_H^{total} = 0.05$ and $\gamma_{nuc} = 115$ mJ/m^2. The y-axis is logarithmic.

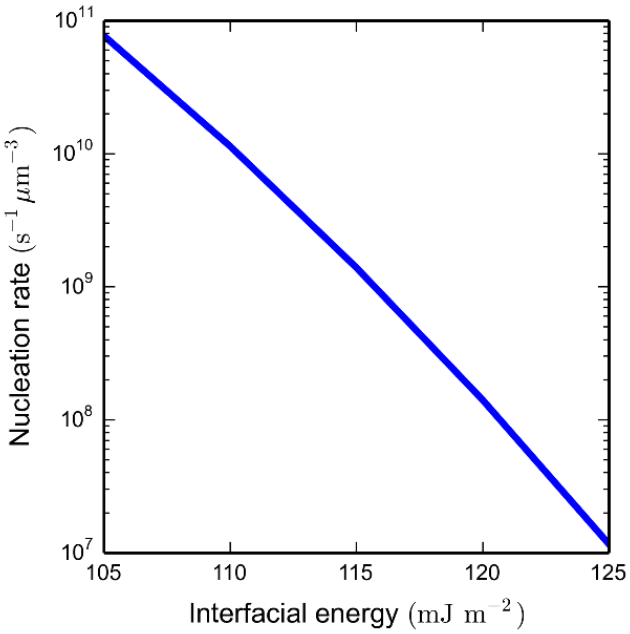

Figure 5.1.3: The nucleation rate for $\gamma_{nuc} = 115 \pm 10$ mJ/m^2 at $T = 600$ K and $X_H^{total} = 0.05$. The y-axis is logarithmic.

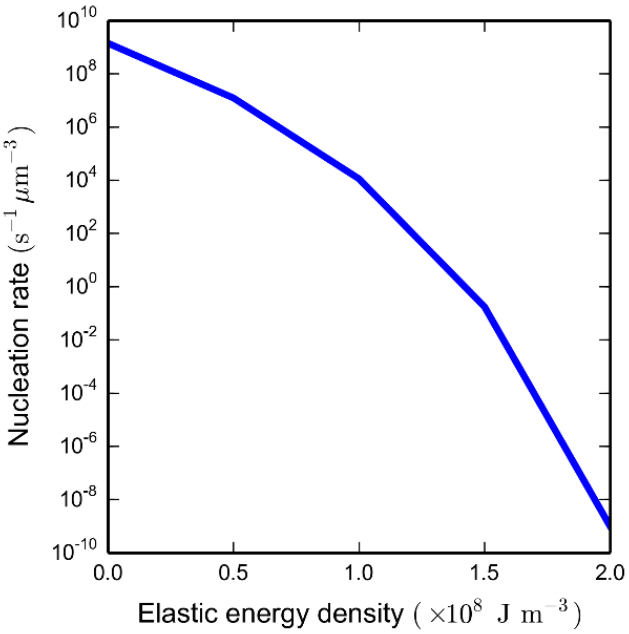

Figure 5.1.4: The nucleation rate as a function of $\Delta\bar{g}_{el}$, with $\gamma_{nuc} = 115$ mJ/m^2, $T = 600$ K and $X_H^{total} = 0.05$. The y-axis is logarithmic.

5.1.2 Spatial distribution of the volumetric nucleation rate around a precipitate

As mentioned previously, autocatalytic nucleation has been proposed as the mechanism for the alignment of microscopic hydride stacks [22, 53]. In autocatalytic nucleation, the presence of an existing hydride promotes nucleation in a preferential direction. The elastic interaction energy between an existing hydride and a nucleus is hypothesized to cause the proposed autocatalytic nucleation [22, 53]. Therefore, a preliminary study of the spatial distribution of the volumetric nucleation rate around a growing precipitate is performed.

To perform this study, an OPO hydride nucleus (Chapter IV) is seeded into a uniformly supersaturated zirconium matrix and is allowed to grow, and the volumetric nucleation rate around the precipitate is examined as the precipitate evolves. Using the volumetric nucleation rate calculated in each element allows the nucleation rate to be examined when employing adaptive meshing. A three-dimensional simulation is performed with a domain size of 250 nm $\times$250 nm $\times$ 250 nm at $T = 600$ K, $X_H^{total} = 0.05$, and misfit strain tensor relaxation of 50% ($\psi = 0.5$). To reduce resolution requirements, the interface thickness is broadened, increasing the interfacial energy in the phase field model. However, this should not affect the results presented. No-flux boundary conditions are applied for X and η and no-stress boundary conditions are applied for the displacements; in this case, the volume of the matrix phase per nucleus is similar to the computational domain size. The OPO nucleus is seeded in the form of a platelet such that the initial platelet radius is 12 nm and the initial platelet height is 8 nm, resulting in a height:width ratio of 0.667. As before, the interfacial energy $\gamma_{nuc} = 115$ mJ/m^2 is chosen for the nucleation rate calculation.

Two-dimensional slices of the 3D simulation are presented to examine the spatial distributions of the volumetric nucleation rate calculated for each element (Fig. 5.1.5), the hydrogen atomic fraction (Fig. 5.1.6), the elastic interaction energy (Fig. 5.1.7), and the chemical potential ($\delta G/\delta X$, Fig. 5.1.9a). The computational domain is cut through the $\{hki0\}$ plane family and the (0001) basal plane (the habit plane) bisecting the precipitate, where the indices are with respect to the crystallography of the zirconium matrix. The precipitate/matrix interface is indicated by a gray contour surface. In Figs. 5.1.5-5.1.7, (a) and (c) display the quantities in the $\{hki0\}$ plane family while (b) and (d) display those in the basal plane. In addition, (a) and (b) are at time $t = 2.8 \times 10^{-4}$ s, just after the precipitate has accumulated hydrogen but before it has grown, while (c) and (d) are at time

$t = 3.5 \times 10^{-3}$ s, after the precipitate has increased in volume by 370% and is in a regime of steady growth (i.e., the precipitate is growing and has attained a constant height:width ratio of 0.81).

The volumetric nucleation rate around the precipitate displays significant spatial variation; it is anisotropic in the $\{hki0\}$ plane family. In the basal plane, only very weak anisotropy is observed, which is likely due to insufficient resolution of the mesh. The anisotropy exhibits cylindrical symmetry around the $[0001]$ direction. In the $\{hki0\}$ plane family, the volumetric nucleation rate is suppressed in the $[0001]$ direction, but is increased in a region that extends at an approximately 45° angle from the basal plane of the precipitate. Further from the precipitate, the spatial distribution of the volumetric nucleation rate becomes essentially uniform. In the basal plane, the volumetric nucleation rate is increased adjacent to the precipitate for a distance of approximately 10 nm. This spatial distribution of the volumetric nucleation rate remains qualitatively unchanged as the precipitate grows, as shown in Figs. 5.1.5c and 5.1.5d. The volumetric nucleation rate far from the precipitate decreases with time due to the depletion of hydrogen from the matrix. In Figs. 5.1.5c and 5.1.5d, the volumetric nucleation rate is slightly higher in the centers of the boundary planes. This is due to the stress-free boundary condition imposed on the boundaries for the mechanical equilibrium equation, and does not significantly change the pertinent results of the simulations as long as the precipitate is sufficiently smaller than the computational domain.

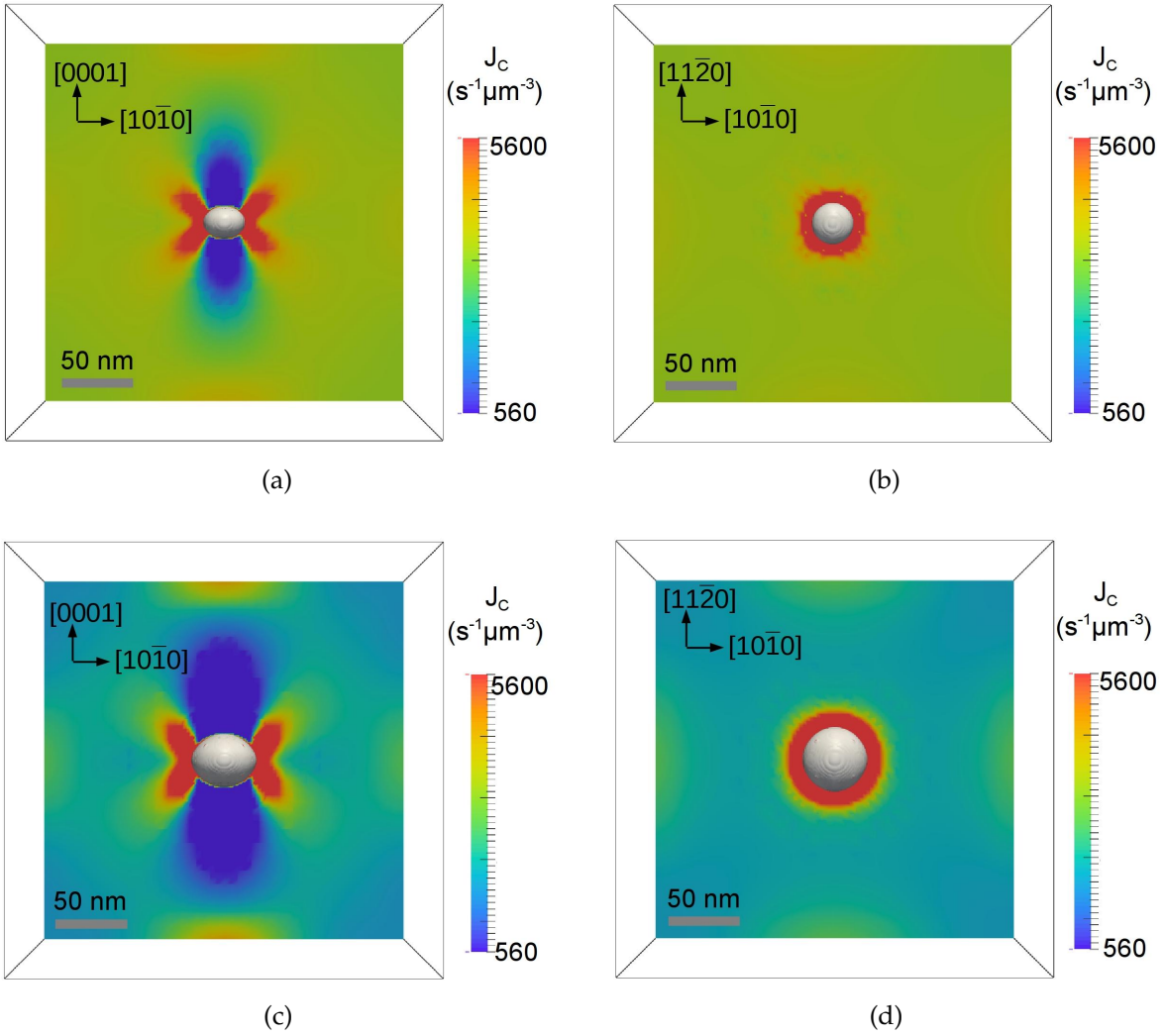

Figure 5.1.5: Two-dimensional slices of the simulated 3D spatial distribution of the volumetric nucleation rates around a growing hydride precipitate. (a) and (b) are at time $t = 2.8 \times 10^{-4}$ s and (c) and (d) are at time $t = 3.5 \times 10^{-3}$ s. (a) and (c) show the $\{hki0\}$ plane family bisecting the precipitate and (b) and (d) show the basal plane bisecting the precipitate. The gray contour surface indicates the surface of the precipitate.

Several factors may be responsible for the spatial distribution of the volumetric nucleation rate around a precipitate, including the spatial distribution of hydrogen in the matrix, the elastic interaction energy density, $\Delta\bar{g}^{interaction}_{elastic}$, of a potential nucleus accounting

for the local stress (Chapter II), and a transient kinetic effect. Figure 5.1.6 illustrates the spatial distribution of hydrogen around the growing precipitate. The spatial distribution of hydrogen in the matrix is very similar to the volumetric nucleation rate distribution, indicating that the hydrogen distribution around the precipitate has a strong effect on the nucleation rate. In the $\{hki0\}$ plane family, the atomic fraction of hydrogen is decreased in the $[0001]$ direction but increased in a region that extends at an approximately 45° angle from the basal plane of the precipitate. Further from the precipitate, the spatial distribution of hydrogen becomes nearly uniform. In the basal plane, the atomic fraction of hydrogen is increased adjacent to the precipitate for a distance of approximately 10 nm.

The strong correlation between the volumetric nucleation rate and the hydrogen concentration can be understood through the critical energy barrier for nucleation, ΔG_C (Chapter II). As the hydrogen concentration in the supersaturated matrix increases, ΔG_C decreases. The nucleation rate is exponentially dependent upon $-\Delta G_C$, such that a small increase in hydrogen concentration significantly increases the nucleation rate; this was also observed in the results in Section 5.1.1. Both the spatial distribution of the volumetric nucleation rate and the spatial distribution of hydrogen in the matrix could lead to the formation of the aligned nanoscale hydride stacks observed via TEM [22, 47]; an enhanced volumetric nucleation rate leads to a greater probability of precipitate formation in that region, while the increased hydrogen content would promote the growth of nucleated hydrides.

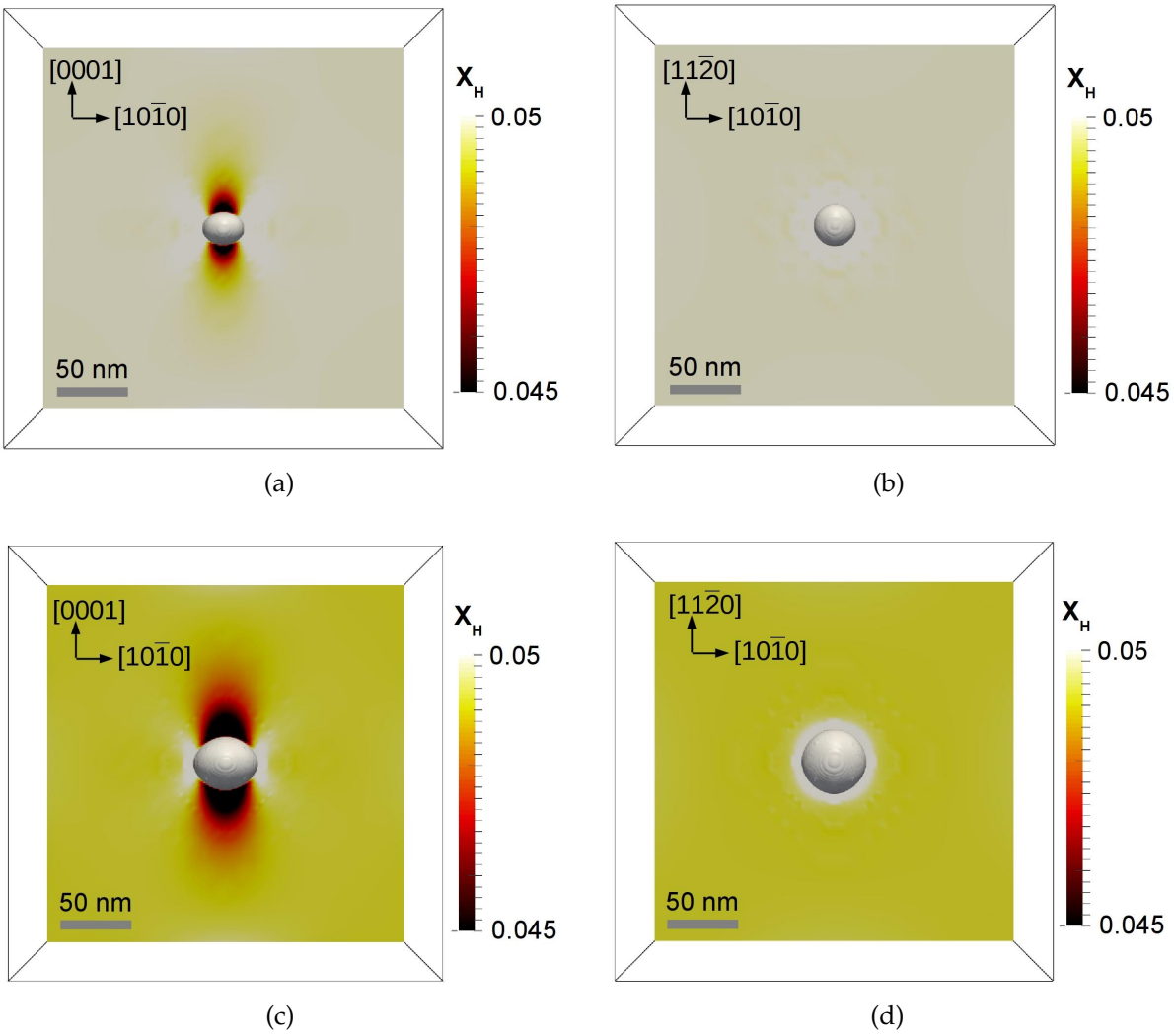

Figure 5.1.6: Two-dimensional slices of the simulated 3D the spatial distributions of hydrogen around a growing hydride precipitate. (a) and (b) are at time $t = 2.8 \times 10^{-4}$ s and (c) and (d) are at time $t = 3.5 \times 10^{-3}$ s. (a) and (c) show the $\{hki0\}$ plane family bisecting the precipitate and (b) and (d) show the basal plane bisecting the precipitate. The gray contour surface indicates the surface of the precipitate.

Autocatalytic nucleation has been proposed as the mechanism by which precipitate arrays form, and it has been hypothesized that $\Delta\tilde{g}^{interaction}_{elastic}$ is the cause of autocatalytic nucleation [53, 170, 204]. The total elastic strain energy density of a nucleus can be consid-

ered as the sum of the ''self'' energy density of an isolated precipitate in an unstressed matrix, which is constant, and an ''interaction'' term with local stress due to the presence of coherent precipitates, applied stress, etc. (Chapter II). Thus, only the interaction term is studied next. Figure 5.1.7 illustrates the spatial distribution of $\Delta\bar{g}_{elastic}^{interaction}$. A positive elastic interaction energy density will suppress the volumetric nucleation rate, and a negative elastic interaction energy density will enhance it. The nucleation rate is affected because the bulk thermodynamic driving force for nucleation is decreased or increased, respectively.

The spatial distribution of the elastic interaction energy density is similar to the volumetric nucleation rate distribution; in the $\{hki0\}$ plane family, the elastic interaction energy density is positive in the $[0001]$ direction, but negative in a region that extends at an approximately 45° angle from the basal plane of the precipitate. Further from the precipitate, the elastic interaction energy density decays to zero. In the basal plane, the elastic interaction energy density is negative adjacent to the precipitate for a distance of approximately 2 nm. While the spatial distributions of the elastic interaction energy density and volumetric nucleation rate may be qualitatively similar, the magnitude of $\Delta\bar{g}_{elastic}^{interaction}$ is much greater for positive $\Delta\bar{g}_{elastic}^{interaction}$ values than negative $\Delta\bar{g}_{elastic}^{interaction}$ values. In addition, the region of the matrix in which $\Delta\bar{g}_{elastic}^{interaction}$ is significantly negative is only approximately 2 nm wide around the edge of the platelet. However, the region of the matrix in which $\Delta\bar{g}_{elastic}^{interaction}$ is significantly positive extends for tens of nanometers into the matrix above and below the precipitate. Thus, the overall effect of the elastic interaction energy is to suppress the volumetric nucleation rate. This is in contradiction with the hypotheses proposed in the literature [53,170,204] that the elastic interaction energy enhances nucleation.

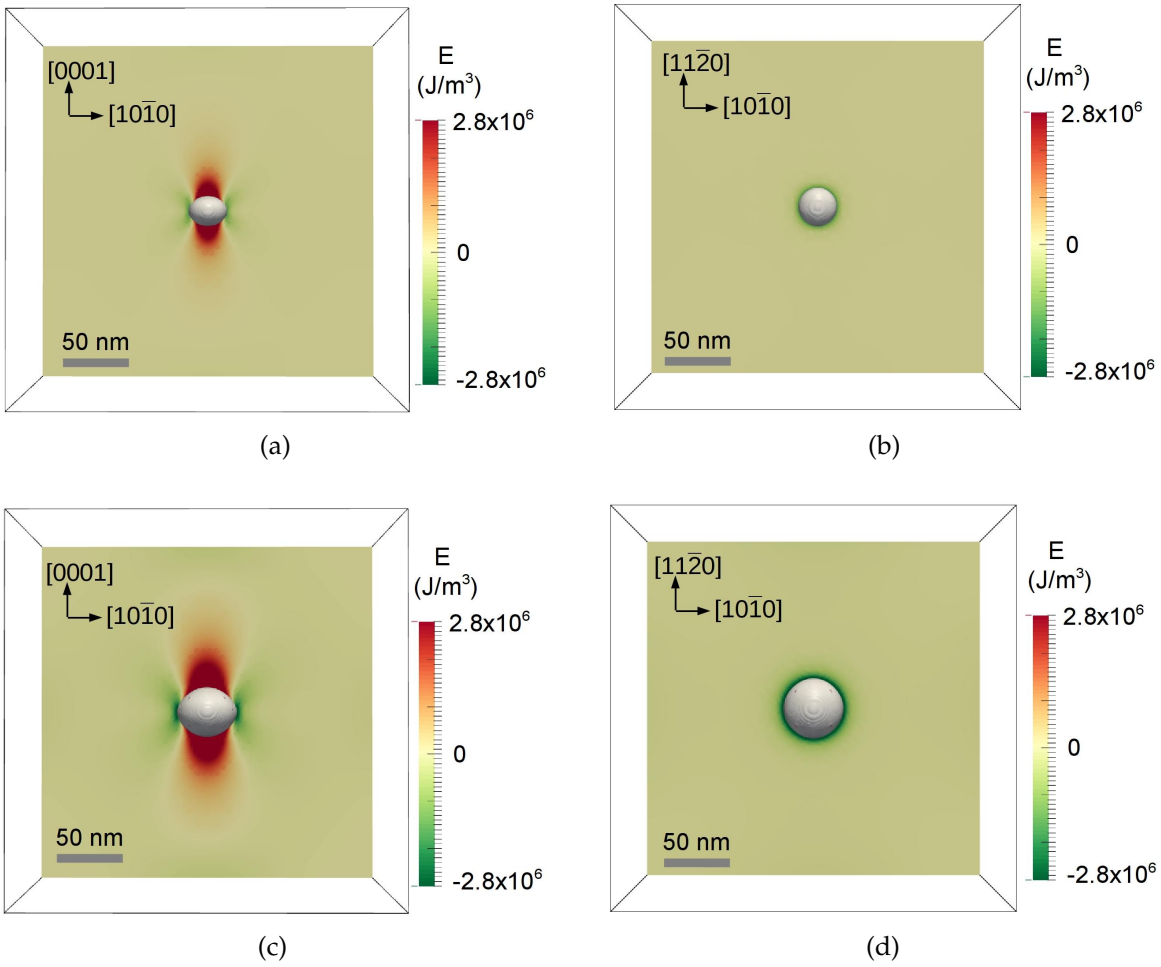

Figure 5.1.7: Two-dimensional slices of the simulated 3D spatial distributions of the elastic interaction energy, Δg_{el}^{int}, surrounding a growing hydride precipitate. (a) and (b) are at time $t = 2.8 \times 10^{-4}$ s and (c) and (d) are at time $t = 3.5 \times 10^{-3}$ s. (a) and (c) show the $\{hki0\}$ plane family bisecting the precipitate and (b) and (d) show the basal plane bisecting the precipitate. The gray contour surface indicates the surface of the precipitate.

The dominant factor affecting the volumetric nucleation rate may be determined by examining the similarities between the distributions of the volumetric nucleation rate (Fig. 5.1.5), the hydrogen composition (Fig. 5.1.6), and the elastic interaction energy density (Fig. 5.1.7). For the hydrogen composition simulated, the distribution of hydrogen around the

precipitate is primarily responsible for the spatial variation of the volumetric nucleation rate.

While the hydrogen distribution controls the nucleation rate, both the hydrogen distribution and the elastic interaction energy density distribution are a result of stresses in the matrix induced by the presence of the precipitate. Hydrogen induces an anisotropic dilational strain in α-zirconium that is proportionate to its concentration (the hydrogen distortion strain tensor has equal values in the $[10\bar{1}0]$ and $[11\bar{2}0]$ directions and the largest value in the $[0001]$ direction) [144, 145]. Therefore, hydrogen will diffuse in a stress field to reduce elastic strain energy. Because hydrogen induces a stress-free expansion of α-zirconium, it will diffuse to areas of tensile stress. Figure 5.1.8 illustrates the hydrogen distribution in the matrix and the compressive and tensile stress contours for σ_{xx}, σ_{yy}, and σ_{zz} (the normal stresses in the $[10\bar{1}0]$, $[11\bar{2}0]$, and $[0001]$ directions, respectively). The precipitate is at the center of the contours and is indicated by a gray surface. Matching contour shapes indicate that the hydrogen distribution is primarily affected by σ_{zz}. Where σ_{zz} is compressive, the concentration of hydrogen is decreased, and where σ_{zz} is tensile, the concentration of hydrogen is increased. As the magnitude of σ_{zz} increases, the hydrogen concentration is increasingly affected. It is likely that σ_{zz} is the dominant stress controlling the hydrogen distribution because both the α/δ misfit strain and the distortion strain tensor of hydrogen in solution with α-zirconium are greatest in the $[0001]$ direction, inducing the largest stress and having the greatest contribution to the elastic strain energy.

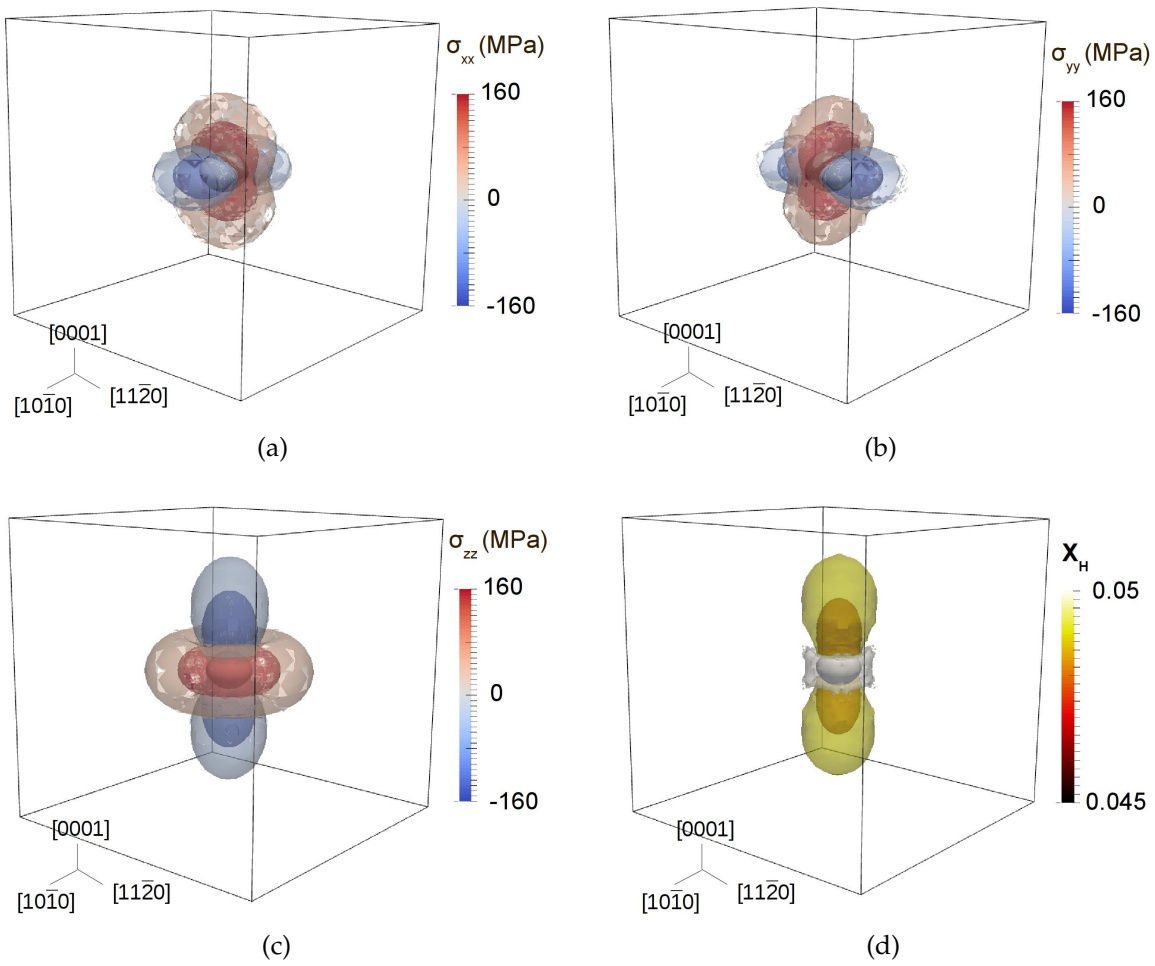

Figure 5.1.8: Contours of (a) the normal stress σ_{xx}, (b) the normal stress σ_{yy}, (c) the normal stress σ_{zz}, and (d) the hydrogen atomic fraction in the zirconium matrix, X. The time is $t = 2.8 \times 10^{-4}$ s. Contour roughness is an artifact of a nonuniform mesh.

To determine whether the the observed distribution of hydrogen is transient resulting from the initial conditions, the chemical potential of hydrogen is examined. Figure 5.1.9a-5.1.9c shows the chemical potential, μ, $\partial g_{chem}/\partial X$, and $\partial g_{el}/\partial X$, respectively, at $t = 2.8 \times 10^{-4}$ s, where

$$\mu = \frac{\partial g_{chem}}{\partial X} + \frac{\partial g_{el}}{\partial X}, \tag{5.1.1}$$

g_{chem} is the chemical free energy density, and g_{el} is the elastic energy density (Chapter II). While the chemical potential will not be constant until the system achieves equilibrium, the gradient of the chemical potential around the precipitate indicates whether the hydrogen distribution is a transient phenomenon or is a characteristic behavior of the diffusion-controlled growth of the precipitates. If the hydrogen distribution is a characteristic behavior, the gradient in the chemical potential will reflect the shape of the precipitate [202], while if the hydrogen distribution is transient, the gradient of the chemical potential will not reflect the shape of the precipitate. As shown in Fig. 5.1.9a, the gradient of the chemical potential reflects the shape of the precipitate, indicating that the hydrogen distribution is not a transient phenomenon. The chemical (Fig. 5.1.9b) and elastic (Fig. 5.1.9c) components of the total chemical potential do not reflect the shape of the precipitate, but their spatial variations oppose each other to yield a chemical potential gradient that does reflect the precipitate shape. In other words, if $\partial g_{el}/\partial X$ is more negative at a given position, $\partial g_{chem}/\partial X$ is less negative, and vice versa.

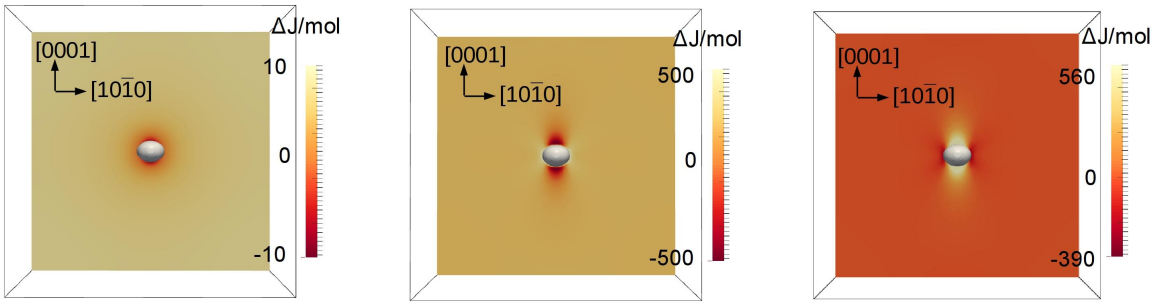

(a) (b) (c)

Figure 5.1.9: The spatial distribution of (a) the total chemical potential, μ, around a growing precipitate, which is the sum of (b) the chemical contribution, $\partial g_{chem}/\partial X$, and (c) the elastic contribution, $\partial g_{el}/\partial X$. For ease of comparison, the values for each quantity are rescaled with respect to their minimum and maximum such that the mean value is set as zero. The time is $t = 2.8 \times 10^{-4}$ s.

While the results of this analysis provide significant insight into the spatial distribution of the volumetric nucleation rate surrounding a precipitate, additional simulations should be performed to expand the parametric space explored. Different hydrogen compositions and misfit strain relaxations as well as more realistic interfacial energies can be utilized to determine whether hydrogen concentration remains the dominant factor controlling the nucleation rate, or if elastic interaction energy becomes important at lower hydrogen concentrations. Finally, the hydrostatic stress, σ_m, could be examined to determine which stress (σ_{zz} or σ_m) most strongly influences the system.

5.1.3 Concurrent nucleation and growth simulations

In Chapter III, the concurrent nucleation and growth algorithm was designed and implemented, and in Chapter IV, the CALPHAD-based free energy formulation for a phase field model was tested. These components are combined with elastic strain energy to

perform preliminary concurrent nucleation and growth simulations for the α-zirconium/δ-hydride system. The effect of the interfacial energy, γ_{nuc}, on the microstructural evolution is studied. The interfacial energy has a strong effect on the volumetric nucleation rate, as shown earlier in this chapter. As mentioned in Chapter II, the α/δ interfacial energy has not been well characterized in the literature, so the effect of uncertainty in the interfacial energy must be characterized.

Simulations are performed at a constant temperature and with an initially uniform hydrogen concentration. These conditions simulate a ''quench and hold'' precipitation experiment. Due to computational resources, simulations are performed in 2D, with 3D simulations left for future work. Two-dimensional simulations in the $\{hki0\}$ plane family are performed with a domain size of 2μm $\times 2\mu$m, with $T = 600$ K, $X_H^{total} = 0.05$, and $\psi = 0.5$. The $\{hki0\}$ plane family is selected for simulation because the system is highly anisotropic in that plane family. No-flux and no-stress boundary conditions are applied. For the volumetric nucleation rate calculation, the 3D volume for each 2D element is calculated by $A_{elem} \cdot h$, where A_{elem} is the area of the element and $h = 20$ nm is a fixed height, taken as the maximum side length of an element.

Figure 5.1.10 shows snapshots from a 2D microstructural evolution simulation when $\gamma_{nuc} = 110$ mJ/m^2, while Fig. 5.1.11 presents those for $\gamma_{nuc} = 115$ mJ/m^2. Each figure shows the atomic fraction of hydrogen. Blue indicates hydrogen depletion, and red indicates hydrogen enhancement; a hydride is present at the center of each hydrogen depletion region. The same times are shown in Figs. 5.1.10b and 5.1.11a, and Figs. 5.1.10c and 5.1.11b. In Fig. 5.1.10, many nuclei form in a brief period of time and the hydrides are small and relatively uniform in size, 17 nm to 18 nm in diameter. In total, 25 hydride precipitates form over 2.0×10^{-4} s, leading to an average volumetric nucleation rate of

1.6×10^6 nuclei $s^{-1}\mu m^{-3}$. In comparison, precipitate formation is much rarer in Fig. 5.1.11 than in Fig. 5.1.10, leading to a larger distribution in precipitate sizes (20 nm to 65 nm in diameter). In total, 11 precipitates form over 2.2×10^{-3} s, leading to an average volumetric nucleation rate of 6.3×10^4 nuclei $s^{-1}\mu m^{-3}$. Due to the higher volumetric nucleation rate in Fig. 5.1.10, the length of time simulated is much shorter than for Fig. 5.1.11.

The evolutions of the two microstructures to $t = 7.4 \times 10^{-5}$ s are very different. Notably, the number of hydride precipitates formed and the size distribution of the precipitates vary significantly, even though the difference in γ_{nuc} is only 5 mJ/m^2. It is likely that the final microstructures would be very different, with a large number of small, closely spaced precipitates for the $\gamma_{nuc} = 110$ mJ/m^2 simulation and a small number of large precipitates for the $\gamma_{nuc} = 115$ mJ/m^2. These results indicate that it is essential to employ an accurate value of the interfacial energy between the matrix and nucleating phases in order to quantitatively model microstructural evolution that involves nucleation. Future simulations should examine the effect of different hydrogen concentrations, interfacial energies, and applied stresses, as well as to investigate longer evolution times.

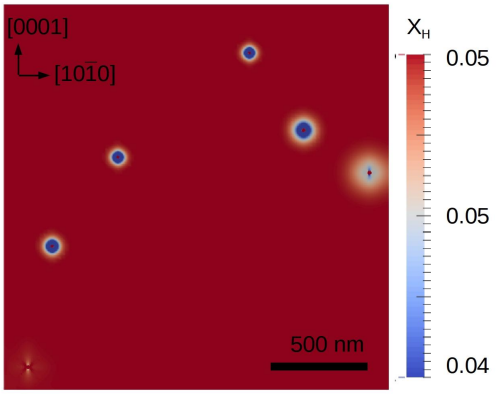

(a)

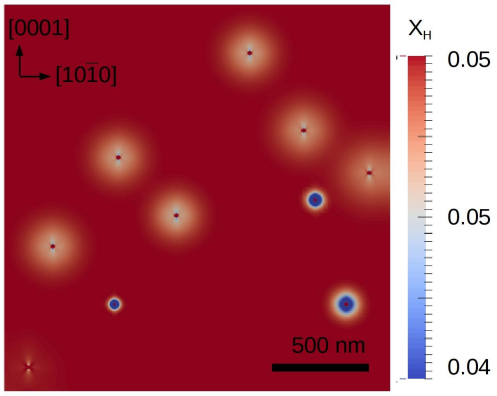

(b)

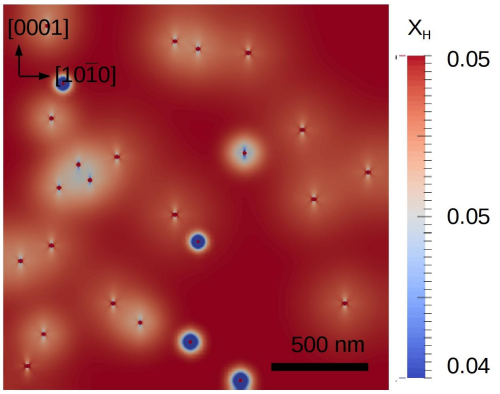

(c)

Figure 5.1.10: Two-dimensional simulation of the evolution of hydride precipitation and growth with $\gamma_{nuc} = 110$ mJ/m^2. (a) $t = 3.2 \times 10^{-5}$ s, (b) $t = 7.4 \times 10^{-5}$ s, (c) $t = 2.0 \times 10^{-4}$ s. A hydride is in the center of each hydrogen depletion region. The temperature is 600 K, and $X_H^{total} = 0.05$.

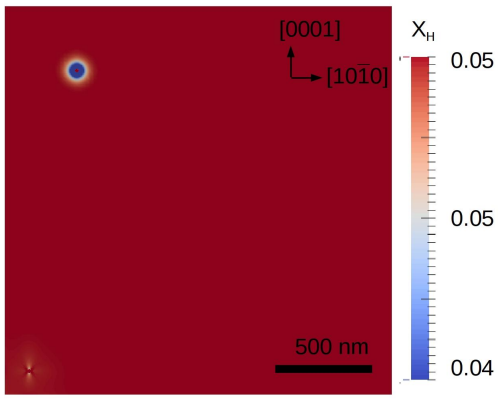

(a)

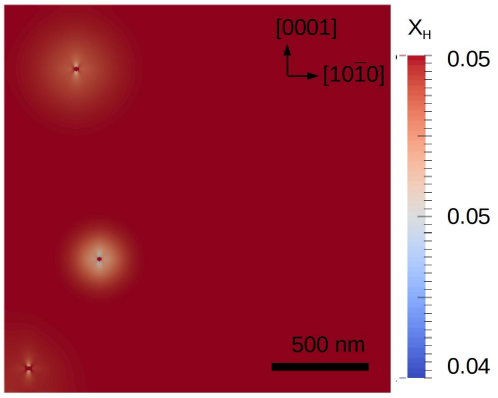

(b)

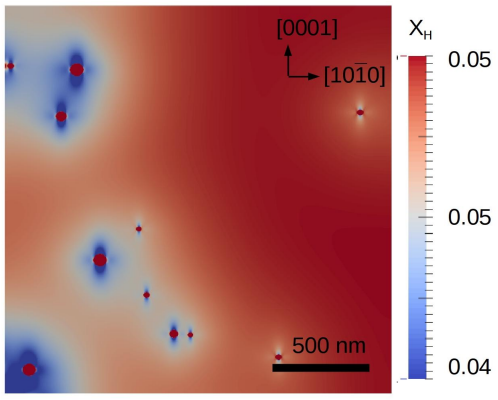

(c)

Figure 5.1.11: Two-dimensional simulation of the evolution of hydride precipitation and growth with $\gamma_{nuc} = 115$ mJ/m^2. (a) $t = 7.4 \times 10^{-5}$ s, (b) $t = 2.0 \times 10^{-4}$ s, (c) $t = 2.2 \times 10^{-3}$ s. A hydride is visible in the center of each hydrogen depletion region. The temperature is at 600 K, and $X_H^{total} = 0.05$.

5.2 Future Work

This thesis presents a quantitative multiphysics phase field model of the α-zirconium/δ-hydride system and its simulation results. As already mentioned, the studies presented in Section 5.1 may be expanded. The sensitivity of the nucleation rate may be studied for additional nominal conditions, particularly different temperatures and hydrogen compositions. To further examine the spatial distribution of the nucleation rate around a precipitate, different hydrogen compositions and misfit strain relaxations as well as more realistic interfacial energies can be utilized. Finally, concurrent nucleation and growth simulations may be performed to examine the effect of different hydrogen concentrations, interfacial energies, and applied stresses, as well as to investigate longer evolution times.

The remainder of this section discusses additional avenues for future work. Topics include the terminal solid solubility hysteresis of hydrogen in zirconium and the effects of the α/δ interfacial energy, as well as thermodiffusion, plasticity, and irradiation, which are not yet accounted for in the model.

5.2.1 Terminal solid solubility hysteresis of hydrogen in α-zirconium

For a given composition, the temperature at which hydrides precipitate and dissolve is not the same, a phenomenon termed terminal solid solubility (TSS) hysteresis (for an introduction, see Chapter I). This behavior is significant for microstructural evolution modeling of fuel cladding material, as it can strongly affect the predicted microstructure. However, the existing theory to explain TSS hysteresis for the α-zirconium/δ-hydride system [36,37] is based on the coherent solvus; this theory does not account for interfacial energy and the nucleation energy barrier. Therefore, the TSS hysteresis in α-zirconium

alloys upon heating and cooling is explored. In this section, methods are given to calculate the coherent solvus, the hydrogen concentration needed to cause the growth of a nanoscale hydride, and the hydrogen concentration needed nucleate hydrides. In addition, several suggestions for future work are provided.

First, the coherent solvus for α-zirconium/δ-hydride may be calculated for different values of misfit strain relaxation, ψ (see Chapter II), similar to the analysis in Refs. [36,37]. The coherent solvus is found by determining the composition of α-zirconium given by the common tangent of the free energies of the α and δ phases when the elastic energy density of δ-hydride, Δg_{el}^{δ}, is included into the energy of the δ-phase [205]. In these calculations, a spherical hydride may be assumed, both for simplicity and because interfacial energy likely dominates the precipitate shape at the nanoscale. Future work should investigate how Δg_{el}^{δ} varies with hydride shape and how that variation affects the coherent solvus, as micron-scale δ-hydrides appear as platelets. Furthermore, more detailed estimates of how the misfit strain is relaxed in the $[10\bar{1}0]$, $[11\bar{2}0]$, and $[0001]$ directions should be made to understand how the relaxation may affect Δg_{el}^{δ} and the calculated solubility limit.

Phase field modeling may be employed to calculate the hydrogen concentration required to induce the growth of a nanoscale hydride, important information for engineering-scale fuel cladding models. To do so, a single precipitate would be allowed to grow to equilibrium, and the final composition of the α phase provides the result. In this model, the Gibbs-Thomson effect for a finite-sized precipitate with curved interfaces will alter the hydrogen composition from the coherent solubility limit. The value of ψ may be varied between 0 and 1, and the interfacial energy should be adjusted accordingly (see Chapter II for a discussion). If future work supplies additional information about the α/δ interfacial dislocation structure and the interfacial energy, this data could be incorporated

into the phase field model. Furthermore, the composition necessary to induce the growth of multiple, elastically interacting particles could be studied, as elastic interaction could have a significant effect on the stress state within the precipitates.

Nucleation behavior is not captured in the previous models, but nucleation must occur during hydride precipitation. Therefore, classical nucleation theory may be employed to calculate the hydrogen composition required to nucleate hydrides. To do so, a nucleation rate may be estimated from experimental data [20, 31, 32, 203], and the composition required to achieve the given rate may be calculated. Multiple rates should be examined to determine the sensitivity of the composition on the rate. Given the uncertainty of the α/δ interfacial energy, the interfacial energy should be a freely varied parameter. The density of nucleation sites should be varied to explore heterogeneous and homogeneous nucleation. Furthermore, calculations should be made both including and excluding elastic energy. As suggested in Refs. [33, 203], interfacial energy alone may be sufficient to cause the observed TSS hysteresis. If that is true, then some mechanism of relaxing the misfit strain energy between the hydride and matrix would be necessary, such as nucleation on dislocations or within the tensile strain fields of dislocations [206, 207]. To further study nucleation in the α-zirconium/δ-hydride system, phase field simulations of concurrent nucleation and growth could be performed, but computational efficiency would need to be increased (see Section 5.2.2).

Below, several suggestions are made for both experimental and theoretical research to extend and refine the models presented in this thesis. First, given the likelihood that the microstructure of samples used in TSS experiments is affected by the thermal history, future experiments should report the detailed thermal histories of the samples. In addition, the grain structure and dislocation structure should be characterized after

each part of the experiments' thermal cycles to determine if the matrix microstructure evolves. Next, *in-situ* TEM experiments of hydride dissolution and precipitation at fixed compositions could provide information such as the hydride nucleation rate, nucleation location (homogeneous or heterogeneous), hydride elastic strain, and interfacial structure. The sample temperature and sample composition would need to be carefully measured to minimize uncertainty, as small changes in these values can strongly affect the predictions made by classical nucleation theory. Furthermore, density functional theory could be applied to calculate the α-zirconium/δ-hydride interfacial energy. Molecular dynamics or other atomic-scale techniques could be employed to study the nucleation and growth of a single hydride, particularly the evolution of the elastic strain within a hydride and its interfacial structure. This information could be used within a phase field model to remove assumptions made in this work in how misfit strain relaxation is incorporated and how the value of the interfacial energy is adjusted.

5.2.2 Interfacial energy

The Wheeler-Boettinger-McFadden-type (WBM) free energy formulation [97] of the α-zirconium/δ-hydride model presented in this work limits the diffuse interface width to several nanometers when incorporating realistic interface energies. With the CALPHAD-based free energy formulation in this thesis, an inherent interfacial energy contribution exists even when the imposed energy barrier parameter w is set to zero. This inherent energy barrier limits the width that the diffuse interface may take for a specified interfacial energy. A wider diffuse interface enables lower resolution to be used within the simulation, reducing computational resource requirements.

Two potential solutions could overcome the existing limitation on the diffuse interface

width. Shen et al. proposed a method to lower the inherent energy barrier in a CALPHAD-based free energy description of a nickel-aluminum system in which both precipitate growth and coarsening were simulated [208]. The chemical free energy was multiplied by a modifying function that decreased the energy barrier between the two phases while leaving the energy wells of the two phases essentially unchanged [208], enabling a wider diffuse interface width to be used for a given interfacial energy. A similar approach might be applicable to the α-zirconium/δ-hydride system. The other alternative is to reformulate the α-zirconium/δ-hydride model as a Kim-Kim-Suzuki-type (KKS) phase field model [188]. In the KKS model, the diffuse interface is regarded as a mixture of the two phases such that the interface width is decoupled from the interfacial energy. However, the KKS model is more complex, both mathematically and computationally, than the WBM model. Recently, the general KKS model has been implemented within the MOOSE phase field module. Reformulation and reimplementation of the α-zirconium/δ-hydride model may be relatively simple with the new functionalities being added.

While the diffuse interface width within the phase field model presents a difficulty, the interface poses a problem from a physical perspective as well. As mentioned throughout this thesis, the microstructural evolution, particularly the nucleation behavior, is highly sensitive to the interfacial energy. However, the α/δ interfacial energy has not been well characterized. An accurate determination of the α/δ interfacial energy will further enhance the capabilities of the multiphysics phase field model presented here, enabling more accurate modeling of concurrent nucleation and growth processes.

5.2.3 Thermodiffusion

While isothermal conditions are often studied in the laboratory, fuel cladding expe-

riences thermal gradients during service. Fuel cladding is hotter on the fuel side and cooler on the water side, and the thermal gradient provides an additional driving force for hydrogen diffusion as well as introducing spatial variation in the thermodynamic and kinetic states of the material. Therefore, it is important to be able to model the diffusion of hydrogen in a temperature gradient in a thermodynamically consistent fashion. Hydrogen in zirconium diffuses to colder areas [209,210], which is termed the Soret effect or thermodiffusion. The phase field model for the α-zirconium/δ-hydride system proposed in this work has been validated for isothermal conditions, but not for non-isothermal conditions.

Experimentally, the diffusion of hydrogen in a temperature gradient has been measured as the heat of transport, Q^* [209,210]. The heat of transport describes the flux of hydrogen in zirconium in combination with the isothermal diffusion coefficient. To understand the relevance of the heat of transport and to correctly incorporate it into the phase field model, it must be interpreted within the mathematical framework of linear irreversible thermodynamics [96].

Linear irreversible thermodynamics is based on force-flux relationships [96], in which the flux of a quantity is a function of the thermodynamic driving force and the kinetic coefficient associated with the quantity. If two quantities (e.g., a solute and heat) are diffusing within the same system, their fluxes may be coupled, which is represented by coupling kinetic coefficients. For the hydrogen-zirconium system, the flux $\mathbf{J}_i$, where i indicates the quantity diffusing, of hydrogen, H, and heat, Q, is given as [96]

$$\mathbf{J}_H = L_{HH}F_H + L_{HQ}F_Q \tag{5.2.1}$$

and

$$\mathbf{J}_Q = L_{QH}F_H + L_{QQ}F_Q, \tag{5.2.2}$$

where F_i is the driving force for each quantity, L_{ij} is the kinetic coefficient, and the subscripts of L indicate if it is a direct or coupling coefficient, represented by the same or different subscripts, respectively. The flux must have units of *quantity* $\mathrm{m}^{-2}\mathrm{s}^{-1}$, where the quantity is energy (Joules) for Q and moles for H. The units of L_{ij} and F_i may vary depending on the definition of the driving force [96], but they must combine to produce the appropriate units for the flux. In a system with only chemical energy, the driving force for hydrogen is given as $-\nabla\mu_H$ (with units of J $\mathrm{m}^{-1}\mathrm{mol}^{-1}$) and the driving force for heat is given as $-\nabla T/T$ with units of m^{-1} [96].

By substituting in the expressions for the driving forces in Eqs. 5.2.1 and 5.2.2, the flux expressions become

$$\mathbf{J}_H = -L_{HH}\nabla\mu_H - L_{HQ}\nabla T/T \tag{5.2.3}$$

and

$$\mathbf{J}_Q = -L_{QH}\nabla\mu_H - L_{QQ}\nabla T/T. \tag{5.2.4}$$

By applying the chain rule of differentiation, the flux expressions are given as

$$\mathbf{J}_H = -L_{HH}\left(\frac{\partial\mu_H}{\partial c_H}\nabla c_H + \frac{\partial\mu_H}{\partial T}\nabla T\right) - \frac{L_{HQ}}{T}\nabla T \tag{5.2.5}$$

where c_H is the concentration of hydrogen in mol/m^3, and

$$\mathbf{J}_Q = -L_{QH}\left(\frac{\partial \mu_H}{\partial c_H}\nabla c_H + \frac{\partial \mu_H}{\partial T}\nabla T\right) - \frac{L_{QQ}}{T}\nabla T \tag{5.2.6}$$

where the flux of hydrogen is dependent on both the gradient in hydrogen concentration and the gradient in temperature. By collecting terms in Eq. 5.2.5,

$$\mathbf{J}_H = -L_{HH}\frac{\partial \mu_H}{\partial c_H}\nabla c_H - \left(L_{HH}\frac{\partial \mu_H}{\partial T} + \frac{L_{HQ}}{T}\right)\nabla T \tag{5.2.7}$$

results [96].

The flux of hydrogen that arises from the gradient in concentration is an expression of Fick's First Law, where $L_{HH}\partial\mu_H/\partial c_H$ is the diffusivity (note that $\partial\mu_H/\partial c_H$ is the thermodynamic factor arising from the free energy). However, the equation contains two additional terms, both of which are proportional to ∇T. The flux term $L_{HH}\partial\mu_H/\partial T$ depends on the direct hydrogen coupling coefficient and the free energy, but the term L_{HQ}/T incorporates the indirect heat-hydrogen coupling kinetic coefficient, L_{HQ}, which may be zero or positive. The heat of transport is given by $Q^* = L_{HQ}/L_{HH} - T\left(\partial\mu/\partial T\right)$ [96], terms that exist in the coefficient of ∇T in Eq. 5.2.7. Therefore, the experimentally measured heat of transport incorporates information about the free energy as well as the indirect kinetic coupling coefficient.

While the temperature dependence of the chemical potential may be calculated from $G^{0,\alpha}_{mix}(X,T)$ and $G^{0,\delta}_{mix}(X,T)$, it is unknown if the coupling coefficient L_{HQ} is nonzero. In addition, the CALPHAD free energy description of $\partial\mu_H/\partial T$ should be verified. The data used in the parameterization of $G^{0,\alpha}_{mix}$ and $G^{0,\delta}_{mix}$ were primarily isothermal [98]; uncertainty in the data or the parameterization could influence $\partial\mu_H/\partial T$ in ways that do not affect

the resulting isothermal phase boundaries. Finally, it must be determined whether the heat of transport includes a non-zero L_{HQ} term. A differential heat flux experiment could determine if L_{HQ} is non-zero, which is proposed as follows. An large temperature gradient would be applied across an insulated rod of hydrogen-free zirconium. For example, one end of the rod would be at room temperature, while the other would be in a furnace. Heat flux sensors on either end of the rod would measure the heat flux to calibrate the experiment. After measuring the heat flux, the rod would be charged with zirconium and isothermally annealed to ensure a uniform distribution of hydrogen. Then, the rod would experience the same thermal gradient/heat flux experiment. The differential heat flux would indicate if L_{HQ} is non-zero (if the differential is zero, then L_{HQ} is zero).

5.2.4 Plasticity and irradiation

Two additional extensions of the model include the incorporation of plasticity beyond misfit dislocations and irradiation effects. Plasticity and irradiation play a significant role in the microstructural evolution of zirconium alloy fuel cladding. Dislocations may form at the α/δ interface and may break away from the hydride, raising the interfacial energy, relaxing the α/δ misfit strain, and potentially providing nucleation sites for hydrides. Incorporating dislocation dynamics [211,212] or elasto-plastic modeling [63,64], for example, would provide an additional insight into how misfit strain relaxation affects the microstructural evolution of the system. Dislocation dynamics can simulate how individual dislocations move, multiply, and interact in response to internal and external stresses. Conversely, elasto-plastic phase field modeling describes plastically strained regions with an additional order parameter. These models could potentially be used to evolve the α/δ misfit strain during the phase field simulation or to help parameterize the

nucleation model. In addition, the incorporation of irradiation effects will enhance the ability to model hydride precipitation and growth in reactor conditions. For example, irradiation increases both the TSSd and the TSSp of α-zirconium [30] and increases the yield strength of the material [213].

5.3 Summary

In this chapter, preliminary investigations of the nucleation behavior of δ-hydride in α-zirconium were described, and several potential extensions to the model and additional research were proposed. First, the sensitivities of the nucleation rate to changes in temperature, hydrogen concentration, elastic energy, and interfacial energy were quantified within a limited parametric space. Small variations in these quantities can affect the nucleation rate by an order of magnitude or more, and therefore any uncertainty will pose a significant challenge to accurate modeling of hydride precipitation and growth. Next, the spatial variation of the volumetric nucleation rate surrounding a single precipitate was examined. Preliminary evidence indicates that the hydrogen concentration, which is controlled by the stress induced by the precipitate, is the most important factor influencing the nucleation probability. Finally, the effect of the interfacial energy of a nucleating hydride, and thus the nucleation rate, on the microstructure was also examined via 2D simulations. These results indicate that it is essential to employ an accurate value of the interfacial energy between the matrix and nucleating phases in order to quantitatively model microstructural evolution that involves nucleation.

In addition, several paths for future work were discussed. A microstructural evolution model must be able to quantitatively predict the terminal solid solubility for δ-hydride precipitation, but significant uncertainties still exist in the interfacial energy and misfit

strain of a nucleating hydride. Therefore, several experimental and theoretical research directions were proposed to refine the nucleation model presented in this work. Furthermore, the current diffuse interface width required to incorporate physically appropriate interface energies limits the size of the computational domain that can be simulated, and potential methods to allow a wider diffuse interface width were suggested. Finally, the incorporation of thermodiffusion behavior into the model was described, and the incorporation of plasticity and irradiation effects into the model were briefly discussed.

CHAPTER VI

Conclusions

This work describes the development of a quantitative microstructure evolution model of the α-zirconium/δ-hydride system and the associated numerical methods and algorithms. To capture hydrogen diffusion, hydride nucleation and growth, misfit strain, and internal and applied stresses, the phase field approach was chosen. The model capabilities were extended by incorporating linear elastic solid mechanics and classical nucleation theory. The model was parameterized with CALPHAD-based free energies, α/δ misfit strains, elastic stiffnesses, and diffusion coefficients available within the literature; however, the interfacial energy has not been well-characterized.

In addition, a flexible simulation software was created based on the Multiphysics Object Oriented Simulation Environment (MOOSE) finite element framework [68,69]. Two numerical algorithms were designed, implemented, and verified to address challenges presented by the model implementation: a method of incorporating CALPHAD-based free energies that provide realistic energetics, and a method for the explicit introduction of nuclei into the phase field simulation that naturally satisfies mass conservation requirements. The algorithms were described in detail, and verification studies for each were

discussed. In addition, analyses of the sensitivity of the simulation results to the choice of numerical parameters were presented. For example, threshold values for the CALPHAD free energy algorithm and the use of mesh and time adaptivity when employing the nucleation algorithm were studied.

Furthermore, preliminary insights into the nucleation behavior of δ-hydrides were described. First, the sensitivities of the nucleation rate to changes in temperature, hydrogen concentration, elastic energy, and interfacial energy were quantified within a limited parametric space. Next, the spatial variation of the volumetric nucleation rate surrounding a single precipitate was examined. In addition, the effect of the interfacial energy of a nucleating hydride, and thus the nucleation rate, on the microstructure was also examined via 2D simulations. Finally, multiple avenues for future work were discussed, including the terminal solid solubility hysteresis of hydrogen in zirconium and the effects of the α/δ interfacial energy, as well as thermodiffusion, plasticity, and irradiation, which are not yet accounted for in the model.

The development of a quantitative, multiphysics phase field model for the α-zirconium/δ-hydride system advances nuclear materials modeling. Because the model is based on thermodynamics and kinetics, it can be applied to study the microstructural evolution of hydrides in a variety of conditions. For example, hydride nucleation and growth in the presence of a crack tip could be simulated, which occurs during delayed hydride cracking. Data obtained from the mesoscale model, such as the volume fraction of hydrides and the hydride nucleation rate, could be used in engineering-scale models. The model may be easily adapted to other hydrides, such as γ-hydride, by parameterizing it with a suitable chemical free energy description, mobility, and misfit strain tensor. Ultimately, the model and its corresponding simulation software could aid in the development of new zirconium

alloys and play a role in improving the efficiency of nuclear fuel and reducing nuclear waste.

Bibliography

[1] International Atomic Energy Agency, ''IAEA Annual Report 2013,'' 2014. GC(58)/3.

[2] International Atomic Energy Agency, ''Nuclear Power Reactors in the World,'' 2014. IAEA-RDS-2/34.

[3] R. G. Cochran and N. Tsoulfanidis, *The Nuclear Fuel Cycle: Analysis and Management*. La Grange Park, Illinois: American Nuclear Society, second ed., 1990.

[4] 19th International Conference on Nuclear Engineering, *Improving Nuclear Power Plant's Operational Efficiencies in the USA*, 2011.

[5] United States Energy Information Administration, ''Annual Energy Review 2011,'' 2012. DOE/EIA-0384(2011).

[6] Nuclear Energy Institute, ''Safety: The Nuclear Energy Industry's Highest Priority,'' 2015. Series: Fact Sheets.

[7] Consortium for Advanced Simulation of Light Water Reactors, United States Department of Energy, ''Consortium for Advanced Simulation of Light Water Reactors,'' 2015. ORNL 15-G00108/tcc.

[8] ''Power uprates in nuclear power plants: Guidelines and experience,'' Tech. Rep. No. NP-T-3.9, International Atomic Energy Agency, 2011.

[9] D. R. Olander, ''Nuclear fuels - Present and future,'' *Journal of Nuclear Materials*, vol. 389, pp. 1--22, 2009.

[10] United States Nuclear Regulatory Commission, ''Reactor fuel assembly.'' `http://www.nrc.gov/reading-rm/basic-ref/teachers/reactor-fuel-assembly.html`, 2012. [Online; accessed 5 March 2015].

[11] B. Cox, ''Some thoughts on the mechanisms of in-reactor corrosion of zirconium alloys,'' *Journal of Nuclear Materials*, vol. 336, no. 2, pp. 331--368, 2005.

[12] K. Videm, ''Properties of zirconium base cladding materials-corrosion and hydrogen pickup,'' *Nuclear Engineering and Design*, vol. 21, no. 2, pp. 200--211, 1972.

[13] A. M. Garde, G. P. Smith, and R. C. Pirek, ''In-PWR irradiation performance of diliute tin-zirconium advanced alloys,'' in *Zirconium in the Nuclear Industry: Thirteenth International Symposium*, no. ASTM STP 1423, pp. 490--506, ASTM International, 2002.

[14] C. Coleman and D. Hardie, ''The hydrogen embrittlement of α-zirconium: A review,'' *Journal of the Less Common Metals*, vol. 11, no. 3, pp. 168--185, 1966.

[15] B. Cheng, B. Oberlander, W. Wiesenack, S. Yagnik, and J. Turnbull, ''An in-reactor simulation test to evaluate root cause of secondary degradation of defective BWR fuel rod,'' in *Zirconium in the Nuclear Industry: Thirteenth International Symposium*, no. ASTM STP 1423, pp. 616--633, ASTM International, 2002.

[16] A. Sawatzky, ''Formation of hydride blisters in zirconium alloy pressure tubes,'' *Canadian Metallurgical Quarterly*, vol. 24, no. 3, pp. 227--234, 1985.

[17] C. Ells, ''Hydride precipitates in zirconium alloys (a review),'' *Journal of Nuclear Materials*, vol. 28, no. 2, pp. 129--151, 1968.

[18] ''Delayed hydride cracking of zirconium alloy fuel cladding,'' Tech. Rep. IAEA-TECDOC-1649, International Atomic Energy Agency, 2010.

[19] O. Pierron, D. Koss, A. Motta, and K. Chan, ''The influence of hydride blisters on the fracture of Zircaloy-4,'' *Journal of Nuclear Materials*, vol. 322, no. 1, pp. 21--35, 2003.

[20] K. Colas, A. Motta, J. Almer, M. Daymond, M. Kerr, A. Banchik, P. Vizcaino, and J. Santisteban, ''In situ study of hydride precipitation kinetics and re-orientation in Zircaloy using synchrotron radiation,'' *Acta Materialia*, vol. 58, no. 20, pp. 6575--6583, 2010.

[21] ''Waterside corrosion of zirconium alloys in nuclear power plants,'' Tech. Rep. IAEA-TECDOC-996, International Atomic Energy Agency, 1998.

[22] V. Perovic, G. Weatherly, and C. Simpson, ''Hydride precipitation in α/β zirconium alloys,'' *Acta Metallurgica*, vol. 31, no. 9, pp. 1381--1391, 1983.

[23] E. Zuzek, J. P. Abriata, A. San-Martin, and F. D. Manchester, ''The H-Zr (hydrogen-zirconium) system,'' *Bulletin of Alloy Phase Diagrams*, vol. 11, pp. 385--395, 1990.

[24] R. Daum, Y. Chu, and A. Motta, ''Identification and quantification of hydride phases in Zircaloy-4 cladding using synchrotron X-ray diffraction,'' *Journal of Nuclear Materials*, vol. 392, no. 3, pp. 453--463, 2009.

[25] J. Bradbrook, G. Lorimer, and N. Ridley, ''The precipitation of zirconium hydride in zirconium and Zircaloy-2,'' *Journal of Nuclear Materials*, vol. 42, no. 2, pp. 142--160, 1972.

[26] R. N. Singh, P. Ståhle, A. R. Massih, and A. Shmakov, ''Temperature dependence of misfit strains of δ-hydrides of zirconium,'' *Journal of Alloys and Compounds*, vol. 436, no. 1, pp. 150--154, 2007.

[27] G. Carpenter, ''The dilatational misfit of zirconium hydrides precipitated in zirconium,'' *Journal of Nuclear Materials*, vol. 48, no. 3, pp. 264--266, 1973.

[28] A. Barrow, A. Korinek, and M. Daymond, ''Evaluating zirconium--zirconium hydride interfacial strains by nano-beam electron diffraction,'' *Journal of Nuclear Materials*, vol. 432, no. 1, pp. 366--370, 2013.

[29] W. Erickson and D. Hardie, ''The influence of alloying elements on the terminal solid solubility of hydrogen in α-zirconium,'' *Journal of Nuclear Materials*, vol. 13, no. 2, pp. 254--262, 1964.

[30] A. McMinn, E. C. Darby, and J. S. Schofield, ''The terminal solid solubility of hydrogen in zirconium alloys,'' *ASTM Special Technical Publication*, vol. 1354, pp. 173--195, 2000.

[31] K. Une and S. Ishimoto, ''Dissolution and precipitation behavior of hydrides in Zircaloy-2 and high Fe Zircaloy,'' *Journal of Nuclear Materials*, vol. 322, no. 1, pp. 66--72, 2003.

[32] O. Zanellato, M. Preuss, J.-Y. Buffiere, F. Ribeiro, A. Steuwer, J. Desquines, J. Andrieux, and B. Krebs, ''Synchrotron diffraction study of dissolution and precipitation kinetics of hydrides in Zircaloy-4,'' *Journal of Nuclear Materials*, vol. 420, no. 1, pp. 537--547, 2012.

[33] A. Barrow, C. Toffolon-Masclet, J. Almer, and M. Daymond, ''The role of chemical free energy and elastic strain in the nucleation of zirconium hydride,'' *Journal of Nuclear Materials*, vol. 441, no. 1, pp. 395--401, 2013.

[34] J. Santisteban, M. Vicente-Alvarez, P. Vizcaíno, A. Banchik, and J. Almer, ''Hydride precipitation and stresses in Zircaloy-4 observed by synchrotron X-ray diffraction,'' *Acta Materialia*, vol. 58, no. 20, pp. 6609--6618, 2010.

[35] P. Vizcaíno, A. Banchick, and J. Abraita, ''Solubility of hydrogen in Zircaloy-4: irradiation induced increase and thermal recovery,'' *Journal of Nuclear Materials*, vol. 304, pp. 96--106, 2002.

[36] M. Puls, ''The effects of misfit and external stresses on terminal solid solubility in hydride-forming metals,'' *Acta Metallurgica*, vol. 29, no. 12, pp. 1961--1968, 1981.

[37] M. Puls, ''Elastic and plastic accommodation effects on metal-hydride solubility,'' *Acta Metallurgica*, vol. 32, no. 8, pp. 1259--1269, 1984.

[38] M. Puls, ''On the consequences of hydrogen supersaturation effects in Zr alloys to hydrogen ingress and delayed hydride cracking,'' *Journal of Nuclear Materials*, vol. 165, no. 2, pp. 128--141, 1989.

[39] M. Puls, B. Leitch, and S.-Q. Shi, ''The effect of applied stress on the accomodation energy and the solvi for the formation and dissolution of zirconium hydride,'' in *Effect of Hydrogen on the Behavior of Materials* (N. Moody, ed.), pp. 233--248, TMS, 2003.

[40] B. W. Leitch and M. P. Puls, ''Finite element calculations of the accomodation energy of a misfitting precipitate in an elastic-plastic matrix,'' *Metallurgical Transactions A*, vol. 23A, pp. 797--806, 1992.

[41] K. Une and S. Ishimoto, ''Terminal solid solubility of hydrogen in unalloyed zirconium by differential scanning calorimetry,'' *Journal of Nuclear Science and Technology*, vol. 41, no. 9, pp. 949--952, 2004.

[42] R. Tang and X. Yang, ''Dissolution and precipitation behaviors of hydrides in N18, Zry-4 and M5 alloys,'' *International Journal of Hydrogen Energy*, vol. 34, no. 17, pp. 7269--7274, 2009.

[43] G. Slattery, ''The terminal solubility of hydrogen in zirconium alloys between 30 and 400 C,'' *Journal of the Institute of Metals*, vol. 95, no. 2, pp. 43--47, 1967.

[44] J. Kearns, ''Terminal solubility and partitioning of hydrogen in the α phase of zirconium, Zircaloy-2 and Zircaloy-4,'' *Journal of Nuclear Materials*, vol. 22, no. 3, pp. 292--303, 1967.

[45] H. M. Chung, R. S. Daum, J. M. Hiller, and M. C. Billone, ''Characteristics of hydride precipitation and reorientation in spent-fuel cladding,'' in *Zirconium in the Nuclear Industry: Thirteenth International Symposium*, no. ASTM STP 1423, pp. 561--582, ASTM International, 2002.

[46] M. Veleva, S. Arsene, M.-C. Record, J. L. Bechade, and J. Bai, ''Hydride embrittlement and irradiation effects on the hoop mechanical properties of pressurized water reactor (PWR) and boiling-water reactor (BWR) ZIRCALOY cladding tubes: Part II. Morphology of hydrides investigated at different magnifications and their interaction with the processes of plastic deformation,'' *Metallurgical and Materials Transactions A*, vol. 34, no. 3, pp. 567--578, 2003.

[47] V. Perovic, G. Weatherly, S. MacEwen, and M. Leger, ''The influence of prior deformation on hydride precipitation in Zircaloy,'' *Acta Metallurgica et Materialia*, vol. 40, no. 2, pp. 363--372, 1992.

[48] R. Daum, S. Majumdar, Y. Liu, and M. Billone, ''Radial-hydride embrittlement of high-burnup Zircaloy-4 fuel cladding,'' *Journal of Nuclear Science and Technology*, vol. 43, no. 9, pp. 1054--1067, 2006.

[49] M. Louthan and R. Marshall, ''Control of hydride orientation in Zircaloy,'' *Journal of Nuclear Materials*, vol. 9, no. 2, pp. 170--184, 1963.

[50] D. Hardie and M. W. Shanahan, ''Stress reorientation of hydrides in zirconium-2.5 percent niobium,'' *Journal of Nuclear Materials*, vol. 55, pp. 1--13, 1975.

[51] J. Bai, N. Ji, D. Gilbon, C. Prioul, and D. Francois, ''Hydride embrittlement in Zircaloy-4 plate: Part II. Interaction between the tensile stress and the hydride morphology,'' *Metallurgical and Materials Transactions A*, vol. 25, no. 6, pp. 1199--1208, 1994.

[52] K. Sakamoto and M. Nakatsuka, ''Stress reorientation of hydrides in recrystallized Zircaloy-2 sheet,'' *Journal of Nuclear Science and Technology*, vol. 43, no. 9, pp. 1136--1141, 2006.

[53] V. Perovic, G. Weatherly, and C. Simpson, ''The role of elastic strains in the formation of stacks of hydride precipitates in zirconium alloys,'' *Scripta Metallurgica*, vol. 16, pp. 409--412, 1982.

[54] G. E. Fernandez and G. Meyer, ''A reaction-diffusion analysis of the hydriding kinetics of zirconium-based alloys,'' *Journal of Nuclear Materials*, vol. 279, pp. 167--172, 2000.

[55] G. E. Fernandez, G. Meyer, and H. A. Peretti, ''Analysis of the hydride formation kinetics of Zry-4,'' *Journal of Alloys and Compounds*, vol. 330-332, pp. 483--487, 2002.

[56] G. Marino, ''Hydrogen supercharging in Zircaloy,'' *Materials Science and Engineering*, vol. 7, no. 6, pp. 335--341, 1971.

[57] G. Marino, ''A numerical calculation of the redistribution of an interstitial solute in a thermal gradient,'' *Nuclear Science and Engineering*, vol. 49, no. 1, pp. 93--98, 1972.

[58] G. C. Buscaglia and R. A. Enrique, ''Numerical solution of the thermally-assisted diffusion of hydrogen in zirconium alloys considering hysteresis and finite-rate kinetics,'' *International Journal of Numerical Methods for Heat & Fluid Flow*, vol. 6, no. 5, pp. 49--62, 1996.

[59] A. R. Massih and L. O. Jernkvist, ''Stress orientation of second-phase in alloys: Hydrides in zirconium alloys,'' *Computational Materials Science*, vol. 46, no. 4, pp. 1091--1097, 2009.

[60] X. Ma, S. Shi, C. Woo, and L. Chen, ''Effect of applied load on nucleation and growth of γ-hydrides in zirconium,'' *Computational Materials Science*, vol. 23, no. 1, pp. 283--290, 2002.

[61] X. Ma, S. Shi, C. Woo, and L. Chen, ''Phase-field simulation of hydride precipitation in bi-crystalline zirconium,'' *Scripta Materialia*, vol. 47, no. 4, pp. 237--241, 2002.

[62] X. Ma, S. Shi, C. Woo, and L. Chen, ''The phase field model for hydrogen diffusion and γ-hydride precipitation in zirconium under non-uniformly applied stress,'' *Mechanics of Materials*, vol. 38, no. 1, pp. 3--10, 2006.

[63] X. Guo, S. Shi, Q. Zhang, and X. Ma, ''An elastoplastic phase-field model for the evolution of hydride precipitation in zirconium. Part I: Smooth specimen,'' *Journal of Nuclear Materials*, vol. 378, no. 1, pp. 110--119, 2008.

[64] X. Guo, S. Shi, Q. Zhang, and X. Ma, ''An elastoplastic phase-field model for the evolution of hydride precipitation in zirconium. Part II: Specimen with flaws,'' *Journal of Nuclear Materials*, vol. 378, no. 1, pp. 120--125, 2008.

[65] S.-Q. Shi and Z. Xiao, ''A quantitative phase field model for hydride precipitation in zirconium alloys: Part I. development of quantitative free energy functional,'' *Journal of Nuclear Materials*, 2014.

[66] Z. Xiao, M. Hao, X. Guo, G. Tang, and S.-Q. Shi, ''A quantitative phase field model for hydride precipitation in zirconium alloys: Part II. Modeling of temperature dependent hydride precipitation,'' *Journal of Nuclear Materials*, 2014.

[67] R. Dutton, K. Nuttall, M. Puls, and L. Simpson, ''Mechanisms of hydrogen induced delayed cracking in hydride forming materials,'' *Metallurgical Transactions A*, vol. 8, no. 10, pp. 1553--1562, 1977.

[68] M. R. Tonks, D. Gaston, P. C. Millett, D. Andrs, and P. Talbot, ''An object-oriented finite element framework for multiphysics phase field simulations,'' *Computational Materials Science*, vol. 51, no. 1, pp. 20--29, 2012.

[69] D. Gaston, C. Newman, G. Hansen, and D. Lebrun-Grandie, ''MOOSE: A parallel computational framework for coupled systems of nonlinear equations,'' *Nuclear Engineering and Design*, vol. 239, no. 10, pp. 1768--1778, 2009.

[70] A. M. Jokisaari, C. Permann, and K. Thornton, ''A nucleation algorithm for the coupled conserved/nonconserved phase field model,'' *Computational Materials Science*, vol. 112, pp. 128--138, 2016.

[71] A. M. Jokisaari and K. Thornton, ''General method of incorporating calphad free energies of mixing into phase field models: Application to the α-zirconium/δ-hydride system,'' *CALPHAD: Computer Coupling of Phase Diagrams and Thermochemistry*, vol. 51, pp. 334--343, 2015.

[72] L.-Q. Chen, ''Phase-field models for microstructure evolution,'' *Annual Review of Materials Research*, vol. 32, no. 1, pp. 113--140, 2002.

[73] N. Moelans, B. Blanpain, and P. Wollants, ''An introduction to phase-field modeling of microstructure evolution,'' *Calphad*, vol. 32, no. 2, pp. 268--294, 2008.

[74] C. Shen and Y. Wang, *Fundamentals of Modeling for Metals Processing*, vol. 22A of *ASM Handbook*. ASM International, 2009.

[75] I. Steinbach, ''Phase-field models in materials science,'' *Modelling and Simulation in Materials Science and Engineering*, vol. 17, no. 7, p. 073001, 2009.

[76] B. Nestler and A. Choudhury, ''Phase-field modeling of multi-component systems,'' *Current Opinion in Solid State and Materials Science*, vol. 15, no. 3, pp. 93--105, 2011.

[77] H. Emmerich, ''Advances of and by phase-field modelling in condensed-matter physics,'' *Advances in Physics*, vol. 57, no. 1, pp. 1--87, 2008.

[78] Y. Kwon, K. Thornton, and P. W. Voorhees, ''Coarsening of bicontinuous structures via nonconserved and conserved dynamics,'' *Physical Review E*, vol. 75, no. 2, p. 021120, 2007.

[79] Y. Kwon, K. Thornton, and P. Voorhees, ''The topology and morphology of bicontinuous interfaces during coarsening,'' *EPL (Europhysics Letters)*, vol. 86, no. 4, p. 46005, 2009.

[80] D. Seol, S. Hu, Y. Li, J. Shen, K. Oh, and L. Chen, ''Three-dimensional phase-field modeling of spinodal decomposition in constrained films,'' *Metals and Materials International*, vol. 9, no. 1, pp. 61--66, 2003.

[81] J. W. Cahn, ''On spinodal decomposition,'' *Acta Metallurgica*, vol. 9, no. 9, pp. 795--801, 1961.

[82] L.-Q. Chen and A. Khachaturyan, ''Computer simulation of structural transformations during precipitation of an ordered intermetallic phase,'' *Acta Metallurgica et Materialia*, vol. 39, no. 11, pp. 2533--2551, 1991.

[83] S. Hu and L. Chen, ''A phase-field model for evolving microstructures with strong elastic inhomogeneity,'' *Acta Materialia*, vol. 49, no. 11, pp. 1879--1890, 2001.

[84] J. Zhu, T. Wang, A. Ardell, S. Zhou, Z. Liu, and L. Chen, ''Three-dimensional phase-field simulations of coarsening kinetics of γ' particles in binary Ni-Al alloys,'' *Acta Materialia*, vol. 52, no. 9, pp. 2837--2845, 2004.

[85] H.-J. Diepers, C. Beckermann, and I. Steinbach, ''Simulation of convection and ripening in a binary alloy mush using the phase-field method,'' *Acta Materialia*, vol. 47, no. 13, pp. 3663--3678, 1999.

[86] R. Mendoza, I. Savin, K. Thornton, and P. Voorhees, ''Topological complexity and the dynamics of coarsening,'' *Nature Materials*, vol. 3, no. 6, pp. 385--388, 2004.

[87] W. Boettinger, J. Warren, C. Beckermann, and A. Karma, ''Phase-field simulation of solidification 1,'' *Annual Review of Materials Research*, vol. 32, no. 1, pp. 163--194, 2002.

[88] J. A. Warren and W. J. Boettinger, ''Prediction of dendritic growth and microsegregation patterns in a binary alloy using the phase-field method,'' *Acta Metallurgica et Materialia*, vol. 43, no. 2, pp. 689--703, 1995.

[89] J. A. Warren, R. Kobayashi, A. E. Lobkovsky, and W. Craig Carter, ''Extending phase field models of solidification to polycrystalline materials,'' *Acta Materialia*, vol. 51, no. 20, pp. 6035--6058, 2003.

[90] S. Wise, J. Lowengrub, J. Kim, K. Thornton, P. Voorhees, and W. Johnson, ''Quantum dot formation on a strain-patterned epitaxial thin film,'' *Applied Physics Letters*, vol. 87, no. 13, p. 133102, 2005.

[91] Y. U. Wang, Y. M. Jin, and A. G. Khachaturyan, ''Phase field microelasticity modeling of surface instability of heteroepitaxial thin films,'' *Acta Materialia*, vol. 52, no. 1, pp. 81--92, 2004.

[92] L.-Q. Chen, ''Phase-field method of phase transitions/domain structures in ferroelectric thin films: A review,'' *Journal of the American Ceramic Society*, vol. 91, no. 6, pp. 1835--1844, 2008.

[93] D. Seol, S. Hu, Z. Liu, L. Chen, S. Kim, and K. Oh, ''Phase-field modeling of stress-induced surface instabilities in heteroepitaxial thin films,'' *Journal of Applied Physics*, vol. 98, no. 4, p. 044910, 2005.

[94] S. M. Allen and J. W. Cahn, ''A microscopic theory for antiphase boundary motion and its application to antiphase domain coarsening,'' *Acta Metallurgica*, vol. 27, no. 6, pp. 1085--1095, 1979.

[95] J. W. Cahn and J. E. Hilliard, ''Free energy of a nonuniform system. I. Interfacial free energy,'' *The Journal of Chemical Physics*, vol. 28, no. 2, pp. 258--267, 1958.

[96] R. W. Balluffi, S. Allen, and W. C. Carter, *Kinetics of Materials*. John Wiley & Sons, 2005.

[97] A. A. Wheeer, W. J. Boettinger, and G. B. McFadden, ''Phase-field model for isothermal phase transitions in binary alloys,'' *Physical Review A*, vol. 45, no. 10, pp. 7424--7439, 1992.

[98] N. Dupin, I. Ansara, C. Servant, C. Toffolon, C. Lemaignan, and J. Brachet, ''A thermodynamic database for zirconium alloys,'' *Journal of Nuclear Materials*, vol. 275, no. 3, pp. 287--295, 1999.

[99] H. L. Lukas, S. G. Fries, and B. Sundman, *Computational Thermodynamics: the Calphad Method*, vol. 131. Cambridge University Press Cambridge, 2007.

[100] N. Saunders and A. P. Miodownik, *CALPHAD (Calculation of Phase Diagrams): A Comprehensive Guide*, vol. 1. Elsevier, 1998.

[101] P.-R. Cha, D.-H. Yeon, and J.-K. Yoon, ''A phase field model for isothermal solidification of multicomponent alloys,'' *Acta Materialia*, vol. 49, no. 16, pp. 3295--3307, 2001.

[102] D.-H. Yeon, P.-R. Cha, and J.-K. Yoon, ''A phase field study for ferrite-austenite transitions under para-equilibrium,'' *Scripta Materialia*, vol. 45, no. 6, pp. 661--668, 2001.

[103] I. Loginova, J. Agren, and G. Amberg, ''On the formation of widmanstatten ferrite in binary Fe-C - Phase-field approach,'' *Acta Materialia*, vol. 52, no. 13, pp. 4055--4063, 2004.

[104] J. Rudnizki, B. Bottger, U. Prahl, and W. Bleck, ''Phase-field modeling of austenite formation from a ferrite plus pearlite microstructure during annealing of cold-rolled dual-phase steel,'' *Metallurgical and Materials Transactions A*, vol. 42, no. 8, pp. 2516--2525, 2011.

[105] U. Grafe, B. Bottger, J. Tiaden, and S. Fries, ''Coupling of multicomponent thermodynamic databases to a phase field model: application to solidification and solid state transformations of superalloys,'' *Scripta Materialia*, vol. 42, no. 12, pp. 1179--1186, 2000.

[106] J. Zhu, Z. Liu, V. Vaithyanathan, and L. Chen, ''Linking phase-field model to CALPHAD: Application to precipitate shape evolution in Ni-base alloys,'' *Scripta Materialia*, vol. 46, no. 5, pp. 401--406, 2002.

[107] K. Wu, Y. Chang, and Y. Wang, ''Simulating interdiffusion microstructures in Ni-Al-Cr diffusion couples: A phase field approach coupled with CALPHAD database,'' *Scripta Materialia*, vol. 50, no. 8, pp. 1145--1150, 2004.

[108] J. Wang, M. Osawa, T. Yokokawa, H. Harada, and M. Enomoto, ''Modeling the microstructural evolution of ni-base superalloys by phase field method combined with calphad and cvm,'' *Computational Materials Science*, vol. 39, no. 4, pp. 871--879, 2007.

[109] T. Kitashima, J. Wang, and H. Harada, ''Phase-field simulation with the CALPHAD method for the microstructure evolution of multi-component ni-base superalloys,'' *Intermetallics*, vol. 16, no. 2, pp. 239--245, 2008.

[110] N. Warnken, D. Ma, A. Drevermann, R. C. Reed, S. Fries, and I. Steinbach, ''Phase-field modelling of as-cast microstructure evolution in nickel-based superalloys,'' *Acta Materialia*, vol. 57, no. 19, pp. 5862--5875, 2009.

[111] Y. Wen, J. Lill, S. Chen, and J. Simmons, ''A ternary phase-field model incorporating commercial CALPHAD software and its application to precipitation in superalloys,'' *Acta Materialia*, vol. 58, no. 3, pp. 875--885, 2010.

[112] B. Bottger, J. Eiken, and I. Steinbach, ''Phase field simulation of equiaxed solidification in technical alloys,'' *Acta Materialia*, vol. 54, no. 10, pp. 2697--2704, 2006.

[113] S. Hu, J. Murray, H. Weiland, Z. Liu, and L. Chen, ''Thermodynamic description and growth kinetics of stoichiometric precipitates in the phase-field approach,'' *Calphad*, vol. 31, no. 2, pp. 303--312, 2007.

[114] H. Kobayashi, M. Ode, S. Gyoon Kim, W. Tae Kim, and T. Suzuki, ''Phase-field model for solidification of ternary alloys coupled with thermodynamic database,'' *Scripta Materialia*, vol. 48, no. 6, pp. 689--694, 2003.

[115] R. Qin and E. Wallach, ''A phase-field model coupled with a thermodynamic database,'' *Acta Materialia*, vol. 51, no. 20, pp. 6199--6210, 2003.

[116] R. Qin, E. Wallach, and R. Thomson, ''A phase-field model for the solidification of multicomponent and multiphase alloys,'' *Journal of Crystal Growth*, vol. 279, no. 1, pp. 163--169, 2005.

[117] I. Steinbach, B. Bottger, J. Eiken, N. Warnken, and S. Fries, ''Calphad and phase-field modeling: A successful liaison,'' *Journal of Phase Equilibria and Diffusion*, vol. 28, no. 1, pp. 101--106, 2007.

[118] Y. Mishin, W. Boettinger, J. Warren, and G. McFadden, ''Thermodynamics of grain boundary premelting in alloys. I. Phase-field modeling,'' *Acta Materialia*, vol. 57, no. 13, pp. 3771--3785, 2009.

[119] J. Heulens, B. Blanpain, and N. Moelans, ''Phase field modeling of the crystallization of FeOx-SiO2 melts in contact with an oxygen-containing atmosphere,'' *Chemical Geology*, vol. 290, no. 3, pp. 156--162, 2011.

[120] J.-L. Fattebert, M. Wickett, and P. Turchi, ''Phase-field modeling of coring during solidification of Au-Ni alloy using quaternions and CALPHAD input,'' *Acta Materialia*, vol. 62, pp. 89--104, 2014.

[121] Q. Chen, N. Ma, K. Wu, and Y. Wang, ''Quantitative phase field modeling of diffusion-controlled precipitate growth and dissolution in Ti-Al-V,'' *Scripta Materialia*, vol. 50, no. 4, pp. 471--476, 2004.

[122] H. Singer, I. Singer, and A. Jacot, ''Phase-field simulations of α to γ precipitations and transition to massive transformation in the Ti-Al alloy,'' *Acta Materialia*, vol. 57, no. 1, pp. 116--124, 2009.

[123] M. Park, S. Gibbons, and R. Arroyave, ''Phase-field simulations of intermetallic compound evolution in Cu/Sn solder joints under electromigration,'' *Acta Materialia*, vol. 61, no. 19, pp. 7142--7154, 2013.

[124] M. Hillert and L.-I. Staffansson, ''The regular solution model for stoichiometric phases and ionic melts,'' *Acta Chemica Scandinavica*, vol. 24, pp. 3618--3626, 1970.

[125] B. Sundman and J. Agren, ''A regular solution model for phases with several components and sublattices, suitable for computer applications,'' *Journal of Physics and Chemistry of Solids*, vol. 42, pp. 297--301, 1981.

[126] A. T. Dinsdale, ''SGTE data for pure elements,'' *CALPHAD*, vol. 15, pp. 317--425, 1991.

[127] J. D. Cox, D. D. Wagman, and V. A. Medvedev, *CODATA: Key Values for Thermodynamics*. New York: Hemisphere Publishing Corporation, 1989.

[128] C. M. Elliott, D. A. French, and F. A. Milner, ''A second order splitting method for the Cahn-Hilliard equation,'' *Numerische Mathematik*, vol. 54, pp. 575--590, 1989.

[129] L. Zhang, M. R. Tonks, D. Gaston, J. W. Peterson, D. Andrs, P. C. Millett, and B. S. Biner, ''A quantitative comparison between C0 and C1 elements for solving the Cahn-Hilliard equation,'' *Journal of Computational Physics*, vol. 236, pp. 74--80, 2013.

[130] L. Zhang, M. R. Tonks, D. Gaston, J. W. Peterson, D. Andrs, P. C. Millett, and B. S. Biner, ''A quantitative comparison between C0 and C1 elements for solving the Cahn--Hilliard equation,'' *Journal of Computational Physics*, vol. 236, pp. 74--80, 2013.

[131] J. J. Kearns, ''Diffusion coefficient of hydrogen in α zirconium, Zircaloy-2 and Zircaloy-4,'' *Journal of Nuclear Materials*, vol. 43, pp. 330--338, 1972.

[132] G. Majer, W. Renz, and R. Barnes, ''The mechanism of hydrogen diffusion in zirconium dihydrides,'' *Journal of Physics: Condensed Matter*, vol. 6, no. 15, p. 2935, 1994.

[133] J. D. Eshelby, ''The determination of the elastic field of an ellipsoidal inclusion, and related problems,'' *Proceedings of the Royal Society of London. Series A, Mathematical and Physical Sciences*, vol. 241, no. 1226, pp. 376--396, 1957.

[134] E. S. Fisher and C. J. Renken, ''Single-crystal elastic moduli and the hcp to bcc transformation in ti, zr, and hf,'' *Physical Review*, vol. 135, pp. A482--A494, 1964.

[135] K. Bathe, *Finite Element Procedures*. Prentice Hall, 2006.

[136] F. Auricchio, F. Brezzi, and C. Lovadina, ''Mixed finite element methods,'' in *Fundamentals* (E. Stein, R. de Borst, and T. Hughes, eds.), vol. 1 of *Encyclopedia of Computational Mechanics*, pp. 1--43, John Wiley and Sons, 2004.

[137] K. Srinivasan, K. Matouš, and P. Geubelle, ''Generalized finite element method for modeling nearly incompressible bimaterial hyperelastic solids,'' *Computer Methods in Applied Mechanics and Engineering*, vol. 197, no. 51, pp. 4882--4893, 2008.

[138] P. A. T. Olsson, A. R. Massih, J. Blomqvist, A.-M. Alvarez Holston, and C. Bjerken, ''Ab initio thermodynamics of zirconium hydrides and deuterides,'' *Computational Materials Science*, vol. 86, pp. 211--222, 2014.

[139] M. Kerr, M. Daymond, R. Holt, and J. Almer, ''Strain evolution of zirconium hydride embedded in a zircaloy-2 matrix,'' *Journal of Nuclear Materials*, vol. 380, no. 1-3, pp. 70--75, 2008. cited By 0.

[140] M. Puls, S.-Q. Shi, and J. Rabier, ''Experimental studies of mechanical properties of solid zirconium hydrides,'' *Journal of Nuclear Materials*, vol. 336, no. 1, pp. 73 -- 80, 2005.

[141] A. Rico, M. Martin-Rengel, J. Ruiz-Hervias, J. Rodriguez, and F. Gomez-Sanchez, ''Nanoindentation measurements of the mechanical properties of zirconium matrix and hydrides in unirradiated pre-hydrided nuclear fuel cladding,'' *Journal of Nuclear Materials*, vol. 452, no. 1-3, pp. 69--76, 2014.

[142] H. E. Rosinger and D. O. Northwood, ''The elastic properties of zirconium alloy fuel cladding and pressure tubing materials,'' *Journal of Nuclear Materials*, vol. 79, pp. 170--179, 1979.

[143] S. Yamanaka, K. Yoshioka, M. Uno, M. Katsura, H. Anada, T. Matsuda, and S. Kobayashi, ''Thermal and mechanical properties of zirconium hydride,'' *Journal of Alloys and Compounds*, vol. 293-295, pp. 23--29, 1999.

[144] H. Peisl, ''Lattice strains due to hydrogen in metals,'' in *Hydrogen in Metals I* (G. Alefeld and J. Voelkl, eds.), vol. 28 of *Topics in Applied Physics*, pp. 53--74, Springer Berlin Heidelberg, 1978.

[145] S. R. MacEwen, C. E. Coleman, and C. E. Ells, ''Dilation of hcp zirconium by interstitial deuterium,'' *Acta Metallurgica*, vol. 33, pp. 753--757, 1985.

[146] A. G. Khachaturyan, *Theory of Structural Transformations in Solids*. Courier Corporation, 2008.

[147] G. Boussinot, Y. Le Bouar, and A. Finel, ''Phase-field simulations with inhomogeneous elasticity: Comparison with an atomic-scale method and application to superalloys,'' *Acta Materialia*, vol. 58, no. 12, pp. 4170--4181, 2010.

[148] D. Schneider, S. Schmid, M. Selzer, T. Böhlke, and B. Nestler, ''Small strain elastoplastic multiphase-field model,'' *Computational Mechanics*, vol. 55, no. 1, pp. 27--35, 2015.

[149] D. Turnbull and B. Vonnegut, ''Nucleation catalysis.,'' *Industrial & Engineering Chemistry*, vol. 44, no. 6, pp. 1292--1298, 1952.

[150] L. Thuinet and R. Besson, ''Ab initio study of competitive hydride formation in zirconium alloys,'' *Intermetallics*, vol. 20, pp. 24--32, 2012.

[151] A. Cottrell, *Dislocations and Plastic Flow in Crystals*. International Series of Monographs on Physics, Clarendon Press, 1965.

[152] D. A. Porter and K. E. Easterling, *Phase Transformations in Metals and Alloys, (Revised Reprint)*. CRC Press, 1992.

[153] A. Jain, S. P. Ong, G. Hautier, W. Chen, W. D. Richards, S. Dacek, S. Cholia, D. Gunter, D. Skinner, G. Ceder, *et al.*, ''Commentary: The materials project: A materials genome approach to accelerating materials innovation,'' *APL Materials*, vol. 1, no. 1, p. 011002, 2013.

[154] P. Patel, ''Materials genome initiative and energy,'' *MRS Bulletin*, vol. 36, pp. 964--966, 12 2011.

[155] J. Simmons, C. Shen, and Y. Wang, ''Phase field modeling of simultaneous nucleation and growth by explicitly incorporating nucleation events,'' *Scripta Materialia*, vol. 43, no. 10, pp. 935--942, 2000.

[156] Y. Wang, H. Wang, L. Chen, and A. Khachaturyan, ''Microstructural development of coherent tetragonal precipitates in magnesium-partially-stabilized zirconia - A computer simulation,'' *Journal of the American Ceramic Society*, vol. 78, no. 3, pp. 657--661, 1995.

[157] Y. Wang, D. Banerjee, C. Su, and A. Khachaturyan, ''Field kinetic model and computer simulation of precipitation of Ll(2) ordered intermetallics from FCC solid solution,'' *Acta Materialia*, vol. 46, no. 9, pp. 2983--3001, 1998.

[158] A. Artemev, Y. Jin, and A. Khachaturyan, ''Three-dimensional phase field model of proper martensitic transformation,'' *Acta Materialia*, vol. 49, no. 7, pp. 1165--1177, 2001.

[159] M. Castro, ''Phase-field approach to heterogeneous nucleation,'' *Phys. Rev. B*, vol. 67, p. 035412, 2003.

[160] J. Simmons, Y. Wen, C. Shen, and Y. Wang, ''Microstructural development involving nucleation and growth phenomena simulated with the Phase Field method,'' *Materials Science and Engineering A-Structural Materials Properties Microstructure and Processing*, vol. 365, no. 1-2, pp. 136--143, 2004.

[161] M. Park and R. Arroyave, ''Concurrent nucleation, formation and growth of two intermetallic compounds (Cu6Sn5 and Cu3Sn) during the early stages of lead-free soldering,'' *Acta Materialia*, vol. 60, no. 3, pp. 923--934, 2012.

[162] S. Hu and L. Chen, ''Solute segregation and coherent nucleation and growth near a dislocation - A phase-field model integrating defect and phase microstructures,'' *Acta Materialia*, vol. 49, no. 3, pp. 463--472, 2001.

[163] W. Zhang, Y. Jin, and A. Khachaturyan, ''Phase field microelasticity modeling of heterogeneous nucleation and growth in martensitic alloys,'' *Acta Materialia*, vol. 55, no. 2, pp. 565--574, 2007.

[164] L. Granasy, T. Borzsonyi, and T. Pusztai, ''Nucleation and bulk crystallization in binary phase field theory,'' *Physical Review Letters*, vol. 88, no. 20, 2002.

[165] C. Shen, J. Li, and Y. Wang, ''Finding critical nucleus in solid-state transformations,'' *Metallurgical and Materials Transactions A-Physical Metallurgy and Materials Science*, vol. 39A, no. 5, pp. 976--983, 2008.

[166] L. Zhang, L.-Q. Chen, and Q. Du, ''Morphology of critical nuclei in solid-state phase transformations,'' *Physical Review Letters*, vol. 98, no. 26, 2007.

[167] L. Zhang, L.-Q. Chen, and Q. Du, ''Diffuse-interface description of strain-dominated morphology of critical nuclei in phase transformations,'' *Acta Materialia*, vol. 56, no. 14, pp. 3568--3576, 2008.

[168] L. Zhang, L.-Q. Chen, and Q. Du, ''Mathematical and numerical aspects of a phase-field approach to critical nuclei morphology in solids,'' *Journal of Scientific Computing*, vol. 37, no. 1, pp. 89--102, 2008.

[169] E. Clouet, *Fundamentals of Modeling for Metals Processing*, vol. 22A of *ASM Handbook*. ASM International, 2009.

[170] C. Shen, J. Simmons, and Y. Wang, ''Effect of elastic interaction on nucleation: I. Calculation of the strain energy of nucleus formation in an elastically anisotropic crystal of arbitrary microstructure,'' *Acta Materialia*, vol. 54, no. 20, pp. 5617--5630, 2006.

[171] M. Doi, ''Elasticity effects on the microstructure of alloys containing coherent precipitates,'' *Progress in Materials Science*, vol. 40, pp. 79--180, 1996.

[172] J. Robson, ''Modelling the overlap of nucleation, growth and coarsening during precipitation,'' *Acta Materialia*, vol. 52, no. 15, pp. 4669--4676, 2004.

[173] V. Vaithyanathan, C. Wolverton, and L. Q. Chen, ''Multiscale modeling of theta prime precipitation in Al-Cu binary alloys,'' *Acta Materialia*, vol. 52, pp. 2973--2987, 2004.

[174] J. D. Hoffman and S. Frankel, *Numerical Methods for Engineers and Scientists, Second Edition*. New York: Marcel Dekker, Inc., 2001.

[175] R. Eymard, T. Gallouët, and R. Herbin, ''Finite volume methods,'' *Handbook of Mumerical Analysis*, vol. 7, pp. 713--1018, 2000.

[176] E. C. Becker, G. F. Carey, and J. T. Oden, *Finite Elements: An Introduction*. Englewood Cliffs, New Jersey: Prentice-Hall, 1981.

[177] P. Solin, K. Segeth, and I. Dolezel, *Higher-Order Finite Element Methods*. Studies in Advanced Mathematics, CRC Press, 2003.

[178] D. A. Knoll and D. E. Keyes, ''Jacobian-free newton--krylov methods: a survey of approaches and applications,'' *Journal of Computational Physics*, vol. 193, no. 2, pp. 357--397, 2004.

[179] S. Balay, S. Abhyankar, M. Adams, J. Brown, P. Brune, K. Buschelman, L. Dalcin, V. Eijkhout, W. Gropp, D. Karpeyev, D. Kaushik, M. Knepley, L. Curfman McInnes, K. Rupp, B. Smith, S. Zampini, and Z. H., *PETSc Users Manual, Revision 3.6*. Argonne National Laboratory, 2015.

[180] Argonne National Laboratory, ''2010-2015 Strategic Plan: The U.S. Department of Energy's Argonne National Laboratory,'' 2010.

[181] D. R. Gaston, J. W. Peterson, C. J. Permann, D. Andrs, A. E. Slaughter, and J. M. Miller, ''Continuous integration for concurrent computational framework and application development,'' *Journal of Open Research Software*, vol. 2, no. 1, p. e10, 2014.

[182] D. R. Gaston, C. J. Permann, J. W. Peterson, A. E. Slaughter, a. Andrš, Y. Wang, M. P. Short, D. M. Perez, M. R. Tonks, J. Ortensi, *et al.*, ''Physics-based multiscale coupling for full core nuclear reactor simulation,'' *Annals of Nuclear Energy*, 2014.

[183] B. S. Kirk, J. W. Peterson, R. H. Stogner, and G. F. Carey, ''libmesh: a c++ library for parallel adaptive mesh refinement/coarsening simulations,'' *Engineering with Computers*, vol. 22, no. 3-4, pp. 237--254, 2006.

[184] J. Mangeri, O. Heinonen, D. Karpeyev, and S. Nakhmanson, ''Influence of elastic and surface strains on the optical properties of semiconducting core-shell nanoparticles,'' *Physics Review Applied*, vol. 4, p. 014001, 2015.

[185] P. Chakraborty, Y. Zhang, and M. R. Tonks, ''Multi-scale modeling of microstructure dependent intergranular brittle fracture using a quantitative phase-field based method,'' *submitted to Computational Materials Science*, 2015.

[186] D. P. Adhikary, C. T. Jayasundara, R. K. Podgorney, and A. H. Wilkins, ''Multisurface plasticity in practice,'' *submitted to International Journal for Numerical Methods in Engineering*, 2015.

[187] K. Grönhagen, J. Ågren, and M. Odén, ''Phase-field modelling of spinodal decomposition in tialn including the effect of metal vacancies,'' *Scripta Materialia*, vol. 95, pp. 42 -- 45, 2015.

[188] S. G. Kim, W. T. Kim, and T. Suzuki, ''Phase-field model for binary alloys,'' *Physical Review E*, vol. 60, no. 6, pp. 7186--7197, 1999.

[189] M. J. Welland, D. Wolf, and J. E. Guyer, ''Multicomponent phase-field model for extremely large partition coefficients,'' *Physical Review E*, vol. 89, p. 012409, Jan 2014.

[190] H. Xiong, Z. Huang, Z. Wu, and P. P. Conway, ''A generalized computational interface for combined thermodynamic and kinetic modeling,'' *Calphad*, vol. 35, no. 3, pp. 391--395, 2011.

[191] L. Zhang, M. Stratmann, Y. Du, B. Sundman, and I. Steinbach, ''Incorporating the CALPHAD sublattice approach of ordering into the phase-field model with finite interface dissipation,'' *Acta Materialia*, vol. 88, pp. 156--169, 2015.

[192] A. Yamanaka, T. Takaki, and Y. Tomita, ''Simulation of austenite-to-ferrite transformation in deformed austenite by crystal plasticity finite element method and multi-phase-field method,'' *ISIJ international*, vol. 52, no. 4, pp. 659--668, 2012.

[193] K. Ankit, A. Choudhury, C. Qin, S. Schulz, M. McDaniel, and B. Nestler, ''Theoretical and numerical study of lamellar eutectoid growth influenced by volume diffusion,'' *Acta Materialia*, vol. 61, no. 11, pp. 4245--4253, 2013.

[194] T. Philippe, D. Erdeniz, D. Dunand, and P. Voorhees, ''A phase-field study of the aluminizing of nickel,'' *Philosophical Magazine*, no. ahead-of-print, pp. 1--13, 2015.

[195] H. Liu, Y. Gao, J. Liu, Y. Zhu, Y. Wang, and J. Nie, ''A simulation study of the shape of β precipitates in Mg-Y and Mg-Gd alloys,'' *Acta Materialia*, vol. 61, no. 2, pp. 453--466, 2013.

[196] A. Iserles, *A First Course in the Numerical Analysis of Differential Equations*. Cambridge, UK: Cambridge University Press, first ed., 1996.

[197] A. Malik, G. Amberg, A. Borgenstam, and J. Ågren, ''Effect of external loading on the martensitic transformation--a phase field study,'' *Acta Materialia*, vol. 61, no. 20, pp. 7868--7880, 2013.

[198] M. R. Tonks, D. Gaston, P. C. Millett, D. Andrs, and P. Talbot, ''An object-oriented finite element framework for multiphysics phase field simulations,'' *Computational Materials Science*, vol. 51, no. 1, pp. 20--29, 2012.

[199] J. Christian, *The Theory of Transformations in Metals and Alloys, Part I*. New York: Pergamon Press, second ed., 1975.

[200] M. Avrami, ''Kinetics of phase change I - General theory,'' *Journal of Chemical Physics*, vol. 7, no. 12, pp. 1103--1112, 1939.

[201] M. Avrami, ''Kinetics of phase change II - Transformation-time relations for random distribution of nuclei,'' *Journal of Chemical Physics*, vol. 8, no. 2, pp. 212--224, 1940.

[202] F. S. Ham, ''Theory of diffusion-limited precipitation,'' *Journal of Physics and Chemistry of Solids*, vol. 6, no. 4, pp. 335--351, 1958.

[203] M. Blackmur, J. Robson, M. Preuss, O. Zanellato, R. Cernik, S.-Q. Shi, F. Ribeiro, and J. Andrieux, ''Zirconium hydride precipitation kinetics in zircaloy-4 observed with synchrotron x-ray diffraction,'' *Journal of Nuclear Materials*, vol. 464, pp. 160--169, 2015.

[204] C. Shen, J. Simmons, and Y. Wang, ''Effect of elastic interaction on nucleation: II. Implementation of strain energy of nucleus formation in the phase field method,'' *Acta Materialia*, vol. 55, no. 4, pp. 1457--1466, 2007.

[205] Z.-K. Liu and J. gren, ''On two-phase coherent equilibrium in binary alloys,'' *Acta Metallurgica et Materialia*, vol. 38, pp. 561--572, 1990.

[206] J. W. Cahn, ''Nucleation on dislocations,'' *Acta Metallurgica*, vol. 5, no. 3, pp. 169--172, 1957.

[207] F. C. Larche, ''Nucleation and precipitation on dislocations,'' in *Dislocations in Solids* (F. R. N. Nabarro, ed.), vol. 4, pp. 135--153, North-Holland Publishing Company, 1979.

[208] C. Shen, Q. Chen, Y. Wen, J. Simmons, and Y. Wang, ''Increasing length scale of quantitative phase field modeling of growth-dominant or coarsening-dominant process,'' *Scripta Materialia*, vol. 50, no. 7, pp. 1023--1028, 2004.

[209] A. Sawatzky, ''Hydrogen in Zircaloy-2: Its distribution and heat of transport,'' *Journal of Nuclear Materials*, vol. 2, no. 4, pp. 321--328, 1960.

[210] K. Hashizume, M. Hayakawa, M. Koganemaru, and M. Sugisaki, ''Temperature dependence of heat of transport of hydrogen in zirconium,'' in *Defect and Diffusion Forum*, vol. 95, pp. 323--328, Trans Tech Publ, 1993.

[211] H. M. Zbib, M. Rhee, and J. P. Hirth, ''On plastic deformation and the dynamics of 3d dislocations,'' *International Journal of Mechanical Sciences*, vol. 40, no. 2, pp. 113--127, 1998.

[212] D. Raabe, ''Introduction of a hybrid model for the discrete 3d simulation of dislocation dynamics,'' *Computational Materials Science*, vol. 11, no. 1, pp. 1--15, 1998.

[213] G. J. C. Carpenter and J. F. Watters, ''Irradiation damage recovery in some zirconium alloys,'' in *Zirconium in Nuclear Applications*, no. ASTM STP 551, pp. 400--415, American Society for Testing and Materials, 1974.